Ultrabright Source of Polarization-Entangled Photons from Cavity-Enhanced Downconversion

by

Christopher Edward Kuklewicz

Submitted to the Department of Physics
in partial fulfillment of the requirements for the degree of

Doctor of Philosophy

at the

MASSACHUSETTS INSTITUTE OF TECHNOLOGY

October 2005

Author . . . .
Department of Physics
October 21, 2005

Certified by . . . .
Erich P. Ippen
Professor
Thesis Supervisor

Certified by . . . .
Franco N.C. Wong
Senior Research Scientist
Thesis Supervisor

Accepted by . . . .
Thomas J. Greytak
Chairman, Department Committee on Graduate Students

Ultrabright Source of Polarization-Entangled Photons from Cavity-Enhanced Downconversion

by

Christopher Edward Kuklewicz

Submitted to the Department of Physics
on October 21, 2005, in partial fulfillment of the
requirements for the degree of
Doctor of Philosophy

Abstract

This thesis describes the design, construction, and testing of a new source of entanglement. The goal is to produce pairs of photons which are not only polarization-entangled, but also have a high brightness within a narrow bandwidth. This novel source is more suitable than previous SPDC sources for transferring entanglement to future qubit storage such as a trapped rubidium memory. The narrow bandwidth is imposed by modifying the spectrum of the photon pairs by performing the downconversion inside a cavity. The collinear downconversion geometry inside the linear cavity is achieved by using a quasi-phased-matched periodically-poled potassium titanyl phosphate (PPKTP) crystal. The single-pass free-space photon-pairs produced were demonstrated to be polarization-entangled by measuring the Hong-Ou-Mandel interference dip and measuring a violation of Bell's inequality of 2.711 ± 0.010 (which was greater than the classical limit of 2). The cavity-enhanced downconversion was observed with a brightness of 0.7 pairs/s per mW of pump per MHz of bandwidth in the Gaussian mode collected (a generation rate of 110 pairs/s/mW/MHz is inferred). The interference dip from the pairs was measured to have a visibility of 75% when near the ideal equal-FSR operating point, where the pairs are in the biphoton triplet state. When detuned to have unequal FSR the output pairs show the an interference dip behavior consisting of a combination of triplet and singlet states that depends on the time separation of the pair as it leaves the cavity. The observed results corroborate detailed predictions of a Gaussian-state model of cavity-enhanced downconversion.

Thesis Supervisor: Erich P. Ippen
Title: Professor

Thesis Supervisor: Franco N.C. Wong
Title: Senior Research Scientist

Acknowledgments

I would like to thank my adviser Franco Wong for giving me the opportunity to work on this project. And I wish to thank my coworkers, especially Elliot Mason who helped teach me what I needed to understand about nonlinear optics and Eser Keskiner for working with me on my first experiments. For the single-pass PPKTP experiments, I thank Gaétan Messin for working with me to achieve our excellent results. And I wish to thank Jeff Shapiro for bringing me from ignorance to excellence with respect to the theory. I am grateful for the friendship and support of Shane Haas, Marco Fiorentino, Marius Albota, Pavel Gorelik, Taehyun Kim, and Onur Kuzucu. Thank you all for wonderful, and wide ranging, discussions that have helped make working in this group, and eating lunch, something to look forward to each day.

I owe particular thanks to Theresa Robinson for proof-reading this thesis, and helping me focus when procrastination was winning. I am also in debt to my parents, Gerald and Pauline, who have always encouraged and supported me, and my brother Andrew who has done the most to inspire me to achieve success and happiness.

And finally I want to thank the other member of my committee, Erich Ippen, Daniel Kleppner, and Michael Feld for helping me achieve my ambition here at M.I.T.

Contents

List of Figures

List of Tables

Chapter 1

Introduction

> George got stung by a bee and said,
> “I wouldn’t have got stung if I’d stayed in bed.”
> Fred got stung and we heard him roar,
> “What am I being punished for?”
> Lew got stung and we heard him say,
> “I learned somethin’ about bees today.”
> **Shel Silverstein**, *Three Stings*

The goal of quantum optics is to study the electromagnetic field where Maxwell’s equations and “semi-classical” models no longer apply. Experiments to observe quantum features [1] evolve into complex state preparation, and make it possible to perform fundamental tests of quantum theory, such as Bell’s inequality [2]. These states have been or may eventually be used in larger experiments to perform precision measurements, quantum computation [3], or encrypted communication [4]. In particular, communication via quantum teleportation [5] has been proposed. Almost all these systems use a source of entangled photons that have strong correlations beyond what classical physics allows. The purpose of this work is to develop a novel entanglement source to enable efficient communication via quantum teleportation. In particular I will develop a source, and the corresponding theory, which produces polarization-entangled pairs where both photons are nearly the same frequency, i.e. degenerate. The rate of pair generation within a few MHz of exact degeneracy will be over an order of magnitude brighter that any previous system.

1.1 Teleportation Architecture

There are three ways to communicate a quantum state from one party to another. If the sender knows what the quantum state is or how to prepare it, then the "recipe" can be sent via normal, classical communications. If the state has been prepared, then the physical subsystem underlying the state can be "transported" to the receiver; usually this will be photons through free space or a fiber. There is a third way to send a state, which is via a quantum "teleportation" protocol which is summarized below. Like the "transport" mechanism, "teleportation" can transmit a message state which is unknown to any of the participants.

To be concrete, define the message state to be the superposition of two particular known orthogonal states in a Hilbert space. The quantum state of such a two element system is called a qubit. As a precondition, all qubit teleportation protocols depend on each of the two parties having half of a fully entangled pair of qubit states, such as a singlet or triplet state. This source is shown in Fig. 1-1 at location S and the pair is stored in two quantum memories at each location, marked M in the figure. The sender Alice then needs to make a complete joint measurement of the message qubit and the entangled qubit in the four state Bell basis (location B). The result of the measurement puts those two qubits into a known Bell state with uniform probability across the 4 states, generating two classical bits. This random pair of bits is sent classically to the receiver Bob, who then performs one of 4 local unitary operations (at location U) corresponding to the measured Bell state communicated by Alice, on the shared entangled qubit. After the unitary operation, Bob's qubit is then in the same state as the message qubit was initially. At no point does Alice or Bob know or

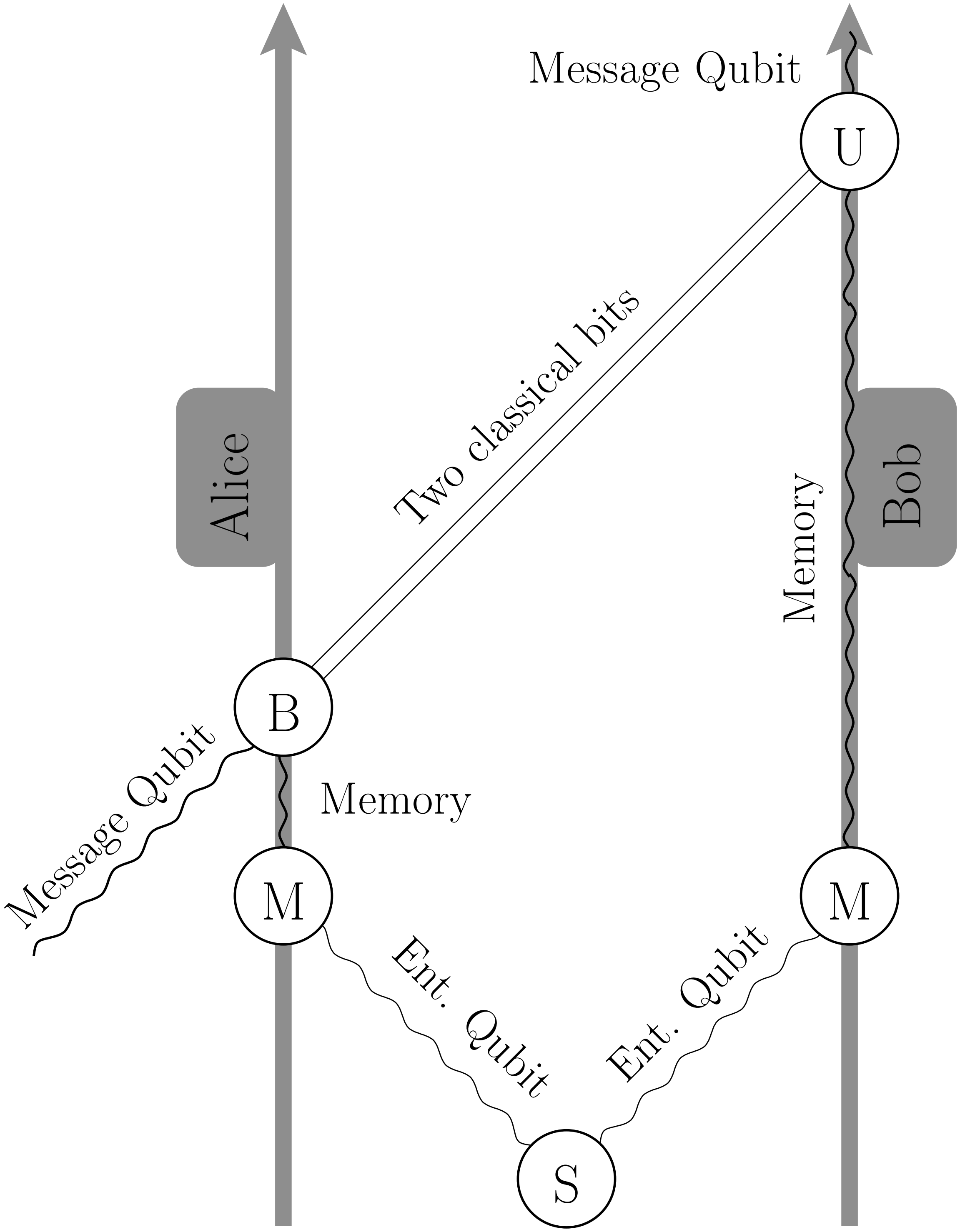

Figure 1-1: Illustration of quantum teleportation. Time increases upward, space is horizontal.

learn anything about the quantum state of the message.

The specific architecture proposed in Ref. [6] calls for the quantum memory to be a single rubidium atom trapped in a high finesse cavity. Each half of the entangled photon pair, perhaps distributed over up to 100 km of fiber, is sent into the cavity. The atomic qubit storage is required since an all-photon system could not fully measure the joint Bell state of the message and entangled qubits. The protocol checks whether the two memory atoms have each absorbed a photon before proceeding. Thus the system is limited by the rate at which suitable pairs can be created and distributed. These pairs need to have photons at the right frequency to excite the rubidium memory and need to have the right spatial mode to enter the high finesse cavity trapping the rubidium atom. This work is an attempt to create a bright source of suitable entangled pairs.

1.2 Entanglement Source

The workhorse of experimental quantum optics has been nonlinear $\chi^{(2)}$ crystals and $\chi^{(3)}$ fibers. Such materials can produce pairs of subharmonic photons via spontaneous parametric downconversion (SPDC) when driven with a phase-matched pump laser. Under the proper conditions these output pairs are polarization entangled. The bandwidth of the spontaneous pair generation is quite large, from 250 GHz to 5 THz. The proportion of the output which is within the ∼30 MHz bandwidth of the rubidium transition is 10^{-4} at best. When one takes into account the spatial mode matching into the atomic qubit cavity the rate of suitable pairs can be very low.

The optical parametric oscillator (OPO), constructed from a nonlinear material placed inside a cavity, has been well studied in the near-threshold regime where it produces squeezed signal and idler output beams. Far below threshold it acts as an optical parametric amplifier (OPA) and should produce discrete pairs instead of beams, i.e. the pair generation rate is less than the cavity decay rate so the cavity is on average empty of downconverted photons. These pairs should be produced primarily at the cavity resonances, and a type-II OPA, producing a pair with two different polarizations, would produce polarization entanglement. The proposed architecture of the source, detailed in Ref. [7], calls for using a combination of two such sources of narrowband polarization entanglement. The second OPA is used to avoid having a 50-50 beam splitter with a single OPA and losing half the pairs. This work is an attempt to create a single type-II OPA that generates degenerate polarization-entangled pairs at the 795 nm rubidium transition wavelength. Similar experiments, using type-I downconversion, which produces co-polarized photons, have been performed by Ou et al. [8, 9, 10] using type-I downconversion in a linear cavity, and by Kobayashi [11] using two type-I crystals in a ring cavity.

The nonlinear material used for SPDC is periodically potassium titanyl phosphate (PPKTP). The poling allows the pump and output pairs to be collinear and for the crystal to be relatively long, which contributes to the brightness of the narrowband output. The single-pass performance in producing polarization-entangled pairs was investigated first. The first chapter provides the theoretical basis for single-pass downconversion and the second chapter describes the corresponding experiments. The theory for the low-power OPA cavity is then presented, including spatial mode effects, in the following chapter. Then the experimental results for the cavity-produced polarization entanglement are detailed.

Chapter 2

Single Pass Theory

> The Mediterranean has the color of mackerel, changeable I mean. You don't always know if it is green or violet, you can't even say it's blue, because the next moment the changing reflection has taken on a tint of rose or gray.
>
> **Vincent Van Gogh**

This chapter presents a model of spontaneous parametric downconversion (SPDC) and specializes it for our experimental conditions. Some of the field notation that will be used here is derived in appendix A. The next section presents an overview of nonlinear $\chi^{(2)}$ material, and is followed by derivations of the SPDC optical state that emerges from the crystal. These derivations are not novel, but the non-perturbative derivation is generalized slightly and then applied to PPKTP. This result will also form part of the starting point for chapter 4. Based on this state several calculations related to experimental conditions and results are then presented. Numerical values are given where it will be useful to aid understanding an expressions or understand the next chapter's experiments.

2.1 Nonlinear Crystal

The induced polarization of some materials is more complicated than a linear dependence on the incident field. These nonlinear materials have higher order dependencies, usually expressed in tensor form as

$$P_i = \chi^{(1)}_{ij} E_j + \chi^{(2)}_{ijk} E_j E_k + \chi^{(3)}_{ijkl} E_j E_k E_l + ... \tag{2.1}$$

The i,j,k,l subscripts being from 1 to 3. The χ's are the electric susceptibilities, and for most materials the processes of interest are derived from the $\chi^{(2)}$ three-wave mixing or $\chi^{(3)}$ four-wave mixing terms. The downconversion in PPKTP is a three-wave mixing process. The second and third indices of $\chi^{(2)}_{ijk}$ are symmetric so the alternative notation d_{ab} is used where $a = i$ and b varies from 1 to 6 to represent jk values of 11, 22, 33, 23(32), 13(31), 12(21) (with extra factor of 2 so that d is half of χ: $2d_{ab} = \chi_{ijk}$) [12]. The KTP crystal has a mm2-orthorhombic crystal structure (space group Pna 2). This symmetry classification ensures that only 7 values of $\chi^{(2)}_{ijk}$ or 5 values of d_{ab} are not zero: d_{31}, d_{32}, d_{33}, d_{24}, and d_{15}.

We convert a pump with the electric field polarized along only the 2nd or y-axis, with signal output polarized along the 3rd or z-axis and idler output polarized along the 2nd or y-axis. The pump is continuous wave (cw) and propagating along the 1st or x-axis, and the signal and idler beams are emitted close to this direction. The d_{24} coefficient is thus responsible for the type-II downconversion seen in our experiments, and the rest of the tensor can be neglected [13].

This parametric process can only proceed if the requirements of the conservation laws of energy and momentum of the photons are met. The photon momenta inside the crystal depends on the indices of refraction; these are from the $\chi^{(1)}_{ij}$ tensor, and in the principal coordinate system of the crystal reduce to n_x, n_y, and n_z. Some nonlinear material, such as the commonly used beta-barium oxide (BBO), are uniaxial: two indices are identical and thus labeled ordinary, while the third index is labeled extraordinary and is also named the optic axis. KTP is a biaxial crystal: all three indices are different from one another, though in the case of KTP n_x differs only slightly from n_y. We take these indices from the Sellmeier equations and temperature dependence given in Ref. [14]. Having three distinct refractive indices produces two optic axes (thus the name biaxial) inclined at 17.65° to the z-axis in the yz-plane (value is at 795 nm), instead of a single optic axis. This lack of symmetry in a biaxial crystal creates slightly more complex formulas for wave propagation than in the uniaxial case [13]. This complexity is mitigated by the previously stated choice of aligning the pump to the x-axis, which essentially eliminates all first order corrections.

The desired process of converting from the ultraviolet (UV) to a degenerate infrared (IR) pair does not satisfy the momentum conservation laws in KTP: this process is not phase matched. Instead the KTP has been periodically poled which causes the sign of the d_{24} coefficient to alternate in each domain. This creates a position dependent $d_{24}(\boldsymbol{r})$ which replaces the usual momentum phase-matching condition with quasi-phase matching (QPM) condition [15]. By carefully choosing the poling period and adjusting the temperature of the crystal a quasi-phase-matching condition can be satisfied.

2.2 Output state from the crystal

The simplest derivation that is often presented involves calculating the biphoton state as a first order perturbation using the interaction Hamiltonian. The biphoton derivation ignores the possibility of emitting more than a single pair, but this is a good approximation for low power cw-pumped operation. This derivation also allows for a more realistic setup, i.e. non-plane-wave, pump beams. It gets the phase delay right due to a subtle choice of crystal location along the x-axis. It is derived here as a demonstration of how it is done with a quasi-phase-matched biaxial material.

A non-perturbative propagating field solution is possible for the plane-wave pump, and is derived after this biphoton derivation. It is clearer where the phase delay comes from, but harder to generalize the full solution beyond the plane-wave pump. The single-pass field solution is needed to build the cavity solution. In the low power limit this coincides with the biphoton solution.

For all the experiments, pump and idler have approximately horizontal (y-axis) polarization and the signal has vertical (z-axis) polarization. The deviation of the eigen-polarizations from exactly horizontal and vertical will be ignored in the paraxial approximation, just as the small deviation of d_{eff} from d_{24} will be ignored.

2.2.1 Perturbative Calculation

The downconversion interaction Hamiltonian in the crystal in terms of the electric-field operators [16, 17, 18, 19, 20]:

$$\widehat{H}_{int}(t) = \iiint_V d^3\boldsymbol{r}\, d_{24}(\boldsymbol{r})\widehat{E}_P^{+}(\boldsymbol{r},t)\widehat{E}_S^{+\dagger}(\boldsymbol{r},t)\widehat{E}_I^{+\dagger}(\boldsymbol{r},t) + H.c. \tag{2.2}$$

The integration over the crystal volume places the origin of $\boldsymbol{r}$ at the center of the output face of the crystal. This location of the origin produces the most immediately useful form of the biphoton amplitude.

Due to the small value of $|d_{24}(\boldsymbol{r})|$ the single-pass pump can be treated in the high-intensity and non-depleted classical limit. Thus $\widehat{E}_P^{+}$ will be replaced by the complex electric-field intensity E_P, with a profile $\widetilde{A}_P$:

$$E_P^{+}(\boldsymbol{r},t) = \iiint d^2\boldsymbol{q}d\omega\, i\sqrt{\frac{\hbar\omega}{2\epsilon_0 n_P(\boldsymbol{q},\omega)c}}\widetilde{A}_P(\boldsymbol{q},\omega)\frac{\exp(i\kappa_P(\boldsymbol{q},\omega)x + i\boldsymbol{q}\cdot\boldsymbol{s} - i\omega t)}{(2\pi)^{3/2}}, \tag{2.3}$$

where $\boldsymbol{s} \equiv (y, z)$ and κ is the function for k_x:

$$\kappa_{S,I,P}(\boldsymbol{q}, \omega) = \sqrt{\left(\frac{n_{S,I,P}(\boldsymbol{q}, \omega)\omega}{c}\right)^2 - |\boldsymbol{q}|^2}. \tag{2.4}$$

In the integrand in (2.2), the periodically-poled $d_{24}(\boldsymbol{r})$ can be approximated by an infinite crystal and expanded in a Fourier series:

$$d_{24}(\boldsymbol{r}) = \begin{cases} +d_{24} & \text{for } 0 < x \bmod \Lambda < 0.5\Lambda, \\ -d_{24} & \text{for } 0.5\Lambda < x \bmod \Lambda < \Lambda \end{cases}, \tag{2.5}$$

$$d_{24}(\boldsymbol{r}) = \sum_{m=1,3,5,\ldots} \frac{d_{eff}}{mi} \left(\exp\left(i\frac{2m\pi}{\Lambda}x\right) - \exp\left(-i\frac{2m\pi}{\Lambda}x\right)\right), \tag{2.6}$$

$$d_{eff} \equiv \left(\frac{2d_{24}}{\pi}\right), \tag{2.7}$$

where Λ is the poling period of the PPKTP crystal. For quasi-phase matching in the system under study, only the $\exp(\pm i\frac{2\pi}{\Lambda}x)$ terms contributes significantly to the integration. For other systems the ability to manufacture a short enough period to achieve matching can be lacking, in which case the next higher 3rd order term can be used instead. The definition above puts the origin $x = 0$ at a domain boundary; other possible locations along x result in a constant global phase shift in the Fourier series. This phase shift will not affect the results of experiments, much as the absolute phase of the pump will not affect the results. Experiments which, for instance, cascade two PPKTP crystals would depend on the exact locations of the domain boundaries, and the type of interactions involved. Phases that result from such subtleties do make comparing different authors' derivations more tedious.

The $\exp(\pm i\kappa_m x)$ terms from the fields combine with this term so that the quasi-matched output will depend on the momentum mismatch in the x direction, defined as

$$\Delta k(\boldsymbol{q}_S, \boldsymbol{q}_I, \omega_S, \omega_I) = \kappa_P(\boldsymbol{q}_S + \boldsymbol{q}_I, \omega_S + \omega_I) - \kappa_S(\boldsymbol{q}_S, \omega_S) - \kappa_I(\boldsymbol{q}_I, \omega_I) - \frac{2\pi}{\Lambda}. \tag{2.8}$$

The phase mismatch Δk will be zero for exact quasi-phase matching. In particular it will be frequently assumed that $\Delta k(\mathbf{0}, \mathbf{0}, \omega_P/2, \omega_P/2) = 0$ for forward degenerate phase matching.

For input vacuum states, the first order perturbation result for the output is a biphoton state with amplitude Φ. Expressing the signal and idler $\widehat{E}^{+\dagger}$ fields as integrals using (A.26) and rearranging leads to perturbation

$$\begin{aligned} |\Psi_{\text{bi}}\rangle &= \frac{i}{\hbar}\int_{-\infty}^{\infty} dt\, \widehat{H}_{int}(t)\, |0\rangle\,, \\ &= \iiint \iiint d^2\boldsymbol{q}_S d\omega_S d^2\boldsymbol{q}_I d\omega_I\, \Phi(\boldsymbol{q}_S, \boldsymbol{q}_I, \omega_S, \omega_I) \widehat{a}_S^\dagger(\boldsymbol{q}_S, \omega_S) \widehat{a}_I^\dagger(\boldsymbol{q}_I, \omega_I)\, |0\rangle\,, \end{aligned} \tag{2.9}$$

where the amplitude Φ includes the pump field and all other integrals. The leading $\sqrt{\omega_m/n_m(\boldsymbol{q}_m, \omega_m)}$ factors in the E_M^+ fields will be approximated by their forward ($\boldsymbol{q} = 0$) quasi-monochromatic value. This approximation will not be applied to the $\boldsymbol{q}_m$ and ω_m dependence in the exp(...) factors. The pump beam is well contained inside the crystal cross-section and thus diffraction can be ignored and the $\int dy$ and $\int dz$ integrals can have their limits taken to $\pm\infty$ without significant error. All the integrals in Φ can now be evaluated:

$$\mathcal{C} = \left(\frac{i}{\hbar}\right)\left(\frac{-d_{eff}}{i}\right)\sqrt{\frac{\omega_S\omega_I\omega_P}{n_S n_I n_P}}\left(\frac{\hbar}{2\epsilon_0 c}\right)^{3/2}\frac{i(-i)(-i)}{(2\pi)^{3/2}} \tag{2.10}$$

$$= \left(\frac{i d_{eff}}{\hbar}\right)\sqrt{\frac{\omega_S\omega_I\omega_P}{n_S n_I n_P}}\left(\frac{\hbar}{2\epsilon_0 c(2\pi)}\right)^{3/2} \tag{2.11}$$

$$\Phi(\boldsymbol{q}_S, \boldsymbol{q}_I, \omega_S, \omega_I) = \int_{-\infty}^{\infty} dt \int_{-L}^{0} dx \int_{-\infty}^{\infty} dy \int_{-\infty}^{\infty} dz \iiint \frac{d^2\boldsymbol{q}_P d\omega_P}{(2\pi)^3}$$
$$\mathcal{C}\widetilde{A}_P(\boldsymbol{q}_P, \omega_P) \exp(i\Delta k(\boldsymbol{q}_S, \boldsymbol{q}_I, \omega_S, \omega_I)x)$$
$$\exp(i(\boldsymbol{q}_P - \boldsymbol{q}_S - \boldsymbol{q}_I) \cdot \boldsymbol{s}) \exp(-i(\omega_P - \omega_s - \omega_I)t) \quad (2.12)$$

$$= \int_{-L}^{0} dx \iiint d^2\boldsymbol{q}_P d\omega_P \mathcal{C}\widetilde{A}_P(\boldsymbol{q}_P, \omega_P)$$
$$\exp(i\Delta k(\boldsymbol{q}_S, \boldsymbol{q}_I, \omega_S, \omega_I)x)\delta^2(\boldsymbol{q}_P - \boldsymbol{q}_S - \boldsymbol{q}_I)\delta(\omega_P - \omega_s - \omega_I) \quad (2.13)$$

$$= C\widetilde{A}_P(\boldsymbol{q}_S + \boldsymbol{q}_I, \omega_S + \omega_I)\frac{[1 - \exp\left(-iL\Delta k(\boldsymbol{q}_S, \boldsymbol{q}_I, \omega_S, \omega_I)\right)]}{i\Delta k(\boldsymbol{q}_S, \boldsymbol{q}_I, \omega_S, \omega_I)} \quad (2.14)$$

$$= C\widetilde{A}_P(\boldsymbol{q}_S + \boldsymbol{q}_I, \omega_S + \omega_I)L$$
$$\operatorname{sinc}\left(\frac{L\Delta k(\boldsymbol{q}_S, \boldsymbol{q}_I, \omega_S, \omega_I)}{2}\right) \exp\left(-i\frac{L\Delta k(\boldsymbol{q}_S, \boldsymbol{q}_I, \omega_S, \omega_I)}{2}\right). \quad (2.15)$$

The final amplitude shows that for this low-power regime the output is proportional to the $|\widetilde{A}_P L|^2$, but the sinc width is inversely proportional to L. So the low-power total downconversion rate is proportional to the product of the pump power and the crystal length.

2.2.2 Forward Plane-Waves

In a single plane-wave pump (pwp) model, which a large-focus Gaussian cw-pump beam of single frequency ω_P approximates, the pump profile is:

$$\widetilde{A}_P(\boldsymbol{q}_S + \boldsymbol{q}_I, \omega_S + \omega_I) = A_P\delta^2(\boldsymbol{q}_S + \boldsymbol{q}_I)\delta(\omega_P - \omega_S - \omega_I), \quad (2.16)$$

which reduces the bi-photon state to an integration over just the three signal photon variables. It is worth noting that $|A_P|$ has units of photons per area per time. The expressions for the biphoton reduce to

$$\Delta k(\boldsymbol{q}_S, \omega_S) = \kappa_P(0, \omega_P) - \kappa_S(\boldsymbol{q}_S, \omega_S) - \kappa_I(-\boldsymbol{q}_S, \omega_P - \omega_S) - \frac{2\pi}{\Lambda} \tag{2.17}$$

$$\Phi(\boldsymbol{q}_S, \omega_S) = \mathcal{C} A_P L \operatorname{sinc}\left(\frac{L\Delta k(\boldsymbol{q}_S, \omega_S)}{2}\right) \exp\left(-i\frac{L\Delta k(\boldsymbol{q}_S, \omega_S)}{2}\right) \tag{2.18}$$

$$|\Psi_{\text{bi,pwp}}\rangle = \iiint d^2\boldsymbol{q}_S d\omega_S \Phi(\boldsymbol{q}_S, \omega_S) \hat{a}_S^\dagger(\boldsymbol{q}_S, \omega_S) \hat{a}_I^\dagger(-\boldsymbol{q}_S, \omega_P - \omega_I) |0\rangle \,, \tag{2.19}$$

The pump has been reduced to the ultimate paraxial limit of $\boldsymbol{q} \to 0$, as in the case of weak pump beam focusing, but the output signal and idler still have appreciable off-axis amplitude. It is possible to filter the output state and collect only the cases where $\boldsymbol{q}_S$ is nearly zero: the forward output. The remaining state only depends on ω_S. Consider operation when the degenerate case ($\omega_S = \omega_I$) is exactly quasi-phase matched and let $\omega \equiv \omega_S - \omega_P/2$ be the detuning of the signal above degeneracy:

$$0 = \left(n_y(\omega_P)\omega_P - n_z(\omega_P/2)\omega_P/2 - n_y(\omega_P/2)\omega_P/2\right)\frac{1}{c} - \frac{2\pi}{\Lambda} \tag{2.20}$$

$$\Delta k(\mathbf{0}, \omega_S) = \left(n_y(\omega_P)\omega_P - n_z(\omega_S)\omega_s - n_y(\omega_P - \omega_S)(\omega_P - \omega_S)\right)\frac{1}{c} - \frac{2\pi}{\Lambda} \tag{2.21}$$

$$\begin{aligned}\Delta k(\mathbf{0}, \omega_S) = \Bigg(& n_y(\omega_P)\omega_P - n_z\left(\frac{\omega_P}{2} + \omega\right)\left(\frac{\omega_P}{2} + \omega\right) - \\ & n_y\left(\frac{\omega_P}{2} - \omega\right)\left(\frac{\omega_P}{2} - \omega\right)\Bigg)\frac{1}{c} - \frac{2\pi}{\Lambda}.\end{aligned} \tag{2.22}$$

The quasi-monochromatic limit means that $\omega << \omega_P/2$ so expanding n_z and n_y to first order in ω gives:

$$\Delta k(\mathbf{0}, \frac{\omega_P}{2} + \omega) \approx -\left(n_z\left(\frac{\omega_P}{2}\right) + n_z'\left(\frac{\omega_P}{2}\right)\frac{\omega_P}{2} - n_y\left(\frac{\omega_P}{2}\right) - n_y'\left(\frac{\omega_P}{2}\right)\frac{\omega_P}{2}\right)\frac{\omega}{c} \tag{2.23}$$

$$\Delta k(\mathbf{0}, \frac{\omega_P}{2} + \omega) \approx \Delta k'\frac{\omega}{c}, \tag{2.24}$$

which defines $\Delta k'$. The prime in $\Delta k'$ is, admittedly, an abuse of notation unless units were changed so that c is 1. But it is also worth noting that this $\Delta k'$ is dimensionless, and it depends only on the material and $\omega_P/2$; for KTP at 795 nm the value $\Delta k'$ is -0.10592. All the complexity of the polarization tensors, the biaxial crystal, and Sellmeier equations reduce in the forward limit to this single constant.

Using (2.24) the forward formulas for Φ can be simplified to:

$$\Phi(\mathbf{0},\omega) \approx \mathcal{C} A_P L \,\mathrm{sinc}\left(\frac{L\omega\Delta k'}{2c}\right) \exp\left(-i\frac{L\omega\Delta k'}{2c}\right) \tag{2.25}$$

$$|\Psi_{\text{bi,pwp,forward}}\rangle \approx \int d\omega\, \Phi(\mathbf{0},\omega)\widehat{a}_S^\dagger(\mathbf{0},\omega_P/2+\omega)\widehat{a}_I^\dagger(\mathbf{0},\omega_P/2-\omega)\,|0\rangle\,, \tag{2.26}$$

where for L of 1 cm this is, numerically:

$$\omega \rightarrow 2\pi f, \tag{2.27}$$

$$\Phi(\mathbf{0},2\pi f) \approx \mathcal{C} A_P(1\text{ cm})\,\mathrm{sinc}\left(\frac{f}{90.1\text{ GHz}}\right) \exp\left(-i\frac{f}{90.1\text{ GHz}}\right), \tag{2.28}$$

which is the source of the forward FWHM bandwidth of 251 GHz listed in table 2.1. For bandwidth defined between the first zeros of the sinc^2 function, instead of half maximum, the value is 566 GHz which spans 1.19 nm around the central 795 nm wavelength. So a 1 nm wide filter is closely matched to the SPDC of this system, and an ideal square 1 nm filter admits 90% of the output.

2.2.3 Non-Perturbative Calculation

It is possible to view the crystal as the concatenation of shorter crystals and consider the downconversion in each section. This limit should produce differential equations that connect the state in the crystal at position x with the state at $x + dx$. Such a differential equation can be derived either from Maxwell's equations including the nonlinear polarization and then quantized as in [21] or via a quantum description of spatial progression in nonlinear medium as in [22]. The latter derivation will be generalized and applied to the PPKTP system.

The generator for spatial progression is a momentum operator G and is used to compute the derivative of an operator S as

$$\frac{\partial \widehat{S}(x)}{\partial x} = \frac{i}{\hbar}\left[\widehat{S}(x), \widehat{G}(x)\right] \tag{2.29}$$

where $\widehat{G}(x)$ and $\widehat{S}(x)$ are composed of field creation and annihilation operators $\widehat{a}^{\pm}(\boldsymbol{q},\omega;x)$ and $\widehat{a}^{\pm\dagger}(\boldsymbol{q},\omega;x)$ which are defined in appendix A. These explicitly depend on the x coordinate, and obey the commutation relations in Eq. (A.15). They subsume the x dependence of the plane waves so that the electric field is now of the form

$$\widehat{E}^{\pm}_m(\boldsymbol{s},t;x) = \iiint d^2\boldsymbol{q}d\omega\, i\sqrt{\frac{\hbar\omega}{2\epsilon_0 n_m(\boldsymbol{q},\omega)c}}\frac{\exp(i(\boldsymbol{q}\cdot\boldsymbol{s}-\omega t))}{(2\pi)^{3/2}}\widehat{a}^{\pm}_m(\boldsymbol{q},\omega;x). \tag{2.30}$$

The linear generator of x progression, in vacuum or a medium, is $\widehat{G}(x)$:

$$\widehat{G}_0(x) = \sum_{j=1,2}\iiint d^2\boldsymbol{q}d\omega\,\hbar|\kappa_j(\boldsymbol{q},\omega)|\left(\widehat{a}_j^{+\dagger}(\boldsymbol{q},\omega;x)\widehat{a}_j^{+}(\boldsymbol{q},\omega;x) - \widehat{a}_j^{-\dagger}(\boldsymbol{q},\omega;x)\widehat{a}_j^{-}(\boldsymbol{q},\omega;x)\right). \tag{2.31}$$

This produces the expected result for progression:

$$\begin{align}
\frac{\partial \widehat{a}_m^{+}(\boldsymbol{q}',\omega';x)}{\partial x} &= \frac{i}{\hbar}\left[\widehat{a}_m^{+}(\boldsymbol{q}',\omega';x), \widehat{G}_0(x)\right] \tag{2.32}\\
&= \sum_{j=1,2}\iiint d^2\boldsymbol{q}d\omega\,\frac{i\hbar}{\hbar}|\kappa_j(\boldsymbol{q},\omega)|\left[\widehat{a}_m^{+}(\boldsymbol{q}',\omega';x), \widehat{a}_j^{+\dagger}(\boldsymbol{q},\omega;x)\widehat{a}_j^{+}(\boldsymbol{q},\omega;x)\right] \tag{2.33}\\
&= \sum_{j=1,2}\iiint d^2\boldsymbol{q}d\omega\, i\kappa_j(\boldsymbol{q},\omega)\delta^2(\boldsymbol{q}'-\boldsymbol{q})\delta(\omega'-\omega)\delta_{mj}\widehat{a}_j^{+}(\boldsymbol{q},\omega;x) \tag{2.34}\\
&= i\kappa_m(\boldsymbol{q}',\omega')a_m^{+}(\boldsymbol{q}',\omega';x). \tag{2.35}
\end{align}$$

This can be integrated to get back the explicit $\exp(i\kappa x)$ dependence, but now obviously relative to the origin of $x = 0$:

$$\widehat{a}_m^{\pm}(\boldsymbol{q}, \omega; x) = \exp(\pm i\kappa_m(\boldsymbol{q}, \omega))\widehat{a}_m^{\pm}(\boldsymbol{q}, \omega; 0). \tag{2.36}$$

This can also be exploited to evaluate commutators at different x coordinates by referring them both back to $x = 0$.

For the QPM downconversion the relevant nonlinear part of $\widehat{G}(x)$ is $\widehat{G}_{NL}(x)$ is (using $\boldsymbol{s} \equiv (y, z)$):

$$\widehat{G}_{NL}(x) = \iint d^2\boldsymbol{s} \int dt\, d_{24}(\boldsymbol{r}) \left(E_P^{+}(\boldsymbol{r}, t)\widehat{E}_S^{+\dagger}(s, t; x)\widehat{E}_I^{+\dagger}(s, t; x) + H.c.\right) \tag{2.37}$$

$$\begin{aligned}\widehat{G}_{NL}(x) = \iiint \iiint d^2\boldsymbol{q}_S d\omega_s d^2\boldsymbol{q}_I d\omega_I \, d_{eff}\sqrt{\frac{\hbar\omega_P}{2\epsilon_0 n_P c}}\sqrt{\frac{\hbar\omega_S}{2\epsilon_0 n_S c}}\sqrt{\frac{\hbar\omega_I}{2\epsilon_0 n_I c}}\frac{1}{(2\pi)^{3/2}} \\ \Bigg(\widetilde{A}_P(\boldsymbol{q}_S + \boldsymbol{q}_I, \omega_s + \omega_I)\widehat{a}_S^{+\dagger}(\boldsymbol{q}_S, \omega_s; x)\widehat{a}_I^{+\dagger}(\boldsymbol{q}_I, \omega_I; x) \\ \exp\left(i\kappa_p(\boldsymbol{q}_S + \boldsymbol{q}_I, \omega_S + \omega_I)x - i\frac{2\pi}{\Lambda}x\right) + H.c.\Bigg).\end{aligned} \tag{2.38}$$

Note that the above encodes specific choices of phase for the pump at $x = 0$ and the location of the crystal domain boundary at $x = 0$. For the monochromatic pump that will be considered this simplifies to

$$\begin{aligned}\widehat{G}_{NL}(x) = \iint \iint \int d^2\boldsymbol{q}_S d^2\boldsymbol{q}_I d\omega_S \, d_{eff}\sqrt{\frac{\omega_P\omega_S(\omega_P - \omega_S)}{n_P n_S n_I}}\left(\frac{\hbar}{2\epsilon_0 c(2\pi)}\right)^{3/2} \\ \Bigg(\widetilde{A}_P(\boldsymbol{q}_S + \boldsymbol{q}_I)\widehat{a}_S^{+\dagger}(\boldsymbol{q}_S, \omega_S; x)\widehat{a}_I^{+\dagger}(\boldsymbol{q}_I, \omega_P - \omega_S; x) \\ \exp\left(i\kappa_p(\boldsymbol{q}_S + \boldsymbol{q}_I)x - i\frac{2\pi}{\Lambda}x\right) + H.c.\Bigg).\end{aligned} \tag{2.39}$$

With the pump as a single forward plane-wave and frequency ω_P with A_P real:

$$\mathcal{K} \equiv \frac{d_{eff}}{\hbar}\sqrt{\frac{\omega_P\omega_S(\omega_P-\omega_S)}{n_P n_S n_I}}\left(\frac{\hbar}{2\epsilon_0 c(2\pi)}\right)^{3/2} A_P, \tag{2.40}$$

$$= -i\mathcal{C}A_P \tag{2.41}$$

$$\widehat{G}_{NL}(x) = \iiint d^2\boldsymbol{q}_S d\omega_s\, \hbar\mathcal{K}\Bigg(\widehat{a}_S^{+\dagger}(\boldsymbol{q}_S,\omega_S;x)\widehat{a}_I^{+\dagger}(-\boldsymbol{q}_S,\omega_P-\omega_s;x) \exp\left(i\kappa_p x - i\frac{2\pi}{\Lambda}x\right) + H.c.\Bigg) \tag{2.42}$$

This is the starting point for deriving the coupled progression equations for the down-conversion:

$$\frac{\partial\widehat{a}_{S,I}^{+}(\boldsymbol{q}_S,\omega_S;x)}{\partial x} = \frac{i}{\hbar}\left[\widehat{a}_{S,I}^{+}(\boldsymbol{q}_S,\omega_S;x), \widehat{G}_0(x)+\widehat{G}_{NL}(x)\right], \tag{2.43}$$

$$\frac{\partial\widehat{a}_S^{+}(\boldsymbol{q}_S,\omega_S;x)}{\partial x} = i\kappa_S(\boldsymbol{q}_S,\omega_S)\widehat{a}_S^{+}(\boldsymbol{q}_S,\omega_S;x) + i\mathcal{K}\widehat{a}_I^{+\dagger}(-\boldsymbol{q}_S,\omega_P-\omega_S;x)\exp\left(i\kappa_p x - i\frac{2\pi}{\Lambda}x\right), \tag{2.44a}$$

$$\frac{\partial\widehat{a}_I^{+}(\boldsymbol{q}_I,\omega_I;x)}{\partial x} = i\kappa_I(\boldsymbol{q}_I,\omega_I)\widehat{a}_I^{+}(\boldsymbol{q}_I,\omega_I;x) + i\mathcal{K}\widehat{a}_S^{+\dagger}(-\boldsymbol{q}_I,\omega_P-\omega_I;x)\exp\left(i\kappa_p x - i\frac{2\pi}{\Lambda}x\right). \tag{2.44b}$$

Change the signal and idler operators to simplify the equations:

$$\widehat{a}_S^{+}(\boldsymbol{q}_S,\omega_S;x) \to \exp(i\kappa_S(\boldsymbol{q}_S,\omega_S)x)\widetilde{a}_S(x), \tag{2.45a}$$

$$\widehat{a}_I^{+}(-\boldsymbol{q}_S,\omega_P-\omega_S;x) \to \exp(i\kappa_I(-\boldsymbol{q}_S,\omega_P-\omega_S)x)\widetilde{a}_I(x), \tag{2.45b}$$

so that only deviations from normal progression are important, leading to

$$\frac{\partial \widetilde{a}_S(x)}{\partial x} = i\mathcal{K}\exp(i(\kappa_P - \kappa_S(\boldsymbol{q}_S,\omega_S) - \kappa_I(-\boldsymbol{q}_S,\omega_P-\omega_S) - \frac{2\pi}{\Lambda})x)\widetilde{a}_I^\dagger(x) \tag{2.46a}$$

$$\frac{\partial \widetilde{a}_I(x)}{\partial x} = i\mathcal{K}\exp(i(\kappa_P - \kappa_S(\boldsymbol{q}_S,\omega_S) - \kappa_I(-\boldsymbol{q}_S,\omega_P-\omega_S) - \frac{2\pi}{\Lambda})x)\widetilde{a}_S^\dagger(x) \tag{2.46b}$$

$$\frac{\partial \widetilde{a}_S(x)}{\partial x} = i\mathcal{K}\exp(i\Delta k(\boldsymbol{q}_s,\omega_s,-\boldsymbol{q}_S,\omega_p-\omega_s)x)\widetilde{a}_I^\dagger(x) \tag{2.47a}$$

$$\frac{\partial \widetilde{a}_I(x)}{\partial x} = i\mathcal{K}\exp(i\Delta k(\boldsymbol{q}_s,\omega_s,-\boldsymbol{q}_S,\omega_p-\omega_s)x)\widetilde{a}_S^\dagger(x). \tag{2.47b}$$

Putting $\boldsymbol{r} = 0$ at the center of the output face, this can be solved (e.g. by Mathematica™) to give the output operators at $x = 0$ in terms of the input operators at $x = -L$:

$$\widetilde{a}_S(0) = \mu\widetilde{a}_S(-L) + \nu\widetilde{a}_I^\dagger(-L) \tag{2.48a}$$

$$\widetilde{a}_I(0) = \mu\widetilde{a}_I(-L) + \nu\widetilde{a}_S^\dagger(-L) \tag{2.48b}$$

$$\mu = \mu(\boldsymbol{q}_S,\omega_S) \equiv \exp(i\Delta kL/2)\left(\cosh(pL/2) - i\frac{\Delta kL}{2}\frac{\sinh(pL/2)}{pL/2}\right) \tag{2.49a}$$

$$\nu = \nu(\boldsymbol{q}_S,\omega_S) \equiv i\mathcal{K}L\exp(-i\Delta kL/2)\frac{\sinh(pL/2)}{pL/2} \tag{2.49b}$$

$$p \equiv \sqrt{|2\mathcal{K}|^2 - \Delta k^2} \tag{2.50}$$

$$1 = |\mu|^2 - |\nu|^2. \tag{2.51}$$

Transforming back to the $\widehat{a}_m^+$ operators gives

$$\begin{aligned}\widehat{a}_S^+(\boldsymbol{q}_S,\omega_S;0) =& \mu\Big(\widehat{a}_S(\boldsymbol{q}_S,\omega_S;-L)\exp(i\kappa_S(\boldsymbol{q}_S,\omega_S)L)\Big)+ \\ &\nu\Big(\widehat{a}_I^+(-\boldsymbol{q}_S,\omega_P-\omega_S;-L)\exp(i\kappa_I(-\boldsymbol{q}_S,\omega_P-\omega_S)L)\Big)^\dagger\end{aligned} \tag{2.52a}$$

$$\begin{aligned}\widehat{a}_I^+(-\boldsymbol{q}_S,\omega_P-\omega_S;0) =& \mu\Big(\widehat{a}_I(-\boldsymbol{q}_S,\omega_P-\omega_S;-L)\exp(i\kappa_I(-\boldsymbol{q}_S,\omega_P-\omega_S)L)\Big)+ \\ &\nu\Big(\widehat{a}_S^+(\boldsymbol{q}_S,\omega_S;-L)\exp(i\kappa_S(\boldsymbol{q}_S,\omega_S)L)\Big)^\dagger.\end{aligned} \tag{2.52b}$$

In the absence of the nonlinear coupling μ is 1 and ν is zero and the solution above is just the standard phase difference going through the medium.

The solution can be inverted to solved for the input annihilation operators in terms of the output ones. Since the eigenvalues of those input operators with a vacuum input state are zeros, this leads to equations of the output operators on the output state that equal zero. These can be solved when the number of signal and idler photons is equal, and the solution is a Bose-Einstein distribution of pairs:

$$\begin{aligned}|\Psi; x=0\rangle = \iint d^2\boldsymbol{q}d\omega \, \frac{1}{\mu(\boldsymbol{q},\omega,-\boldsymbol{q},\omega_P-\omega)} \sum_{n=0}^{\infty} \left(\frac{\nu(\boldsymbol{q},\omega,-\boldsymbol{q},\omega_P-\omega)}{\mu(\boldsymbol{q},\omega,-\boldsymbol{q},\omega_P-\omega)^*}\right)^n \\ \Big(\widehat{a}_S^{+\dagger}(\boldsymbol{q},\omega;0)\widehat{a}_I^{+\dagger}(-\boldsymbol{q},\omega_P-\omega;0)\Big)^n |0; x=0\rangle\end{aligned} \tag{2.53}$$

In the low power limit when A_P is very small we can assume $|\mathcal{K}| \ll \Delta k$ and $|\mathcal{K}L| \ll 1$, and thus

$$p \approx i|\Delta k| \tag{2.54}$$

$$\mu(L) \approx 1 \tag{2.55}$$

$$\nu(L) \approx i\mathcal{K}L\,\mathrm{sinc}(\Delta k L/2)\exp(-i\Delta k L/2). \tag{2.56}$$

In this limit the term $\nu(L)\,|1\rangle_S \otimes |2\rangle_I$ matches the perturbative result (2.15) for the biphoton amplitude up to phase factor of $-i$, which is global and will not affect

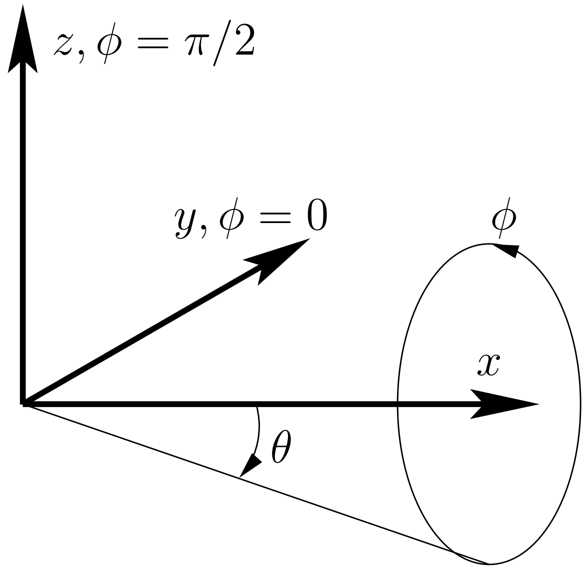

Figure 2-1: Diagram of coordinate system in PPKTP crystal. The x, y, and z are the crystal axes. The pump propagates in the $+x$ direction. The θ coordinate is the the off-axis angle measured from x. The ϕ coordinate indicates which transverse direction, measured in the y-z plane from y.

measurements.

2.3 Calculations

2.3.1 Tuning and Tolerances

Consider the non-forward output while keeping the pump as a plane wave. To be concrete, take the numbers for the index of refraction of PPKTP (from Ref. [14]) with $\Lambda = 8.88$ µm and tuned for forward phase-matching at degeneracy when at 25°C. Use a spherical coordinate system for the signal beam direction (in air) with $\theta = 0$ along the x axis and ϕ from y to z. The expression for Δk in leading orders gives:

$$\Delta k \approx 0.1996 dT + 6.083 dp - 2.220 df + 53.16 q_y^2 + 57.03 q_z^2 \tag{2.57}$$

$$\Delta k \approx 0.1996 dT + 6.083 dp - 2.220 df + \left(1.012 \cos(\phi)^2 + 1.085 \sin(\phi)^2\right) d\theta^2 \tag{2.58}$$

Variable	FWHM
dT	2.78°C
dp	91.5 GHz
df	251 GHz
q_y	.145 rad/µm
q_z	.140 rad/µm
$d\theta$	1.01°– 1.05°

Table 2.1: Tuning ranges of Eq. (2.58) for 10 mm crystal. The q can be compared to $|\boldsymbol{k}| \approx 7.90$ rad/µm.

- Δk: phase mismatch per crystal length in radians per mm
- dT: temperature difference in °C
- dp: pump detuning in THz
- df: signal detuning above degeneracy in THz
- $d\theta$: angle between signal beam and x axis (degrees)
- ϕ: angle around x axis of signal beam from y to z
- $q_{y,z}$: transverse wave vector (radians per µm)

The most important dropped term was $-.009259 df^2$ and is only -0.0058331 radians for a 10 mm crystal when df is 251 GHz. So the expansion above is a very good approximation near degeneracy. The almost round nature of the output is also apparent, and can be approximated by a circular $55.10|\boldsymbol{q}|^2$ or $1.048 d\theta^2$.

With a $L = 10$ mm crystal the full-width half-maximum (FWHM) tuning tolerances, i.e. $\mathrm{sinc}(\Delta k L/2)^2 = 1/2$, are shown in Table 2.1. From Eq. (2.58), a temperature change of 10 mK is balanced by a shift in df of less than 1 GHz. Thus the quasi-phase matching is stable against small temperature fluctuations. Tuning the temperature dT is the preferred way to achieve degenerate phase matching, as opposed to trying to tune the pump frequency dp.

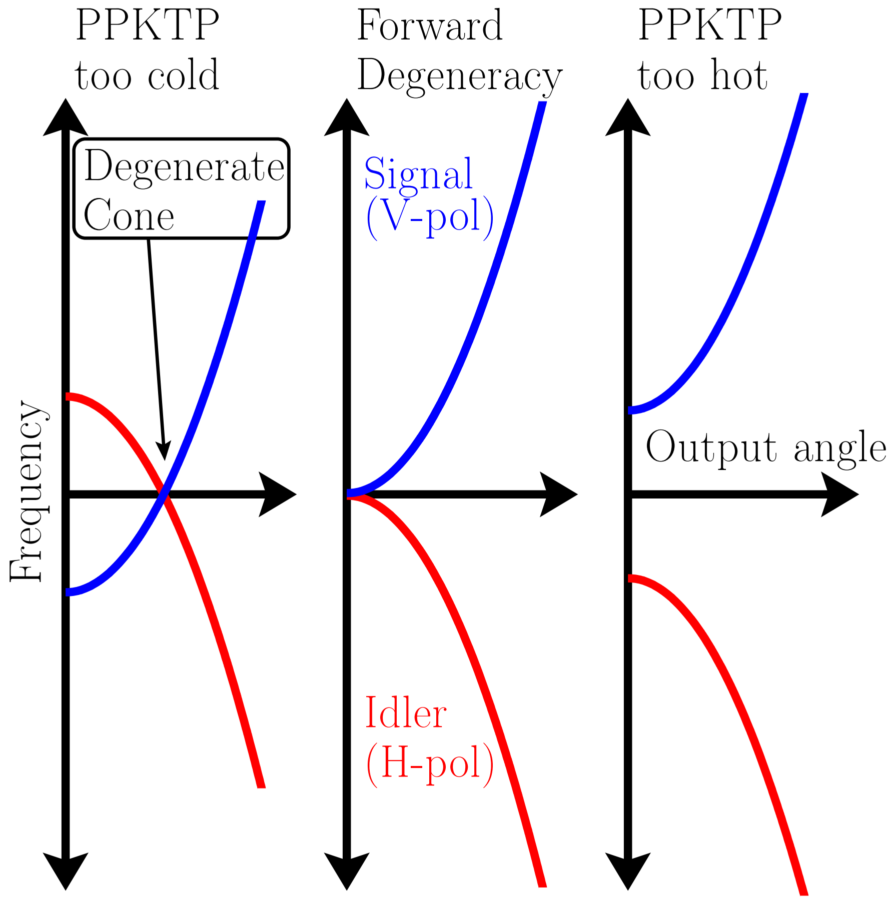

Figure 2-2: Illustration of the phase matched output frequencies of the signal and idler beams versus output angle for three temperatures. On the left, the output is degenerate at a non-zero angle, in the middle the forward output is degenerate, and on the right none of the output pairs have degenerate frequencies.

2.3.2 Degenerate Cone

Maintaining phase matching ($\Delta k = 0$) as the angle is varied causes the central frequency of z-polarized signal beam to detune to higher frequencies while the idler beam detunes to lower frequencies ($df > 0$). If the forward output is frequency degenerate, then this makes the off-axis pairs increasingly distinguishable. For $d\theta$ of 1° the detuning is about 0.49 THz (≈ 1 nm).

The off-axis output can be made degenerate if the temperature or the pump is tuned, as shown in Fig. 2-2. The degenerate output can be changed from forward into a cone. If the temperature is lowered below that of forward degeneracy, then the system still has degenerate outputs in a cone of some finite angle. This has been observed experimentally in our group by Marco Fiorentino [23]. The cones are almost but not exactly circular, with a few percent difference between horizontal and vertical widths. The degenerate pairs in the cone are non-collinear which avoids the 50-50 beam splitter used to separate 50% of the forward collinear output (and lose the other 50% which does not separate at the beam splitter).

2.3.3 Correlation Functions

Calculations of the properties of the output pairs can often be simplified to a few correlation function building blocks. These can be derived fairly simply from the non-perturbative result at the output face by substituting back to the input face with vacuum inputs. Let $\omega_0 \equiv \omega_P/2$ and expand the expression for Δk about forward degenerate operation; Fourier integrals over frequency are extended to $\pm\infty$ since the sinc function will limit the bandwidth:

$$\widehat{a}_S^{\pm}(\boldsymbol{q}, t; x) \equiv \int d\omega\, \widehat{a}_S^{\pm}(\boldsymbol{q}, \omega_0 + \omega; x) \frac{\exp(-i(\omega_0 + \omega)t)}{\sqrt{2\pi}} \tag{2.59}$$

$$\widehat{a}_I^{\pm}(\boldsymbol{q}, t; x) \equiv \int d\omega\, \widehat{a}_I^{\pm}(\boldsymbol{q}, \omega_0 - \omega; x) \frac{\exp(-i(\omega_0 - \omega)t)}{\sqrt{2\pi}} \tag{2.60}$$

$$[a_m^{\pm}(\boldsymbol{q}, t; x), a_{m'}^{\pm}{}^{\dagger}(\boldsymbol{q}', t'; x)] = \delta_{m,m'} \delta^2(\boldsymbol{q} - \boldsymbol{q}')\delta(t - t') \tag{2.61}$$

$$\Delta k(\boldsymbol{q}, \omega_0 + \omega) \approx \Delta k' \omega/c + \Delta k_y q_y^2 + \Delta k_z q_z^2. \tag{2.62}$$

First calculate the normally ordered correlation function for a vacuum state:

$$\begin{aligned}\langle \widehat{a}_S^{+\dagger}(\boldsymbol{q}_1, t_1; 0)\widehat{a}_S^{+}(\boldsymbol{q}_2, t_2; 0)\rangle = &\iint \frac{d\omega_1 d\omega_2}{2\pi}\ \exp(i(\omega_0+\omega_1)t_1 - i(\omega_0+\omega_2)t_2)\\ &\quad \exp(iL(\kappa_I(-\boldsymbol{q}_2, \omega_0-\omega_2) - \kappa_I(-\boldsymbol{q}_1, \omega_0-\omega_1)))\\ &\Big\langle \nu(\boldsymbol{q}_1, \omega_0+\omega_1)^* \widehat{a}_I^{+}(-\boldsymbol{q}_1, \omega_0-\omega_1; -L)\\ &\quad \nu(\boldsymbol{q}_2, \omega_0+\omega_2)\widehat{a}_I^{+\dagger}(-\boldsymbol{q}_2, \omega_0-\omega_2; -L)\Big\rangle \end{aligned} \tag{2.63}$$

$$\begin{aligned} =&\delta^2(\boldsymbol{q}_1-\boldsymbol{q}_2)\exp(i\omega_0(t_1-t_2))\\ &\int \frac{d\omega_1}{2\pi}\ |\nu(\boldsymbol{q}_1, \omega_0+\omega_1)|^2 \exp(i\omega_1(t_1-t_2)) \end{aligned} \tag{2.64}$$

$$\begin{aligned} =&\exp\left(i\left(\omega_0 - c\frac{\Delta k_y q_y^2 + \Delta k_z q_z^2}{\Delta k'}\right)(t_1-t_2)\right)\\ &\delta^2(\boldsymbol{q}_1-\boldsymbol{q}_2)\frac{c|\mathcal{K}|^2 L}{|\Delta k'|}\max\left(0, 1-\frac{c|t_1-t_2|}{|\Delta k'|L}\right) \end{aligned} \tag{2.65}$$

$$\begin{aligned} =&\exp\left(i\left(\omega_0 - c\frac{\Delta k_y q_y^2 + \Delta k_z q_z^2}{\Delta k'}\right)(t_1-t_2)\right)\\ &\delta^2(\boldsymbol{q}_1-\boldsymbol{q}_2)K_{SS}^{(n)}(t_S-t_I). \end{aligned} \tag{2.66}$$

The normal ordered correlation above is thus a “triangle-shaped” function that depends only on $t_1 - t_2$, and is nonzero for $|t_1 - t_2|$ less than $|\Delta k'|L/c$. The analogous function for the idler is the same since it is even in $\boldsymbol{q}$. The phase sensitive correlation function is

$$\begin{aligned}\langle \widehat{a}_S^+(\boldsymbol{q}_1, t_S; 0)\widehat{a}_I^+(\boldsymbol{q}_2, t_I; 0)\rangle = &\iint \frac{d\omega_1 d\omega_2}{2\pi} \exp(-i(\omega_0+\omega_1)t_S - i(\omega_0-\omega_2)t_I)\\ &\exp(i\kappa_S(\boldsymbol{q}_1,\omega_0+\omega_1)L - i\kappa_S(-\boldsymbol{q}_2,\omega_0+\omega_2)L)\\ &\Big\langle \mu(\boldsymbol{q}_1,\omega_0+\omega_1)\widehat{a}_S^+(\boldsymbol{q}_1,\omega_0+\omega_1;-L) \qquad (2.67)\\ &\nu(-\boldsymbol{q}_2,\omega_0+\omega_2)\widehat{a}_S^{+\dagger}(-\boldsymbol{q}_2,\omega_0+\omega_2;-L)\Big\rangle\end{aligned}$$

$$\begin{aligned}=&\delta^2(\boldsymbol{q}_1+\boldsymbol{q}_2)\exp(-i\omega_0(t_S+t_I))\\ &\int \frac{d\omega_1}{2\pi}\exp(-i\omega_1(t_S-t_I))\mu(\boldsymbol{q}_1,\omega_0+\omega_1)\nu(\boldsymbol{q}_1,\omega_0+\omega_1) \qquad (2.68)\end{aligned}$$

$$\begin{aligned}=&\exp\left(-i\omega_0(t_S+t_I) + ic\frac{\Delta k_y q_x^2 + \Delta k_y q_y^2}{\Delta k'}(t_S-t_I)\right)\\ &\delta^2(\boldsymbol{q}_1+\boldsymbol{q}_2)\frac{ic\mathcal{K}}{|\Delta k'|}\begin{cases}1, & (t_S-t_I)\in[0,\frac{-\Delta k' L}{c}]\\ 0, & \text{otherwise.}\end{cases} \qquad (2.69)\end{aligned}$$

$$\begin{aligned}=&\exp\left(-i\omega_0(t_S+t_I) + ic\frac{\Delta k_y q_x^2 + \Delta k_y q_y^2}{\Delta k'}(t_S-t_I)\right)\\ &\delta^2(\boldsymbol{q}_1+\boldsymbol{q}_2)K_{SI}^{(p)}(t_S-t_I) \qquad (2.70)\end{aligned}$$

This is also equal to $\langle \widehat{a}_I^+(\boldsymbol{q}_2, t_I; 0)\widehat{a}_S^+(\boldsymbol{q}_1, t_S; 0)\rangle$ since they commute. Since $\Delta k' < 0$ this means that the function is non-zero for $0 \le (t_S - t_I) \le -\Delta k' L/c$. For 10 mm of KTP this delay is ∼3.5 ps. The other distinct correlation functions $\langle \widehat{a}_m^+ \widehat{a}_m^+\rangle$ and $\langle \widehat{a}_S^{+\dagger} \widehat{a}_I^+\rangle$ are zero using the non-perturbative operators at $x = -L$ without needing the low power limit. The rest of the permutations are conjugates of those presented above.

The $\boldsymbol{q}$ dependent phase shifts can be observed. Taking $\boldsymbol{q}$ to be in radians per µm, the values of $c\Delta k_{y,z}/\Delta k'$ for KTP are -150.5 and -161.4 radians per picosecond. The calculation can be done in general instead of the forward plane-wave limit, in which case the factor

$$c\frac{\Delta k_y q_x^2 + \Delta k_y q_y^2}{\Delta k'}(t_S - t_I) \tag{2.71}$$

is replaced by an expansion of Δk using the values for KTP at 795 nm with the pump along x:

$$-\left(0.5649dT + 17.22dp + \left(2.863\cos(\phi)^2 + 3.071\sin(\phi)^2\right) d\theta^2\right)(t_S - t_I), \qquad (2.72)$$

where $t_S - t_I$ is in picoseconds and the rest are as defined previously: ϕ and $d\theta$ in degrees, dT in °C, and dp in THz. For the circular approximation set ϕ to $\pi/4$ and obtain an average value of $2.967d\theta^2$ for the phase shift. This extra phase shift comes from the center of the signal and idler bandwidths moving away from degeneracy in response to the other terms. This lack of exact degeneracy creates distinguishability which will reduce the observable polarization entanglement.

2.3.4 Timing compensation

The birefringence inherent in the type-II downconversion means that after the pair of signal and idler photons are created at a single moment and position they will then travel at different speeds on their way out of the crystal. For simplicity of discussion, consider only forward output. The idler photon, having the smaller index n_y, will always exit ahead of the signal photon. The actual delay depends on not just the indices but also their first-order dependence on frequency (i.e. the dispersion).

Thus the signal and idler can be delayed by any time between the whole delay from being born at the input face of the crystal to the zero delay from being born at the output face of the crystal. This range of uniformly probable delays can be derived from the wave function as done in Ref. [18]. Let t_S and t_I be the times when the photons are detected upon leaving the crystal. Then the rate involves calculation $\langle \widehat{\boldsymbol{E}}_S^{+\dagger}(t_S)\widehat{\boldsymbol{E}}_S^{+}(t_S)\widehat{\boldsymbol{E}}_I^{+\dagger}(t_I)\widehat{\boldsymbol{E}}_I^{+}(t_I)\rangle$ which simplifies at low power to a function of $|K_{SI}^{(p)}(t_S - t_I)|^2$. This gives the time window for detecting pair coincidences coming out of the crystal.

For conciseness let $T \equiv -\Delta k' L/(2c) > 0$. The first photon to leave the crystal and be detected is always the idler, thus $0 \leq t_S - t_I \leq 2T$. This condition creates distinguishability between signal and idler and prevents polarization entanglement. The timing distinguishing information can be erased by adding an opposite delay of T, half the maximum delay. This could be added by separating, delaying, and recombining the signal and idler or be added by inserting a birefringent compensating crystal: usually a rotated piece of KTP which is half the length of the PPKTP crystal. After the compensation, the signal or idler may arrive first, thus $-T \leq t_S - t_I \leq T$. Knowing the time delay between clicks, the absolute value $|t_s - t_I|$, no longer distinguishes which click was the idler. Thus the distinguishing information has been erased.

2.4 Interference dip

The polarization-entanglement can be demonstrated by a means which resembles a Hong-Ou-Mandel dip [1]. This measurement is similar to measuring the center of the dip, for which the coincidence rate of polarization-entangled photons is ideally zero. For unentangled photons the rate is ideally half the pair generation rate. Thus the degree of polarization-entanglement can be measured.

The forward output is measured in a 45° polarization basis that separates the $(|H\rangle + |V\rangle)/\sqrt{2}$ transmitted and $(|H\rangle - |V\rangle)/\sqrt{2}$ reflected states. Let the idler ($|H\rangle$) modes be timing compensated by a variable delayed of T' seconds. To simplify the calculation further, assume a filter of some kind is used to pass only a single spatial mode to the transmitted and reflected detectors. These modes are defined by function

$f_{T,R}(\boldsymbol{q})$ as:

$$\widehat{a}^{+}_{S,I}(t;x;T,R) = \iint d^2\boldsymbol{q}\, f_{T,R}(\boldsymbol{q})\widehat{a}^{+}_{S,I}(\boldsymbol{q},t;x) \tag{2.73}$$

$$1 = \iint d^2\boldsymbol{q}\ |f_{T,R}(\boldsymbol{q})|^2 \tag{2.74}$$

$$f_R(\boldsymbol{q}) = f_T(-\boldsymbol{q})^* \tag{2.75}$$

$$|f_T(\boldsymbol{q})|^2 \to \delta^2(\boldsymbol{q}_0 - \boldsymbol{q}) \tag{2.76}$$

$$\left[\widehat{a}^{+}_{m}(t_1;x;n), \widehat{a}^{+}_{m'}{}^{\dagger}(t_2;x;n)\right] = \delta_{mm'}\delta(t_1 - t_2) \tag{2.77}$$

The limit of $|f|^2$ to a delta function will be taken at the end.

Coincidences are measured between detectors for these separated beams. The detectors now count for time T_M the superposed modes $|H\rangle + |V\rangle$ and $|H\rangle - |V\rangle$ given by the $\widehat{a}_T$ and $\widehat{a}_R$, respectively:

$$\widehat{a}_T(t_1) \equiv (\widehat{a}^{+}_S(t_1;0;T) + \widehat{a}^{+}_I(t_1 - T';0;T))/\sqrt{2} \tag{2.78}$$

$$\widehat{a}_R(t_2) \equiv (\widehat{a}^{+}_S(t_2;0;R) - \widehat{a}^{+}_I(t_2 - T';0;R))/\sqrt{2} \tag{2.79}$$

$$\widehat{N}_T \equiv \int_0^{T_M} dt_T\, \widehat{a}^{\dagger}_T(t_T)\widehat{a}_T(t_T) \tag{2.80}$$

$$\widehat{N}_R \equiv \int_0^{T_M} dt_R\, \widehat{a}^{\dagger}_R(t_R)\widehat{a}_R(t_R) \tag{2.81}$$

The coincidences detected are then N:

$$N = \langle\Psi|\widehat{N}_T\widehat{N}_R|\Psi\rangle \tag{2.82}$$

$$N = \iint dt_T dt_R\ \langle\Psi|\widehat{a}^{\dagger}_T(t_T)\widehat{a}^{\dagger}_R(t_R)\widehat{a}_T(t_T)\widehat{a}_R(t_R)|\Psi\rangle \tag{2.83}$$

There will be a change of time variable to the average time $t_0 \equiv (t_T + t_R)/2$ and difference $\delta t \equiv t_S - t_I$. Ignoring accidental coincidences in the low power limit, N

simplifies to

$$N = \iint dt_T dt_R \left|\langle 0|\widehat{a}_T(t_T)\widehat{a}_R(t_R)|\Psi\rangle\right|^2 \tag{2.84}$$

$$N = \iint dt_0 d\delta t \left|\frac{1}{2}\int d\omega\ \exp(-i\omega T')\mu(\boldsymbol{q}_0,\omega)\nu(\boldsymbol{q}_0,\omega)\Big(\exp(i\omega\delta t) - \exp(-i\omega\delta t)\Big)\right|^2. \tag{2.85}$$

The time scales for T are picoseconds compared to T_M of microseconds, so that details of the range of integration of δt at the limits of t_0 will be ignored. Use the low power limit of μ and ν. The expansion of Δk from Eq. (2.72) will be used to compute $Q(\boldsymbol{q})$.

$$Q(\boldsymbol{q}) \equiv \frac{c}{\Delta k'}\left(\Delta k_y q_y^2 + \Delta k_z q_z^2 + \Delta k_{dp} dp + \Delta k_{dT} dT\right) \tag{2.86}$$

$$T \equiv -\Delta k' L/(2c), \quad \text{so that } (T > 0) \tag{2.87}$$

$$\text{box}(\tau) \equiv \begin{cases} 1, & -T < \tau < T \\ 0, & \text{otherwise.} \end{cases} \tag{2.88}$$

$$N = \frac{T_M|\mathcal{K}L|^2}{(4T)^2}\int d\delta t \Big| \exp(iQ(\boldsymbol{q}_0)\delta t)\,\text{box}(\delta t + (T - T')) - \exp(-iQ(\boldsymbol{q}_0)\delta t)\,\text{box}(\delta t - (T - T'))\Big|^2 \tag{2.89}$$

$$N = \frac{T_M\,|\mathcal{K}L|^2}{4T}\begin{cases} 1 - \frac{T'}{T}\,\text{sinc}(2Q(\boldsymbol{q}_0)T'), & 0 \le T' \le T \\ 1 - \frac{2T-T'}{T}\,\text{sinc}(2Q(\boldsymbol{q}_0)(2T - T')), & T \le T' \le 2T \\ 1, & \text{otherwise.} \end{cases} \tag{2.90}$$

And for the optimal phase matching Q is zero and the famous triangular dip is obtained. At $T' = T$, the $1-$sinc() term can be up to 1.217, exceeding the background level of 1. With $T' = T$ and the forward direction phase matched, $Q(\mathbf{0}) = 0$, the value of N is zero and rises to 0.001 at $\theta = 0.086°$ and 0.01 of the standard value at $\theta = 0.153°$. This sets the scale of how much of the forward output can be collected to get an entangled beam. For temperature tuning the 0.001 and 0.01 values for dT are respectively 0.069°C and 0.217°C.

A more detailed calculation would need to consider the rate of accidental coincidences, which scales as $|\mathcal{K}L|^4$ from the $|\nu|^4$ dependence. Most experiments also employ frequency filtering, which has the general effect of rounding off the triangular dip and make it wider [18].

2.5 Entanglement inequality

A standard way to verify polarization entanglement is to test one of Bell's inequalities. The "CHSH" test, as originally presented in Ref. [24], is testable with photon pairs and the standard (not number-resolving) photon counters. The formulation is essentially the same as presented in Ref [25], and involves measuring 16 coincidence rates.

The timing-compensated forward bi-photon state when degenerate can be described by the polarization state:

$$|\Psi;t\rangle = |H;t\rangle \otimes |V;t\rangle \,. \tag{2.91}$$

The output is sent through a 50-50 beam splitter and after the beam splitter the state is

$$\begin{aligned} |\Psi_{split};t\rangle = \Big(&|H;t\rangle_T \otimes |V;t\rangle_R + |H;t\rangle_R \otimes |V;t\rangle_T \\ &- |H;t\rangle_T \otimes |V;t\rangle_T - |H;t\rangle_R \otimes |V;t\rangle_R\Big)/2. \end{aligned} \tag{2.92}$$

The TT and RR events are ignored, as they do not cause coincidences, and only the TR and RT events are post-selected. This post-selected state is a triplet state

$$|\Psi_{triplet};t\rangle = \Big(|H;t\rangle_T \otimes |V;t\rangle_R + |H;t\rangle_R \otimes |V;t\rangle_T\Big)/\sqrt{2} \otimes |Other\rangle \tag{2.93}$$

The transmitted photon is analyzed in a rotated linear polarization basis (θ_T) using two detectors (called TT and TR) and likewise for the reflected photon (θ_R basis with detectors RT and RR). The four coincidence rates between one transmitted and one reflected detector are measured. Define

$$E(\theta_T, \theta_R) \equiv \frac{C_{TT,RT}(\theta_T, \theta_R) + C_{TR,RR}(\theta_T, \theta_R) - C_{TR,RT}(\theta_T, \theta_R) - C_{TT,RR}(\theta_T, \theta_R))}{C_{TT,RT}(\theta_T, \theta_R) + C_{TR,RR}(\theta_T, \theta_R) + C_{TR,RT}(\theta_T, \theta_R) + C_{TT,RR}(\theta_T, \theta_R))} \tag{2.94}$$

$$-1 \leq E(\theta_T, \theta_R) \leq +1 \tag{2.95}$$

using the four coincidence rates for a given pair of analysis angles. Four combinations of measurements are taken by choosing a pair of bases in the transmitted path and a different pair in the reflected path. Then the inequality can be expressed using the sum of three E functions minus the fourth:

$$S(\theta_T, \theta'_T, \theta_R, \theta'_R) \equiv E(\theta_T, \theta_R) + E(\theta'_T, \theta_R) + E(\theta_T, \theta'_R) - E(\theta'_T, \theta'_R) \tag{2.96}$$

$$|S(\theta_T, \theta'_T, \theta_R, \theta'_R)| \leq 2 \qquad \text{local, classical} \tag{2.97}$$

$$|S(\theta_T, \theta'_T, \theta_R, \theta'_R)| \leq 2\sqrt{2} \quad \text{non-local, quantum} \tag{2.98}$$

For a polarization-entangled beam there will be some set of four angles which will exhibit a violation of the $|S| \leq 2$ condition. The choice of analysis angles is $\{0, \pi/4\}$ for $\{\theta_T, \theta'_T\}$, and $\{\pi/8, 3\pi/8\}$ for $\{\theta_R, \theta'_R\}$. In practice the measured rates will have statistical noise and the value of S will have some error range, and so S will be above 2 to some degree of confidence, e.g. some multiple of the standard deviation. In a given measurement time there is a fundamental trade off: tighter filtering of the output state improves the purity of polarization entanglement but reduces the count rate and increases the error range of the final value. And tighter filtering cannot be compensated with increasing the power of the pump beam beyond the point where either the detectors saturate or the low power limit breaks down and multiple-pair downconversion spoils the measurement.

Chapter 3

Single Pass Experiments

> I prepared excitedly for my departure, as if this journey had a mysterious significance. I had decided to change my mode of life. "'til now," I told myself, "you have only seen the shadow and been well content with it; now, I am going to lead you into the substance."
>
> **Nikos Kazantzakis**, *Zorba the Greek*

Before building the novel cavity source, the nonlinear PPKTP was tested in a simpler configuration. The crystal was pumped and the downconverted pairs were collected via free-space optics onto the single-photon detectors. This allowed us to learn the parameters to achieve quasi-phase matching with our individual crystal. The collinear pump and output along the x-axis allowed us to use a longer crystal than angle-phase matching, noncollinear techniques which are limited by walk off. This PPKTP source thus obtained was a high-flux source of excellent quality polarization entanglement [26].

3.1 Path of Illumination

The pump light for the down-converter was derived from a continuous-wave (cw) external-cavity UV-diode laser, made by Toptica. The frequency was adjusted by tilting the stabilizing feedback grating. The operating wavelength range was 397.25 nm to 397.5 nm (in vacuum). The laser output power was approximately 10 mW and the pump was weakly focused to a large ∼200-µm beam waist with the focus in the down-conversion crystal, which corresponds to a 31-cm Rayleigh range (half the b-parameter of the Gaussian beam [27]). The crystal used was a ∼10-mm long (x-axis) periodically-poled flux-grown potassium titanyl phosphate (PPKTP) crystal. The period of the grating was 8.84 µm, so that the horizontally polarized pump produced frequency-degenerate type-II quasi-phase-matched collinear (forward) output when operating near room temperature (15°C to 21°C). The exact temperature of the PPKTP could be controlled by a thermo-electric cooler and monitored by a thermistor in order to achieve degenerate operation at the desired pump wavelength[1]. The input and output PPKTP crystal faces have an anti-reflection (AR) coating at 795 nm and are 4.5-mm wide (y-axis) 1-mm high (z-axis); large enough to ignore diffraction effects.

Removing the pump from the collinear SPDC output was accomplished using three dichroic mirrors which reflected the UV and had high transmission in the IR. They were placed right after the PPKTP so that the UV would not reach any other elements, because most of the optics fluoresce when exposed to UV, and some of that emission is in the same frequency bandwidth as the collected down-converted photons. These mirrors were set at a slight angle so as to dump the pump beam outside of the main optical axis of the system, adjusting one dichroic mirror to dump left and the others right so that the net beam displacement was negligible.

The next optical element was the timing compensation crystal (KTPcc). This had 3 mm by 3 mm faces and was 5 mm long, with the same AR coating as the PPKTP crystal. It was rotated 90° so that its z-axis and y-axis were interchanged with respect to the PPKTP crystal thus swapping the indices of refraction and reversing

---

[1] On some occasions the pump wavelength was so short that the required temperature for degeneracy was below the dew point and condensation on the crystal prevented operation until the laser wavelength and temperature were raised.

the relative propagation delay. Pairs produced at the center of the PPKTP crystal travel through 5 mm of PPKTP and 5 mm of reversed KTP and so have nearly zero birefringent delay. Pairs that travel through more PPKTP will have the idler (horizontal polarization) photons ahead of the signal, and pairs that travel through less PPKTP will have the signal (vertical polarization) photons ahead of the idler. The amount of delay between the signal and idler photons ranges from -1.77 ps to 1.77 ps. The amount of birefringent delay does not vary significantly over the range of output frequencies produced by SPDC.

An iris was installed in the collinear output path to limit the collection to near forward direction. The center of the iris could be easily aligned by maximizing the coincidence detection rate. It could be opened and closed to optimize the trade off between a higher rate of pairs and the rejection of off-axis emission.

The output was then sent through an interference filter (IF) to remove unwanted off-degeneracy signal and idler photons, as well as block stray pump and fluorescence photons. For data collection the 1-nm bandwidth and 80% transmission IF was used, while the 3-nm bandwidth IF was used during setup and alignment. The IF could be tuned by tilting it from normal incidence, which moved the center of the passband to shorter wavelengths. It could be tuned to the degenerate wavelength by maximizing the coincidence detection rate. Considering the exactly phase-matched output of Eq. (2.58), the 1-nm IF selects output within 14 mrad of the x-axis (or 0.8 .

3.2 Degenerate Cone

When the interference filter is rotated away from degeneracy to a higher angle of incidence the IF passes higher frequency light. These higher frequencies are produced off-axis in the vertically-polarized signal light. Thus, the brightest transmission through the IF will be in the shape of a cone around the forward direction. This was used to illuminate a ring on a Princeton Instruments camera (which used a back-thinned sili-

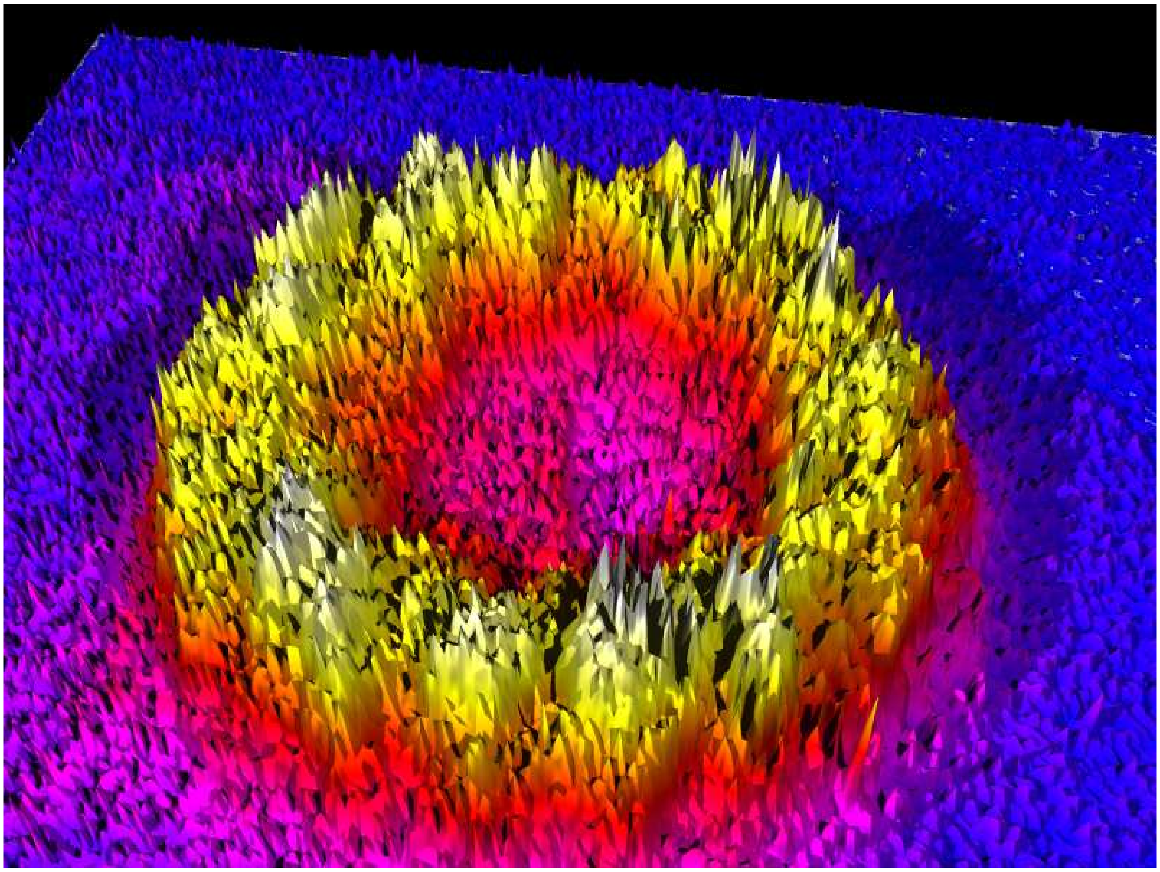

Figure 3-1: POVRay rendering of data from CCD image of the vertically polarized light, showing a ring formed by incoming cone of photons. Height and false color indicate intensity at each pixel.

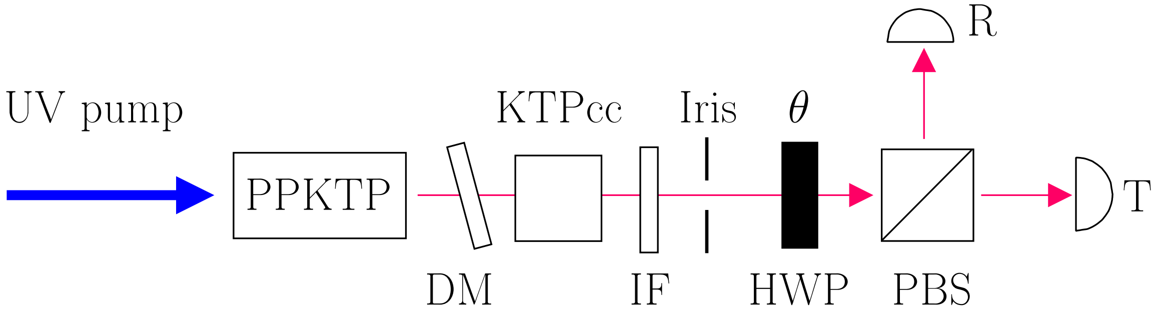

Figure 3-2: Layout for the interference dip experiment using a dichroic mirror (DM), interference filter (IF), half-wave plate (HWP), polarizing beam splitter (PBS), and two single-photon detectors (T and R). Not shown are prisms between the PBS and the two detectors.

con CCD to get ∼80% quantum efficiency near 800 nm). The UV pump was diverted with a prism. The image was processed and rendered in 3D in Fig. 3-1.

As described in section 2.3.2, it is possible to produce such a cone of nearly any size and to be degenerate. Then the entangled output pairs will be traveling along opposite edges of the cone, so a 50-50 beam splitter with its 50% loss will not be needed to separate the pair. This has been observed by Marco Fiorentino in [23].

3.3 Interference Dip

To perform the interference measurement modeled in section 2.4, the setup in Fig. 3-2 was used. A half-wave plate (HWP) at 795 nm and a polarizing beam splitter (PBS) were used to separate the output into transmitted and reflected paths. Commercial EG&G single-photon silicon avalanche detectors were used to collect the transmitted and reflected light, labeled A and B respectively.

With the HWP angle at 0°, its fast and slow axes were aligned to the signal and idler polarizations and did no polarization rotation. The π radian phase delay from the fast and slow axes was inconsequential compared to the birefringent delay. With this setting each photon pair was separated at the PBS and the maximum coincidence rate (pair generation rate) was measured. When the HWP angle was set at 22.5° it rotated the signal and idler polarization from vertical and horizontal to ±45°. Without entanglement, these polarizations would independently separate at the PBS with 50-50 probability and reducing the coincidence rate by half.

The single-photon detectors have an approximately 50% quantum efficiency at 795 nm. The active area of the detectors was about 150 µm, so the collected light was focused down with 50 mm focal length AR-coated doublet lenses (30 mm diameter, not shown on figure). They produce TTL-level logical pulses about 35 ns long with 350 picosecond jitter, and have a total dead time of roughly 50 ns. The mean time between events was typically longer than 5 µs and so the dead time effects were ignored. The intrinsic dark rate of events was about 100 Hz.

3.3.1 Coincidence Measurements

The coincidence event pulses were created by combining the output of two detectors with fast AND logic using an ORTEC model CO4020 logic unit. The detector events pulses and the coincidence event pulses were recorded by a computer using a National Instruments PCI-6602 counter/timer board. These rates are be denoted by N_T, N_R, and N_C for transmitted singles, reflected singles, and coincidences. This equipment defines a coincidences count event as at least one event in each channel within the time window of the pulse overlap. Given a pulse on one detector this time window on the other detector for coincidence identification is about 70 ns long and is called the bin time (t_B). This leads to an "accidental" contribution to the raw, uncorrected N_C rate. This can be corrected under assumptions that dead time can be ignored and that the events follow a Poisson distribution of arrival times. Define the corrected rate of "true" coincidences N_{C0} as

$$N_{C0} \equiv N_T + N_R + \frac{\log(N_C t_B + \exp(-N_T t_B) + \exp(-N_R t_B) - 1)}{t_B}, \qquad (3.1)$$

and also use this to propagate errors to N_{C0}. For short bin times, $N_{T,R,C} \ll 1/t_B$, this can be expanded to obtain

$$N_{C0} \equiv N_C - (N_T N_R)t_B + (N_T + N_R - N_C/2)N_C t_B + ..., \tag{3.2}$$

which is seen to be the raw coincidence rate minus the accidental coincidence rate plus a correction to account for events where a true and an accidental coincidence occur together. The theoretical calculations of the coincidence rate usually use the simpler form $\langle N_T N_R \rangle$ which takes the product of the number of coincidences in each channel within the time window. This theoretical model differs from Eq. (3.2) in that it is exactly

$$\tilde{N}_{C0} \equiv \tilde{N}_C - (\tilde{N}_T \tilde{N}_R)t_B, \tag{3.3}$$

with no other corrections or higher order terms. So it is a good approximation when the last term in Eq. (3.2) is small compared to N_{C0}. Looking at the experimental results reported in Table 3.1, this term is a 3-4% correction when the iris is open and 0.3-0.4% correction when the iris is small. This is large enough to be significant, so the full expression in Eq. (3.1) is used. The dead-time correction, which is 0.1% for the small iris count rate of 20,000 Hz, is ignored. This methodology of correction was tested by using a high time-resolution start-stop histogram obtained with a Picoquant TimeHarp 200 (which in described in more detail in chapter 5).

The coincidence rate in the 0° basis was continuously measured as the iris size was varied, as shown in Fig. 3-3. A second measurement in the 45° basis as the iris was varied allowed the visibility versus average singles rate to be computed. This is also shown in Fig. 3-3. At high visibility the interference dip results in very low coincidence rates with a high relative Poisson shot noise, so the spread of visibility is wider at the high visibility end of the data.

With the iris open and the HWP at 0°, the conditional coincidence rate of 19.2%

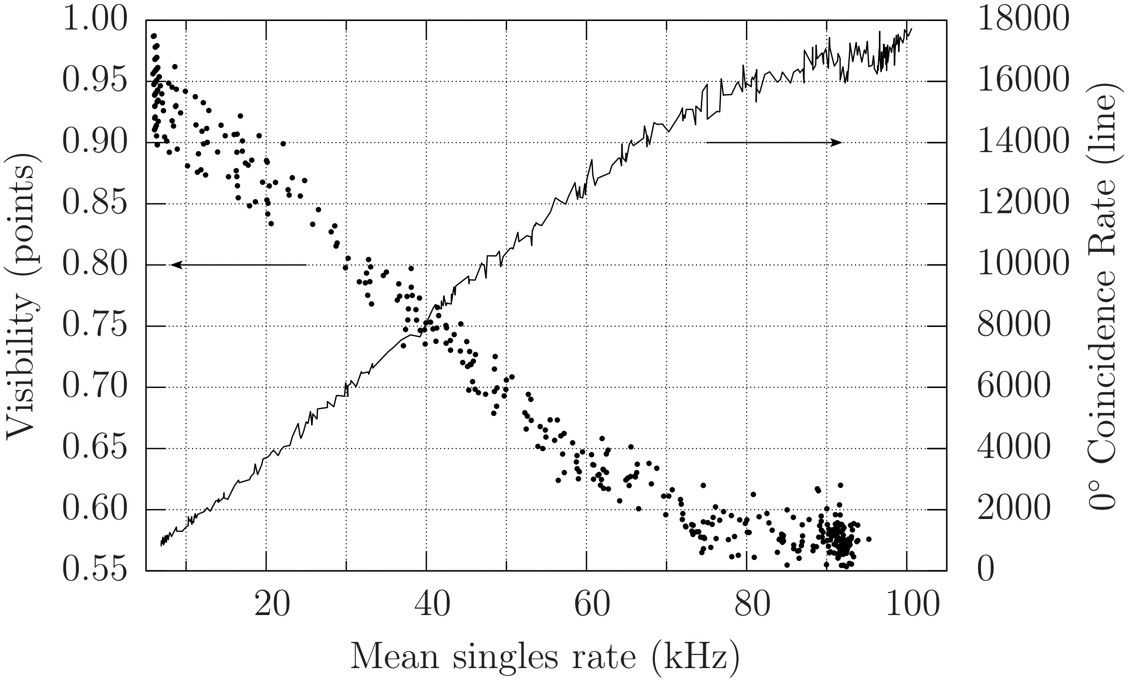

Figure 3-3: Plot showing the visibility as the collection iris is opened. The average of the single-photon detection rate is along the horizontal axis. For 0° basis analysis the coincidence rate (line, right axis scale) increases with the singles rate as the iris is opened. The visibility of the 45° basis versus the 0° basis decreases as the iris is opened (dots, left axis scale).

iris	2θ	N_T	N_R	N_C	N_{C0}	cond%
open	0°	268,767 ± 67	214,023 ± 60	48,520 ± 28	46,094 ± 29	19.2%
open	45°	239,244 ± 63	206,352 ± 59	14,766 ± 16	11,811 ± 16	5.3%
open	90°	241,127 ± 63	236,631 ± 63	48,248 ± 28	45,829 ± 29	19.2%
small	0°	20,651 ± 19	17,784 ± 17	2,540 ± 7	2,522 ± 7	13.2%
small	45°	18,909 ± 18	16,645 ± 17	66.7 ± 1.1	45.5 ± 1.1	0.26%
small	90°	20,049 ± 18	18,077 ± 17	2,539 ± 7	2,521 ± 7	13.2%

Table 3.1: Each row is from a single measurement interval of 60 seconds. All data was taken using a 1 nm IF. Rates are all in hertz, with errors computed using $\sqrt{rate/60}$ to estimate the Poisson noise. The duration of the coincidence window, t_B, was calibrated to be 67.92 ns. 2θ is the rotation of the linear-polarization done by the half-wave plate. The rates of counts at the transmitted and reflected detectors are given in columns N_T and N_R, respectively. The rate of uncorrected coincidences is given the column labeled N_C, with the corrected rate in column N_{C0}. The mean conditional probability of detection is computed with $N_{C0}/\sqrt{N_T N_R}$. The main feature of note is the ratio of the N_{C0} at 45° to either the 0° or 90° rate.

in Table 3.1 implies a generation rate in the crystal of over a million pairs per second. This assumes N_T and N_R come only from pairs, but there was also a small contribution from IR fluorescence caused by the UV laser passing through optics and coatings, estimated at ∼1000 Hz/mW of pump, and dark count rate of 100 to 200 Hz. The visibility v is calculated from the N_{C0} of the 0° (max) and 45° (min) measurements:

$$\mathrm{v} \equiv \frac{max - min}{max + min}. \tag{3.4}$$

With the iris open the corrected coincidence rate dipped from 48,000 to 12,000, which was significantly lower than an unentangled dip of 48,000 to 24,000. The visibility with the iris open was 60.8% and with the iris closed to a small aperture the visibility was 96.4% (the visibility of an unentangled source is 33.3%). This variation can be understood from the model in section 2.4. Opening the iris collected more output so the singles' rates went up as did the number of collected pairs (the line in Fig. 3-3. But these additional collected pairs had a larger transverse $\boldsymbol{q}$ parameter (i.e. larger $d\theta$). This made the signal and idler spectrum shift so they were increasingly distinguishable (Eq. (2.58)). Thus the larger aperture collected additional pairs which were less polarization-entangled and exhibit less of a dip (Eq. (2.90)). The visibility of the observed dip was the average over all the collected pairs, and this fell as the amount of collect pairs was increased (points in Fig. 3-3).

If one were to describe the best visibility with a model that consisted of a mixture of perfectly-entangled and unentangled pairs then $(max - 2min)/max = 96.3\%$ of the pairs would be fully entangled and $2min/max = 3.7\%$ would be unentangled. Using an even smaller 200-µm-diameter aperture, which collected angles up to ∼1 mrad off axis, the visibility improved to 97.7%.

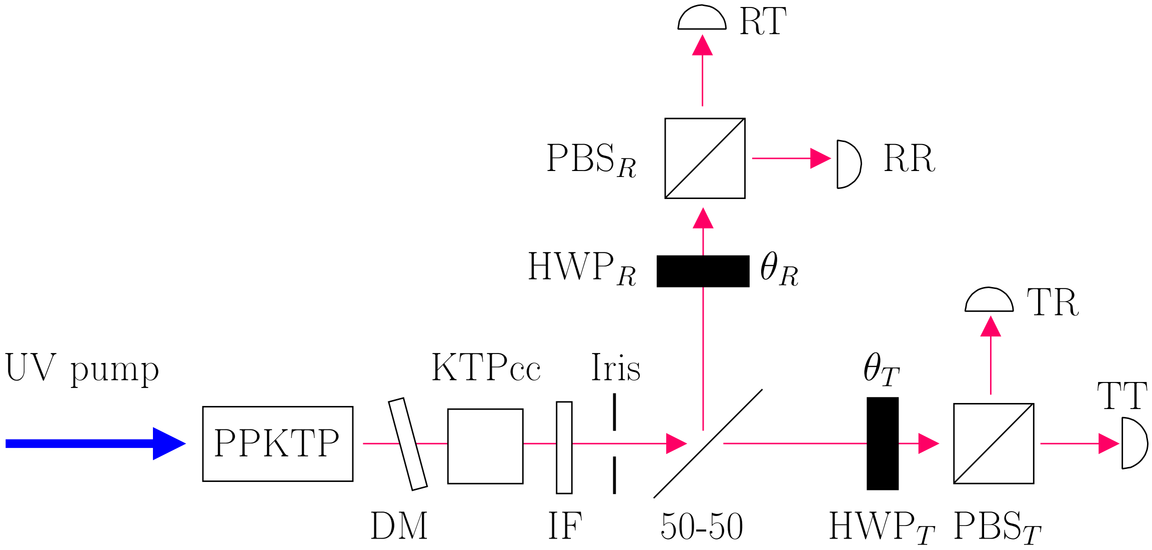

Figure 3-4: Layout for the CHSH experiment using a dichroic mirror (DM), 50-50 beam splitter, interference filter (IF), half-wave plates (HWP), polarizing beam splitters (PBS), and four single-photon detectors (TR,TR,RT,RT).

3.4 Entanglement

The above dip result is highly indicative of polarization entanglement, but it is possible to make a stronger set of observations. The most common measure is the violation of the "CHSH" form of Bell's inequality [24]. The ideal, loophole-free form of such an experiment would demonstrate quantum entanglement and rule out the combination of light-speed causality and local hidden variables. The detection efficiency required for a loophole-free observation is higher than the detectors in use here, so this experiment assumes quantum mechanics instead of trying to prove it.

The setup that was used is shown in Fig. 3-4, where the 50-50 beam splitter is located after the iris and before the HWP and PBS analyzers. The detectors are labeled TT,TR,RT, and RR as in Sec. 2.5. The four singles rates and three coincidence rates were measured. (The 8$^{\text{th}}$ channel of the counter/times board was used to generate the internal clock signal). The coincidence rate between the TT and TR detectors was monitored, much like the N_C rate used to measure the interference dip in the previous section. The other two coincidence rates that were measured

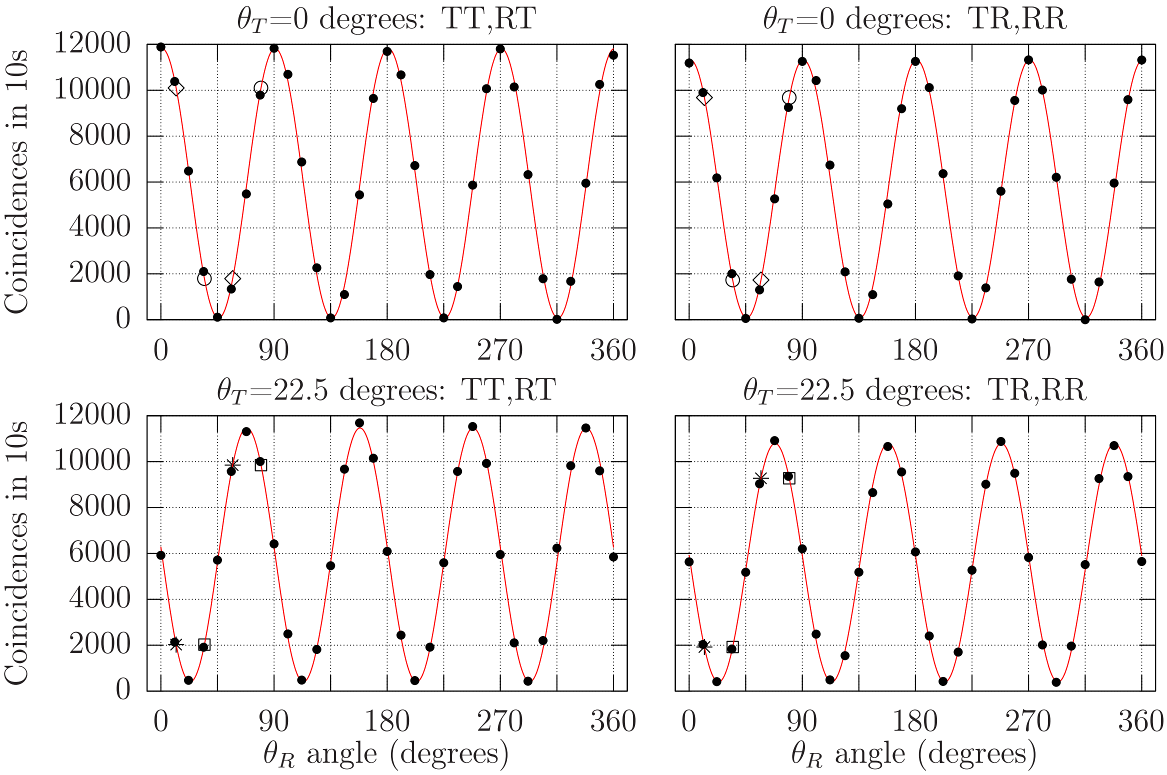

Figure 3-5: Data (solid circles) and fits for the entanglement experiment's corrected coincidences. The 16 markers on the fits (4 each of 4 kinds) are the values used to compute the CHSH inequality.

were $C_{TT,RT}$ and $C_{TR,RR}$. One half-wave plate, HWP$_T$, was set to either $\theta_T = 0°$ or $\theta_T = 22.5°$. The second half-wave plate, HWP$_R$ was set to a series of 32 angles spaced roughly 11.25° apart for each setting of θ_T. The $C_{TT,RT}$ and $C_{TR,RR}$ coincidence rates for these two series of angles were measured for 10 seconds per setting. The resulting data was fit to sinusoidal functions as shown in Fig. 3-5.

Since only 2 of the four coincidence rates between the two analyzers were measured, the others ($C_{TT,RR}$ and $C_{TR,RT}$) were derived from the fits with θ_R set forward by 45°:

$$C_{TT,RR}(\theta_T, \phi_R) = C_{TT,RT}(\theta_T, \phi_R + 45°) \tag{3.5}$$

$$C_{TR,RT}(\theta_T, \phi_R) = C_{TR,RR}(\theta_T, \phi_R + 45°) \tag{3.6}$$

marker	θ_T	ϕ_R	$E(\theta_T, \phi_R)$
diamond	0°	11.25°	-0.6978
circle	0°	33.75°	0.6978
asterisk	22.5°	11.25°	0.6579
square	22.5°	33.75°	0.6579

Table 3.2: The four E values used in the CHSH inequality (see Eq. (2.94)) and the marker symbols in Fig. 3-5 used to compute each value. Combining the four E value gives $S = 2.711 \pm 0.010$.

There is a small offset determined by the fit between the angle θ_R of the scale of the holder for HWP$_R$ and the angle ϕ_R of the half-wave plate's axes. The two values ϕ_R and ϕ'_R for optimal violation of the CHSH inequality are 11.25° and 33.75°. The four coincidence rates that are combined to form a single normalized $E(\theta_T, \phi_R)$ value (defined in Eq. (2.94)) are given the same kind of marker on Fig. 3-5, and the four E values and their markers are listed in table 3.2. The ideal E magnitude would be $\sqrt{2}/2 = 0.707107$, leading to $S = 2\sqrt{2} = 2.82843$. In this experiment S was 2.711 ± 0.010. This violates the classical limit of S less than 2 by over 70 times the standard deviation. Measuring $C_{TT,RT}$ and $C_{TR,RR}$ for only the 8 settings of the half-wave plates needed would take 80 seconds of acquisition time.

Chapter 4

Cavity Theory

> The only things known to go faster than ordinary light is monarchy, according to the philosopher Ly Tin Weedle. He reasoned like this: you can't have more than one king, and tradition demands that there is no gap between kings, so when a king dies the succession must therefore pass to the heir instantaneously. Presumably, he said, there must be some elementary particles – kingons, or possibly queons – that do this job, but of course succession sometimes fails if, in mid-flight, they strike an anti-particle, or republicon. His ambitious plans to use his discovery to send messages, involving the careful torturing of a small king in order to modulate the signal, were never fully expanded because, at that point, the bar closed.
>
> **Terry Pratchett**, *Mort*

4.1 Introduction

The downconversion process is strongly influenced by the presence of cavity mirrors that reflect the output wavelengths [28]. This modifies the input field for the internal crystal from a vacuum state to one that includes feedback. In the models discussed

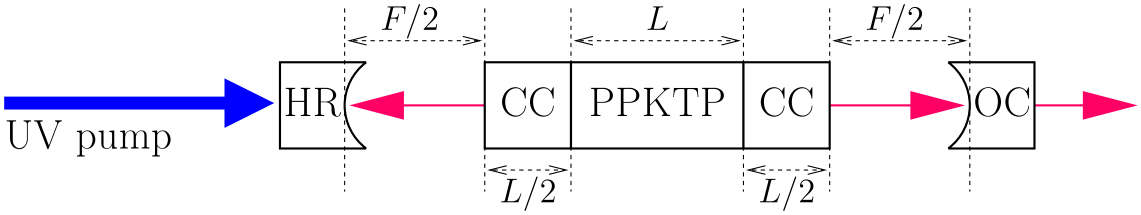

Figure 4-1: Layout for the model of the single-ended cavity. The pump is transmitted by all the components. Distances are defined in terms of the PPKTP length L and the total free space length F. The KTP compensating crystals (CC) are half the length of the PPKTP crystal.

the pump will always be taken as transmitted perfectly by the cavity mirrors, and therefore considered single-pass. Presented first is the simplest approximation to the cavity derivation: considering only a single mode for the signal and for the idler. This will provide an analytical solution which can be easily pictured in the time domain. Also, a modified form that includes a quarter-wave plate will be presented which has some interesting properties. These generalize and extend previous work by J.H. Shapiro (Refs. [7, 29]). Next, there will be a new and more complicated derivation based on Laguerre-Gaussian modes for the pump, signal, and idler. This will ultimately require numerical integration, but will provide more complete predictions. The previous derivations were only for the specific limit of forward single-mode plane waves, with the cavity at double-resonance, with the signal and idler at degeneracy, and for equal signal and idler free-spectral ranges in the cavity. These restrictions are relaxed or removed in the new derivations presented here.

4.2 Simple Model

This derivation includes only a single mode for the signal and single mode for the idler. This will turn out to be a reasonable approximation for resonant cavity modes. The optical layout is shown in Fig. 4-1. The field operators of Eq. (A.27) are used to describe the fields at the input and output of each optical element. Ultimately the cavity output signal and idler are solved for in terms of the signal and idler

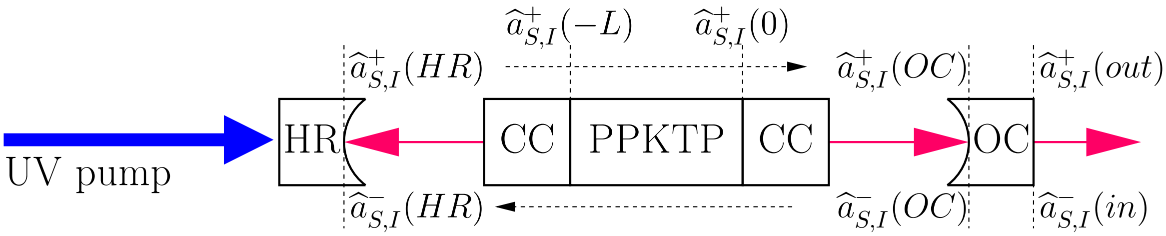

Figure 4-2: Identical to Fig. 4-1, but annotated to show the locations and directions for which the field operators are defined.

cavity inputs, which are taken to be vacuum. This is a single ended cavity where the signal and idler can enter and exit only through the output coupler. The frequency difference between successive resonances is the free spectral range (FSR) which for an empty linear cavity of length ℓ is $2\ell/c$.[1] The finesse is defined by the ratio of the FSR and the full width at half maximum (relative to minimum) (FWHM) of the resonant peaks:

$$\text{finesse} \equiv \frac{\text{FSR}}{\text{FWHM}} = \frac{\pi}{\arccos\left(\frac{2\sqrt{R_1 R_2}}{1+R_1 R_2}\right)} \approx \frac{\pi\sqrt[4]{R}}{1-\sqrt{R}}, \tag{4.1}$$

where the arccos form is given for a two-ended linear cavity with power-reflection coefficients R_1 and R_2. The approximate form is for a single-ended linear cavity where $R_1 = R$ and $R_2 = 1$. This is an excellent approximation (less than 1% error) for R greater than 65%. The low R limit requiring the arccos form comes up in practice since the pump is slightly reflected by the two cavity mirrors by enough to create a ripple in the pump transmission. We note that internal losses can be easily lumped in an effective R or R_2.

Fields that travel to the right in Fig. 4-1 are the $\widehat{a}^{+}_{S,I}(\omega, x)$ operators and to the left are the $\widehat{a}^{-}_{S,I}(\omega, x)$ operators, where ω is the (angular) frequency of the field above the degenerate frequency ω_0 with x as the position label. The pump travels to the right in a single pass. Outside the cavity, to the right of the output coupler (OC), are the

---

[1] This effective ℓ is slightly modified by the Gouy phase of the Gaussian beam, on the order of a wavelength of the light. This shift will usually be ignored, except when comparing different higher-order Gaussian modes.

cavity input fields $\widehat{a}_S^-(\omega; in)$ and $\widehat{a}_I^-(-\omega; in)$ and cavity output fields $\widehat{a}_S^+(\omega; out)$ and $\widehat{a}_I^+(-\omega; out)$. The fields inside the cavity, on the left side of the OC, are $\widehat{a}_S^+(\omega; OC)$, $\widehat{a}_S^-(\omega; OS)$, $\widehat{a}_I^+(-\omega; OC)$, and $\widehat{a}_I^-(-\omega; OC)$. The fields at the high reflector (HR) are $\widehat{a}_S^+(\omega; HR)$, $\widehat{a}_S^-(\omega; HR)$, $\widehat{a}_I^+(-\omega; HR)$, and $\widehat{a}_I^-(-\omega; HR)$. There are three crystals in the model cavity: a length L PPKTP crystal with a length $L/2$ KTP compensating crystal on each side. This arrangement means the pair will be timing compensated when it leaves the cavity. The field state entering the PPKTP is $\widehat{a}_S^+(\omega; -L)$ and $\widehat{a}_I^+(-\omega; -L)$. The field state leaving the PPKTP is $\widehat{a}_S^+(\omega; 0)$ and $\widehat{a}_I^+(-\omega; 0)$. There is length $F/2$ free space between each mirror and the crystals. The output coupler has transmission and reflection parameters $T_{S,I}$ and $R_{S,I} = 1 - T_{S,I}$. Therefore, the model equations are given by the external output coupler boundary condition:

$$\widehat{a}_S^+(\omega; out) = i\sqrt{T_S}\widehat{a}_S^+(\omega; OC) - \sqrt{R_S}\widehat{a}_S^-(\omega; in) \tag{4.2a}$$

$$\widehat{a}_I^+(-\omega; out) = i\sqrt{T_I}\widehat{a}_I^+(-\omega; OC) - \sqrt{R_I}\widehat{a}_I^-(-\omega; in) \tag{4.2b}$$

and the internal equations

$$\widehat{a}_S^-(\omega; OC) = -\sqrt{R_S}\widehat{a}_S^+(\omega; OC) + i\sqrt{T_S}\widehat{a}_S^-(\omega; in) \tag{4.2c}$$

$$\widehat{a}_I^-(-\omega; OC) = -\sqrt{R_I}\widehat{a}_I^+(-\omega; OC) + i\sqrt{T_I}\widehat{a}_I^-(-\omega; in) \tag{4.2d}$$

$$\widehat{a}_S^-(\omega; HR) = \widehat{a}_S^-(\omega; OC)\exp(i(\omega_0 + \omega)(F + Ln_S(\omega) + Ln_I(\omega))/c) \tag{4.2e}$$

$$\widehat{a}_I^-(-\omega; HR) = \widehat{a}_I^-(-\omega; OC)\exp(i(\omega_0 - \omega)(F + Ln_S(-\omega) + Ln_I(-\omega))/c) \tag{4.2f}$$

$$\widehat{a}_S^+(\omega; HR) = -\widehat{a}_S^-(\omega; HR) \tag{4.2g}$$

$$\widehat{a}_I^+(-\omega; HR) = -\widehat{a}_I^-(-\omega; HR) \tag{4.2h}$$

$$\widehat{a}_S^+(\omega; -L) = \widehat{a}_S^+(\omega; HR)\exp(i(\omega_0 + \omega)(F/2 + Ln_I(\omega)/2)/c) \tag{4.2i}$$

$$\widehat{a}_I^+(-\omega; -L) = \widehat{a}_I^+(-\omega; HR)\exp(i(\omega_0 - \omega)(F/2 + Ln_S(-\omega)/2)/c) \tag{4.2j}$$

$$\begin{aligned}\widehat{a}_S^+(\omega; 0) = {} & \big(\widehat{a}_S^+(\omega; -L)\mu(\omega)\exp(i(\omega_0 + \omega)Ln_S(\omega)/c)\big) + \\ & \big(\widehat{a}_I^{+\dagger}(-\omega; -L)\nu(\omega)\exp(-i(\omega_0 - \omega)Ln_I(-\omega)/c)\big)\end{aligned} \tag{4.2k}$$

$$\begin{aligned}\widehat{a}_I^+(-\omega; 0) = {} & \big(\widehat{a}_I^+(-\omega; -L)\mu(\omega)\exp(i(\omega_0 - \omega)Ln_I(-\omega)/c)\big) + \\ & \big(\widehat{a}_S^{+\dagger}(\omega; -L)\nu(\omega)\exp(-i(\omega_0 + \omega)Ln_S(\omega)/c)\big)\end{aligned} \tag{4.2l}$$

$$\widehat{a}_S^+(\omega; OC) = \widehat{a}_S^+(\omega; 0)\exp(i(\omega_0 + \omega)(F/2 + Ln_I(\omega)/2)/c) \tag{4.2m}$$

$$\widehat{a}_I^+(-\omega; OC) = \widehat{a}_I^+(-\omega; 0)\exp(i(\omega_0 + \omega)(F/2 + Ln_S(-\omega)/2)/c) \tag{4.2n}$$

where the conjugated forms of the internal equations are also included. The PPKTP is placed from $-L$ to 0 so that the previous result in Eq. (2.52) can be used, but the coordinates are arbitrary. The nonlinear coefficients μ and ν themselves are almost those of Eq. (2.49a), except for $\mathcal{K}$. The amplitude of $\mathcal{K}$ in ν is not as large in the single-pass case since this cavity process ignores all the other spatial modes of the output. Calculating the reduced $\mathcal{K}$ will be undertaken in section 4.4.

The solution depends on two slightly different times: since the cavity is not empty there are two ways to define the round-trip time. The free spectral range for a given wavelength, e.g. 795 nm, depends on the phase velocity and determines the FSR related time $\mathfrak{L}$:

$$\mathfrak{L} = 2(F + L(n_S(0) + n_I(0)))/c = 808.25 \text{ ps.} \tag{4.3}$$

$$\tag{4.4}$$

However, just as with the single-pass case, the group velocity determines the propagation delay of the signal and idler photons. Define the group velocity dependent $\mathfrak{B}$, to first order, as:

$$\mathfrak{b} = 2L(n'_S(0) + n'_I(0))\omega_0/c = 7.82 \text{ ps} \tag{4.5}$$

$$\mathfrak{B} = \mathfrak{L} + \mathfrak{b} = 816.07 \text{ ps.} \tag{4.6}$$

In the above, L is taken to be 10 mm, and F is 85.1 mm. The dispersive shift $\mathfrak{b}$ is then a few times the correlation box width of 3.5 ps. It is the $\mathfrak{B}$ time, not the $\mathfrak{L}$, that will determine the arrival time delay on the histogram. The solution below shows that if the signal photon stays in the cavity for n round-trips more than the idler photon, then the difference in arrival times $t_S - t_I$ for this pair will be increased by $n\mathfrak{B}$.

To model a singly-resonant cavity, set one of the R_I or R_S to zero. For the doubly-resonant cavity the $R_{S,I}$ and $T_{S,I}$ are set to be identical and equal to R, with $T \equiv 1 - R$. The solution for the doubly-resonant cavity output in terms of the cavity input is then:

$$1 = |\mu|^2 - |\nu|^2. \tag{4.7a}$$

$$d(\omega) = 1 - \sqrt{R}e^{i(\mathfrak{L}\omega_0+\mathfrak{B}\omega)}\mu(\omega) - \sqrt{R}e^{-i(\mathfrak{L}\omega_0-\mathfrak{B}\omega)}\mu^*(\omega) + Re^{2i\mathfrak{B}\omega} \tag{4.7b}$$

$$\alpha(\omega) = \mu(\omega)e^{i(\mathfrak{L}\omega_0+\mathfrak{B}\omega)} - \sqrt{R} - \sqrt{R}e^{2i\mathfrak{B}\omega} + R\mu^*(\omega)e^{-i(\mathfrak{L}\omega_0-\mathfrak{B}\omega)} \tag{4.7c}$$

$$\beta(\omega) = -e^{i(\mathfrak{B}\omega-\phi)}T\nu(\omega) \tag{4.7d}$$

$$\phi = \left(\left(\frac{\mathfrak{L}}{2} + \frac{L}{2c}(n_S(0) + n_I(0))\right)\omega_0\right) \tag{4.7e}$$

$$\widehat{a}_S^+(\omega; out) = \frac{\alpha(\omega)}{d(\omega)}\widehat{a}_S^-(\omega; in) + \frac{\beta(\omega)}{d(\omega)}\widehat{a}_I^{-\dagger}(-\omega; in) \tag{4.7f}$$

$$\widehat{a}_I^+(-\omega; out) = \frac{\alpha(-\omega)}{d^*(\omega)}\widehat{a}_I^-(-\omega; in) + \frac{\beta(-\omega)}{d^*(\omega)}\widehat{a}_S^{-\dagger}(\omega; in). \tag{4.7g}$$

The $d(\omega)$, $\alpha(\omega)$, $\beta(\omega)$, and ϕ expressions are shorthand. The downconversion amplitude factor $\nu(\omega)$ is part of $\beta(\omega)$, where it is multiplied by a phase and by the transmission amplitude $\sqrt{T}$ for both the signal and idler. The phase shift of ϕ is frequency independent and does not affect any of the measurements. The $\alpha(\omega)/d(\omega)$ is very close to unity amplitude and, while important for preserving commutation brackets, does not tell us much. The denominator $d(\omega)$ will be interesting, since its amplitude creates the periodic resonance structure.

The effect of the cavity can be removed by taking the limit of $R \to 0$ and $T \to 1$; this limit makes $d(\omega) \to 1$,$\alpha(\omega) \to \mu(\omega)\exp(i...)$, and $\beta(\omega) \to \nu(\omega)\exp(i...)$. This reduces the solution to the single pass case, up to phases which come from the now odd choice of input field location and presence of the high reflector.

In the low-power limit $\mu(\omega)$ is approximately one and the expressions for $d(\omega)$ and

$\alpha(\omega)$ can be factored. This allows the solution to be simplified to:

$$d(\omega) = \left(1 - \sqrt{R} e^{i(\mathfrak{L}\omega_0 + \mathfrak{B}\omega)}\right)\left(1 - \sqrt{R} e^{-i(\mathfrak{L}\omega_0 - \mathfrak{B}\omega)}\right), \tag{4.8a}$$

$$\alpha(\omega) = \left(1 - \sqrt{R} e^{-i(\mathfrak{L}\omega_0 + \mathfrak{B}\omega)}\right)\left(1 - \sqrt{R} e^{-i(\mathfrak{L}\omega_0 - \mathfrak{B}\omega)}\right) e^{i(\mathfrak{L}\omega_0 + \mathfrak{B}\omega)}, \tag{4.8b}$$

$$\beta(\omega) = -i\mathcal{K}LT e^{i(\mathfrak{B}\omega - \phi)} \operatorname{sinc}\left(\frac{\Delta k' \omega L}{2c}\right). \tag{4.8c}$$

In this low-power limit the $\alpha(\omega)/d(\omega)$ term is of unit magnitude. The form of $\beta(\omega)$ is, up to a phase, just T times the single-pass result. The doubly-resonant cavity effects come from the denominator $d(\omega)$ which is the product of two factors: a signal frequency and an idler frequency factor. A singly-resonant cavity would have only one of these factors in $d(\omega)$.

When the pump frequency, $2\omega_0$, and the cavity round-trip phase, $\mathfrak{L}$, are at a double resonance the output simplifies further:

$$\omega_0 \to \frac{2\pi m}{\mathfrak{L}}, \text{ where } m \in \mathbb{N} \tag{4.9}$$

$$d(\omega) = \left(1 - \sqrt{R} e^{i\mathfrak{B}\omega}\right)^2 \tag{4.10}$$

$$\alpha(\omega) = \left(1 - \sqrt{R} e^{-i\mathfrak{B}\omega}\right)\left(1 - \sqrt{R} e^{i\mathfrak{B}\omega}\right) e^{i\mathfrak{B}\omega} \tag{4.11}$$

$$\beta(\omega) = -i\mathcal{K}LT e^{i(\mathfrak{B}\omega - \phi)} \operatorname{sinc}\left(\frac{\Delta k' \omega L}{2c}\right). \tag{4.12}$$

$$\left|\frac{1}{d(\omega))}\right| = \frac{1}{1 + R - 2\sqrt{R}\cos(\mathfrak{B}\omega)} \tag{4.13}$$

This double resonance occurs when ω_0 is a multiple of the FSR 1.237 GHz, which is half the FSR at degeneracy. When $(\mathfrak{B}\omega)$ is 0 mod (2π) the $\beta(\omega)/d(\omega)$ output amplitude has a resonant peak, which occurs when ω is a multiple of 1.225 GHz. Hence the output spectra for signal and idler have a peak roughly every FSR (modified by the group velocity, not phase).

Therefore, one would expect a doubly-resonant degenerate peak where $\omega = 0$ once every FSR of the cavity, i.e. one such peak should occur if the OC is moved

$\lambda_0/2 = 397.5$ nm. However, it is observed that two such peaks occur at half this spacing. This is because there is a second "odd" resonance condition in between the degenerate resonances:

$$\omega_0 \rightarrow \frac{\pi m}{\mathfrak{L}}, \text{ where } m \text{ is odd} \tag{4.14}$$

$$d(\omega) = \left(1 + \sqrt{R}e^{i\mathfrak{B}\omega}\right)^2 \tag{4.15}$$

$$\alpha(\omega) = -\left(1 + \sqrt{R}e^{-i\mathfrak{B}\omega}\right)\left(1 + \sqrt{R}e^{i\mathfrak{B}\omega}\right)e^{i\mathfrak{B}\omega} \tag{4.16}$$

$$\beta(\omega) = -i\mathcal{K}LTe^{i(\mathfrak{B}\omega-\phi)}\operatorname{sinc}\left(\frac{\Delta k'\omega L}{2c}\right). \tag{4.17}$$

$$\left|\frac{1}{d(\omega))}\right| = \frac{1}{1 + R + 2\sqrt{R}\cos(\mathfrak{B}\omega)} \tag{4.18}$$

The output spectrum now has a peak when $(\mathfrak{B}\omega)$ is π mod (2π). Hence there is almost no output at the degenerate wavelength, but otherwise the downconversion rate experiences a double resonant enhancement. The output rate when neither of these resonant conditions is close to being satisfied is suppressed.

4.2.1 Ultrabright peaks

The difference between the "even" degenerate and "odd" non-degenerate resonance and the off-resonant condition is depicted in Figures 4-3, 4-4, and 4-5.

In the singly-resonant case, in which only one polarization is reflected by the cavity, the denominator d has only the factor for the resonated polarization, and the T in β is $\sqrt{T}$. This $d(\omega)$ reshapes the phase-matched output spectrum into a series of peaks keeping the integrated total output rate unchanged (This is similar to the flat regime of Fig. 4-12) . The spectral reshaping increases the brightness near the peak frequencies by a factor proportional to the finesse. The brightness per unit hertz near a resonant peak in the frequency spectrum is proportional to the finesse of the cavity.

In the doubly-resonant case above, the two terms in the denominator narrow the the output slightly more and increase the integrated total output by a factor of the

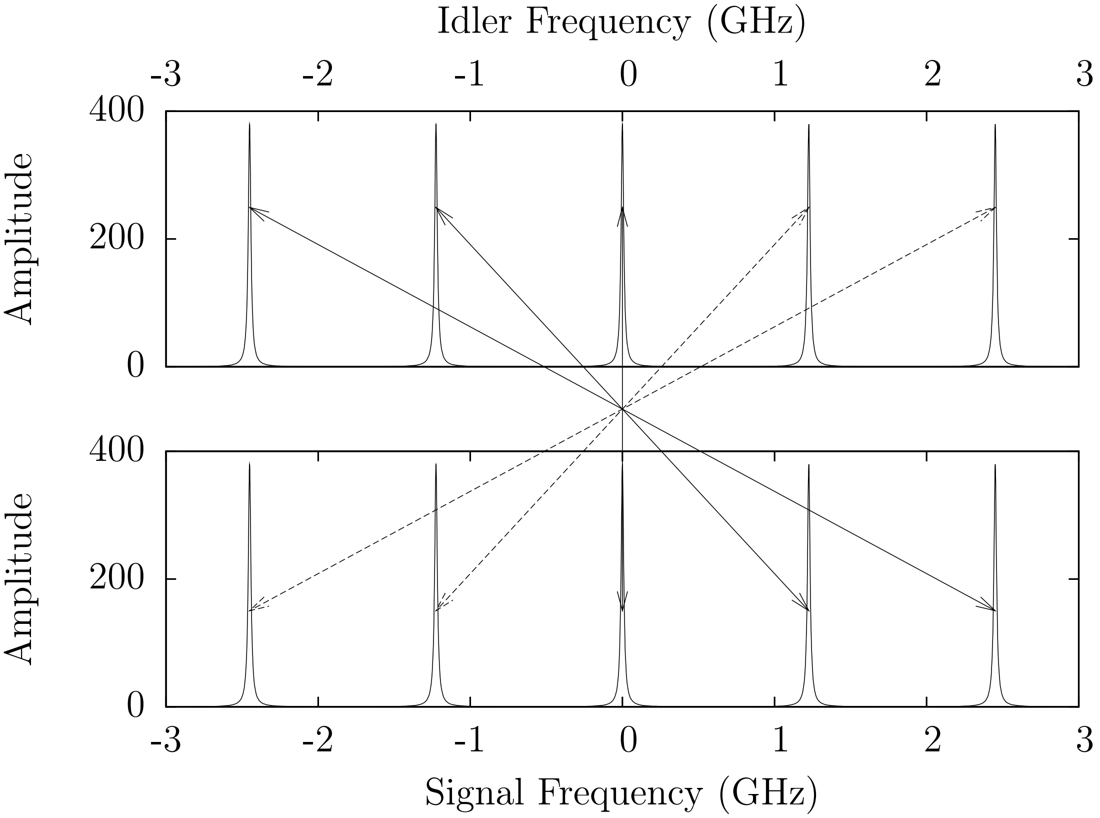

Figure 4-3: Spectral condition for degenerate double resonance. Each curve is for probing the cavity near degeneracy (0 GHz) with the signal or idler polarization (they have equal FSR). The arrows connect signal/idler pairs, showing that the signal resonances are matched with the idler resonances. The downconversion is proportional to the product of the signal and idler amplitudes.

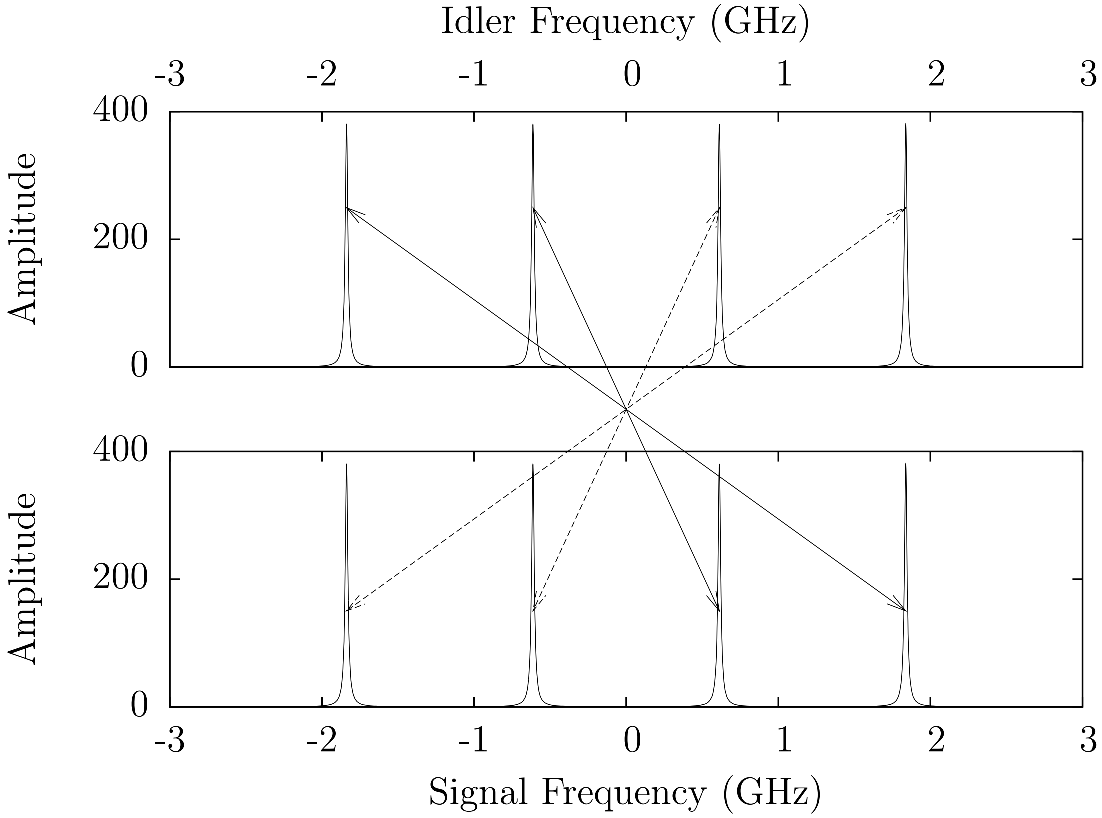

Figure 4-4: Similar to Fig. 4-3, but a different cavity length has offset the degenerate (0 GHz) point. This shows the non-degenerate double resonance. Each signal and idler peak is paired with a peak on the other spectrum as shown by the arrows.

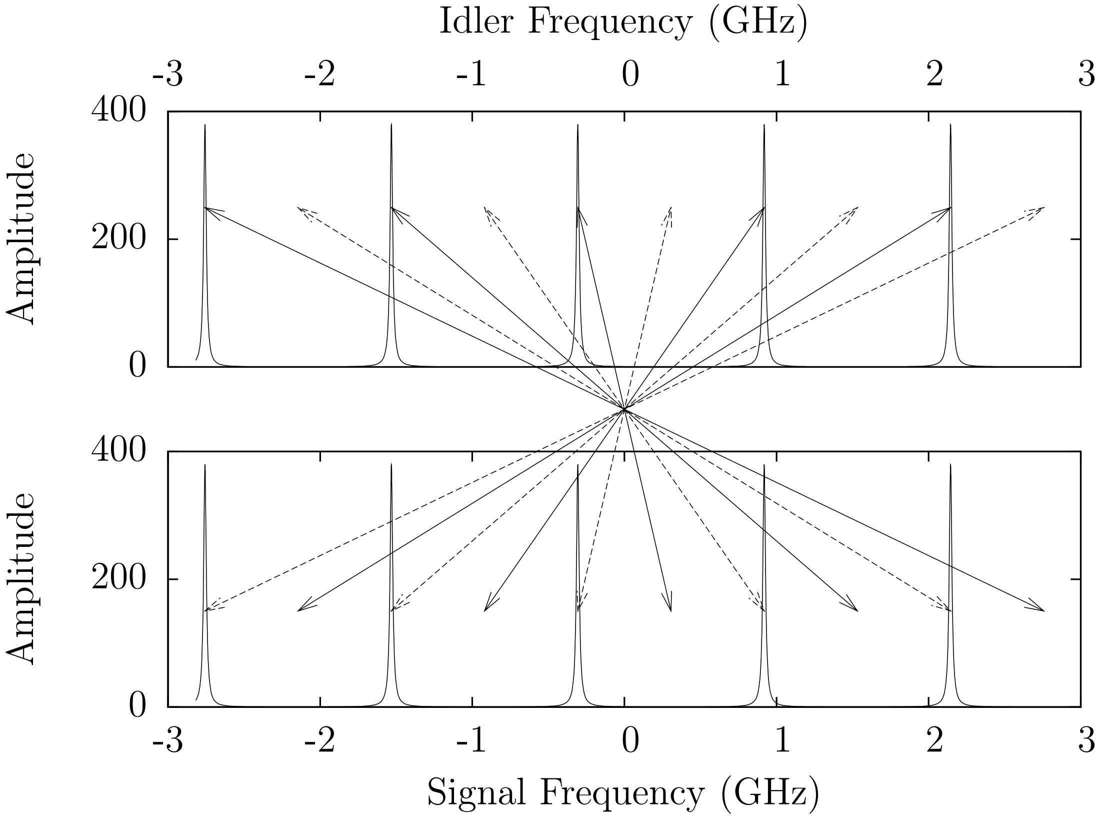

Figure 4-5: Similar to Fig. 4-3 and Fig. 4-4, but with a cavity length between those two conditions. Thus this shows a non-resonant condition where the signal and idler peaks are not paired with each other. This suppresses the downconversion rate.

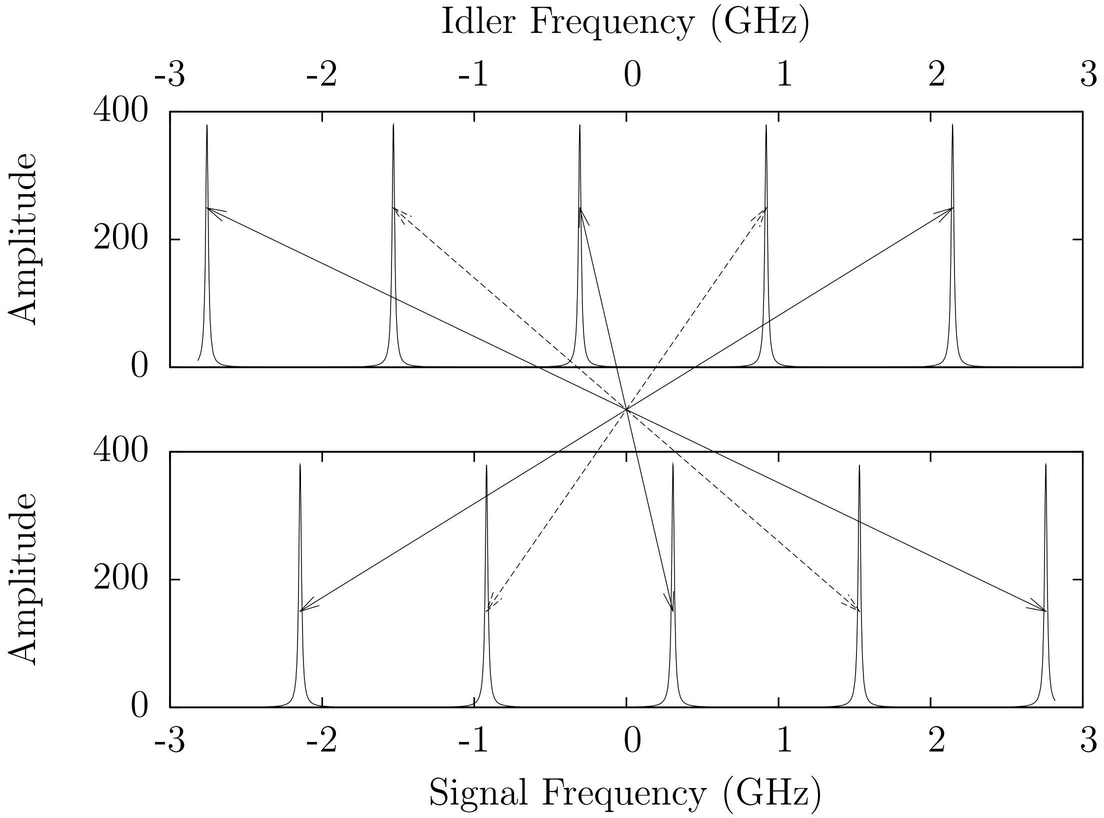

Figure 4-6: Spectral conditions for unequal signal and idler FSR but with the cavity length at double resonance. The signal and idler peaks are matched as shown by the arrows, but the signal peaks and idler peaks do not line up at the same frequencies. This allows the polarization to be deduced from the frequency.

finesse divided by π. As the finesse increases, the rate of downconversion increases and the bandwidth decreases so that the brightness per unit hertz near the peak frequencies increase as the square of the finesse. Away from the peaks the doubly-resonant cavity suppresses the output by as much as $(1+\sqrt{R})^4/T^2$ which is two to three orders of magnitude.

4.2.2 Histogram

The ideal start-stop histogram is determined from the phase-sensitive correlation function, which is the Fourier transform:

$$K_{SI}^{(p)}(t_S - t_I) = \int \frac{d\omega}{2\pi} \exp(-i\omega(t_S - t_I)) \left(\frac{\alpha(\omega)\beta(-\omega)}{d(\omega)d^*(\omega)} \right) \tag{4.19}$$

Now the $(1 - \sqrt{R}\exp(...))$ factors in α cancel factors in dd^* leaving

$$\frac{1}{1-\sqrt{R}\exp(i\mathfrak{B}\omega)} \frac{1}{1-\sqrt{R}\exp(-i\mathfrak{B}\omega)} = \sum_{j_S=0}^{\infty} \left(\sqrt{R}\exp(i\mathfrak{B}\omega) \right)^{j_S} \sum_{j_I=0}^{\infty} \left(\sqrt{R}\exp(-i\mathfrak{B}\omega) \right)^{j_I}. \tag{4.20}$$

The denominator is seen to be a sum of the contribution from j_S round trips inside the cavity for the signal and the j_I round trips for the idler. Each term in the expanded sums is reduced in amplitude and phase shifted. Therefore, the Fourier integral transforms the phase shift into a translation in $\delta t = t_s - t_I$. Thus the 3.5 ps wide box function is translated by the number of round-trip delays that the signal and idler photons take in the cavity, with the idler contributing the opposite sign. As the photons may exit after a different number of round trips, the ideal start-stop histogram will resemble Fig. 4-7. In a perfectly resonant system, each of the spikes in the figure is a 3.5 ps wide box which is the accumulation of a different number of co-round trips.

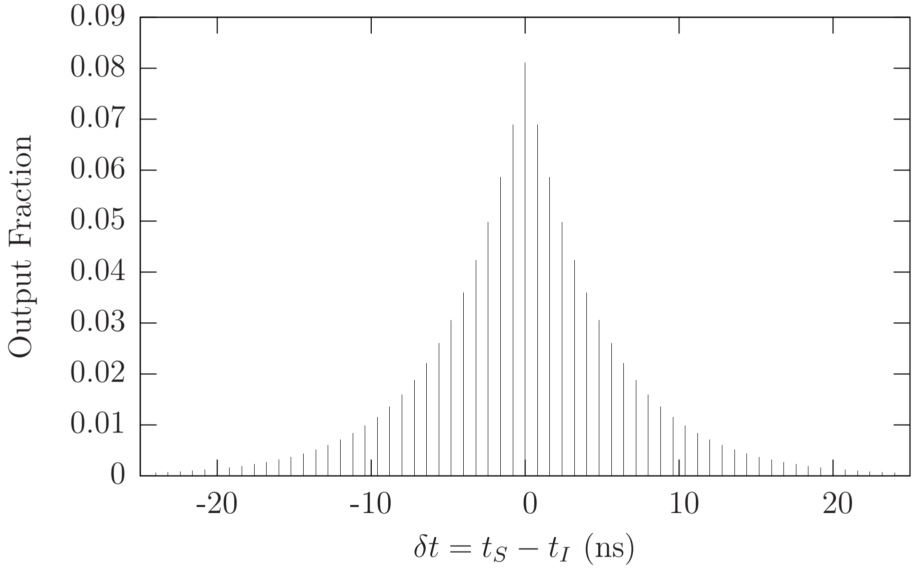

Figure 4-7: Model output histogram for R of 85% and round-trip time of 0.8 ns. The difference in the number of round trips taken by the signal and idler make the distinct peaks. The height for each spike is normalized so they sum to one.

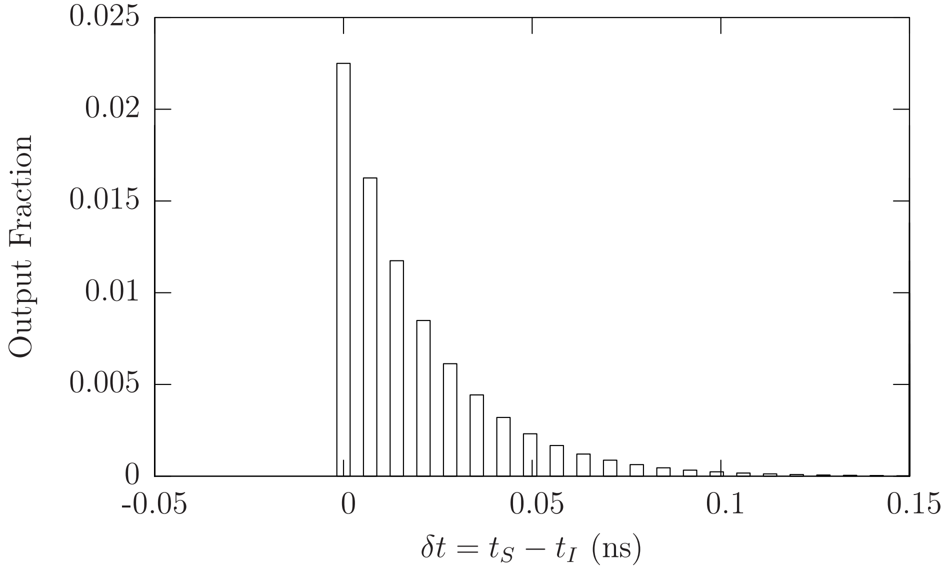

Figure 4-8: This is a zoomed view of Fig. 4-7 near $\delta t = 0$. This is for a model without any compensating crystals in the cavity (only one outside the OC). The reflectivity of the OC is 85% and round-trip time is 0.8 ns. Only contributions from signal and idler that take the same number of round trips are visible. Height is normalized to fraction of total output contained in each box.

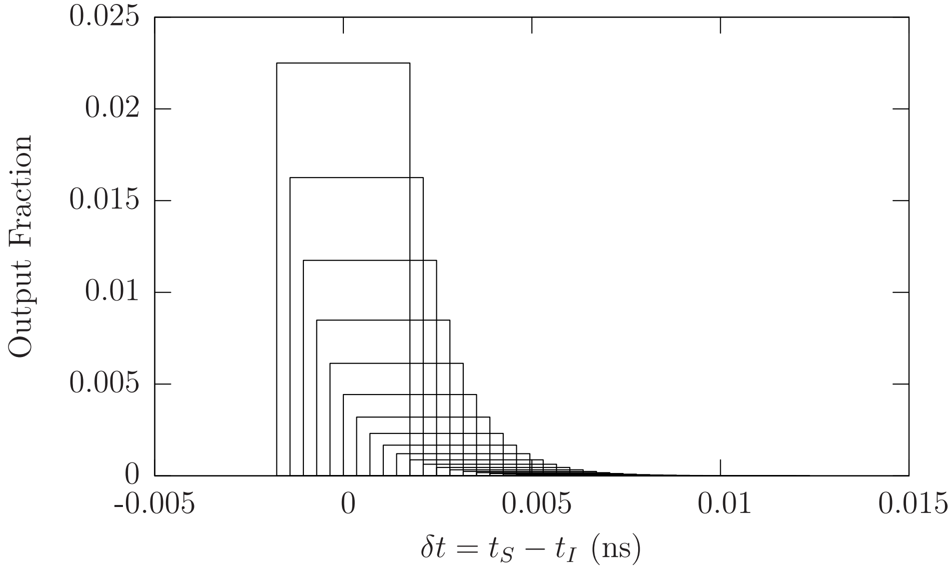

Figure 4-9: Like Fig. 4-8 but the compensating crystal is 95% of the length of the PPKTP (50% near OC, 45% near HR). The co-round-trip shift of 0.353 ps moves the box by 10% of its width. How the boxes interfere depends on the cavity length.

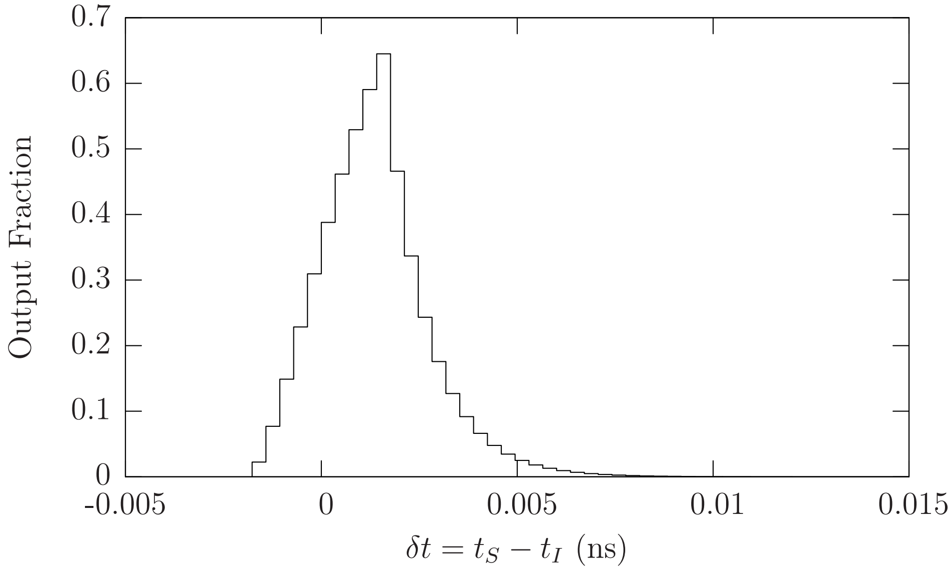

Figure 4-10: This is the same as Fig. 4-9 at a cavity length giving resonance with constructive interference of the boxes.

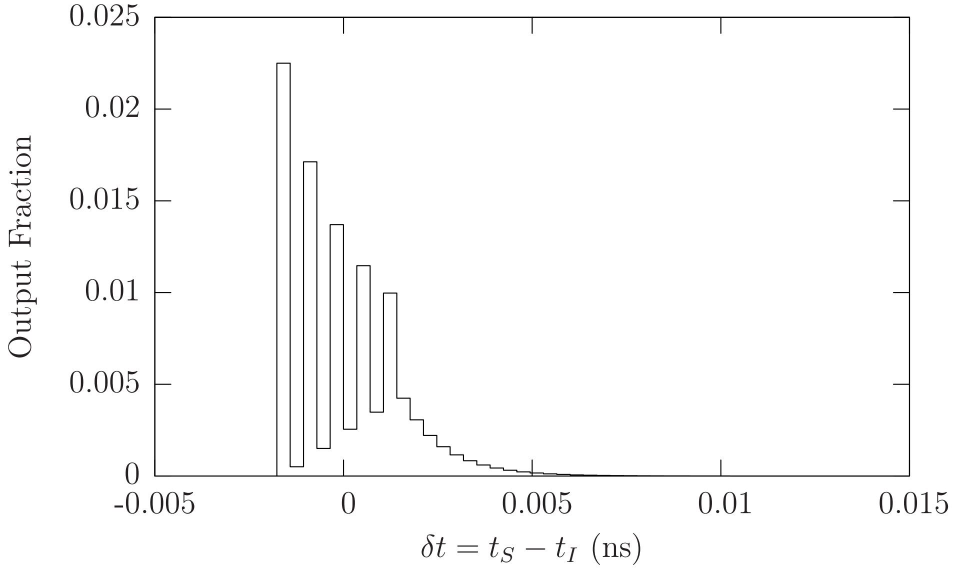

Figure 4-11: This is the same as Fig. 4-9 at a cavity length giving maximum destructive interference of the boxes.

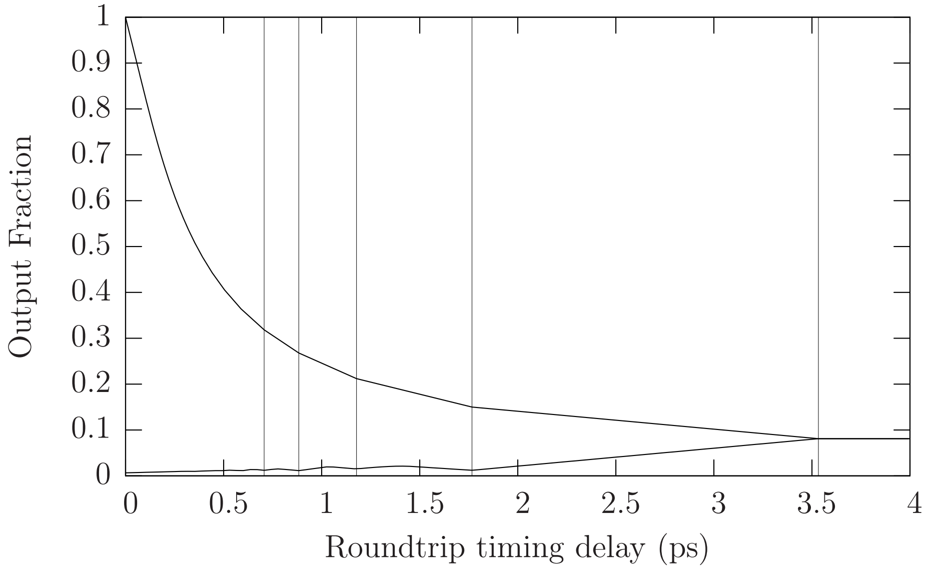

Figure 4-12: This is a plot of the downconversion rate versus the round-trip birefringent shift. Upper curve is for contructive resonant cavity length; lower curve is for most destructive cavity length. Vertical lines at 3.5/1,2,3,4,5 are provided to indicate where additional boxes (Fig. 4-9) overlap. These transitions make the maximum effectively piecewise linear. Past 3.5 ps the system acts similarly to a singly-resonant cavity and the output rate is independent of cavity length.

4.2.3 Slightly Unequal FSR

Experimentally, arranging the birefringence in the cavity to cancel to zero to give equal FSR is a special case, and the more generic situation must also be modeled. The constructive and destructive overlap of "box" terms will be described in the time domain by reference to the correlation function $\langle \widehat{a}_S^+(\boldsymbol{q}_1, t_S; 0)\widehat{a}_I^+(\boldsymbol{q}_2, t_I; 0)\rangle$ which determines the ideal start-stop histogram of photon detection times. The imbalance in FSR is modeled by the compensating crystal near HR being short by σ, but keeping the same free space length F. This crystal length error will cause the boxes to slowly shift in δt as the number of co-round trips increases as sketched in Fig. 4-9. Getting the phase of each of those boxes requires solving the modified model. The phase difference between the boxes comes from the more complex $d(\omega)$ denominator. Define an average round-trip phase $\mathfrak{L}_0$ and individual round-trip phases $\mathfrak{L}_S$ and $\mathfrak{L}_I$, and the new group velocity dependent $\mathfrak{B}_S$ and $\mathfrak{B}_I$ which have average $\mathfrak{B}_0$:

$$\mathfrak{d} \equiv (n_S(0) - n_I(0))/c \tag{4.21}$$

$$\mathfrak{L}_0 = 2\left(F + L\left(1 - \frac{\sigma}{2L}\right)(n_S(0) + n_I(0))\right) \tag{4.22}$$

$$\mathfrak{L}_S = \mathfrak{L}_0 + \mathfrak{d}\sigma \tag{4.23}$$

$$\mathfrak{L}_I = \mathfrak{L}_0 - \mathfrak{d}\sigma \tag{4.24}$$

$$\mathfrak{B}_0 = \mathfrak{L}_0 + \mathfrak{b}\left(1 - \frac{\sigma}{2L}\right) \tag{4.25}$$

$$\mathfrak{B}_S = \mathfrak{B}_0 - \left(\frac{\Delta k'}{c}\right)\sigma \tag{4.26}$$

$$\mathfrak{B}_I = \mathfrak{B}_0 + \left(\frac{\Delta k'}{c}\right)\sigma \tag{4.27}$$

$$d(\omega) \equiv \left(1 - \sqrt{R}\exp(i(\mathfrak{L}_S\omega_0 + \mathfrak{B}_S\omega)\right)\left(1 - \sqrt{R}\exp(-i(\mathfrak{L}_I\omega_0 - \mathfrak{B}_I\omega))\right) \tag{4.28}$$

The $\mathfrak{d}$ term is shorthand for the birefringence at degeneracy and σ is the length by which the KTP CC near the HR is shorter than $L/2$.

In terms of round-trip counts j_S and j_I, the $\alpha/(dd^*)$ factor now produces the correlation function:

$$\begin{aligned} K_{SI}^{(p)}(t_S - t_I) = \int \frac{d\omega}{2\pi} \exp\Big(-i\omega(t_S - t_I)\Big)\beta(-\omega)\times \\ \sum_{j_S=0}^{\infty}\sum_{j_I=0}^{\infty}(\sqrt{R})^{j_S+j_I}\exp\Big(i(j_S+j_I)\mathfrak{L}_0\omega_0\Big)\exp\Big(i(j_S-j_I)\mathfrak{d}\sigma\omega_0\Big) \\ \exp\Big(-i(j_S+j_I)\Delta k'\sigma\omega/c\Big)\exp\Big(i(j_S-j_I)\mathfrak{B}_0\omega\Big) \end{aligned} \tag{4.29}$$

This is the key equation for understanding the output state of the cavity. The Fourier transform of $\beta(-\omega)$ alone is the transform of sinc to box as seen in Eq. (2.69). The double sum can be seen as a sum over the possible histories of the signal and idler photons inside the cavity. The amplitude $\sqrt{R}$ factor damps the amplitude so only a finite number of terms need to be used for computations. This finite truncation means each round-trip peak in Fig. 4-7 can be computed separately for our experiment. The sum can be transformed into the number of round trips the signal and idler take together, $u = \min(j_S, j_I)$, and the difference in round trips, $v = j_s - j_I$:

$$\begin{aligned} \sum_{v=-\infty}^{\infty}\sum_{u=0}^{\infty}(\sqrt{R})^{2u+|v|}\exp\Big(i(2u+|v|)\mathfrak{L}_0\omega_0\Big)\exp\Big(i(v)\mathfrak{d}\sigma\omega_0\Big) \\ \exp\Big(-i(2u+|v|)\Delta k'\sigma\omega/c\Big)\exp\Big(i(v)\mathfrak{B}_0\omega\Big) \end{aligned} \tag{4.30}$$

There are four exp(...) factors in the sum:

- The first factor is similar to the resonance term for the equal FSR case, and has both even and odd resonances where $\exp(-i\mathfrak{L}_0\omega_0)$ equals ± 1, respectively. The sum over overlapping boxes, $\sum_u$, has a factor of 2 so the $(\pm 1)^{2u}$ is always 1. The peaks for different v will alternate in sign for the odd resonances, $(-1)^v$, or all be the same phase for even resonances.

- The second factor, which contains $\mathfrak{d}\sigma$, contributes to each box a phase proportional to $(j_S - j_I)$, the difference in number of round-trips. This is also special when $\exp(i\mathfrak{d}\sigma\omega_0)$ is ± 1, as this is when the signal and idler cavity resonance peaks are at (nearly) the same positions. This phase is irrelevant if the histogram is taken between the signal and idler in the 0° basis. But other measurements in Chapter 5 are sensitive to this phase.

- The third factor creates a small translation of the boxes for small σ. This delay from the $2u$ part of this factor is what shifts the boxes as illustrated in Fig. 4-9. This may be ignored as long as the delay is small compared to 3.5 ps, which means that $\sigma \ll L/2$. (This means the system is operating near the peak shown in Fig. 4-12.) In the case where $\sigma = L/2$ this delay is 3.5 ps, the width of the boxes, so that they no longer overlap.

- The fourth factor produces the big $\sim$816 ps translation for each additional round trip, creating the peak spacing seen in Fig. 4-7.

If there are no compensating crystals ($\sigma = L$) then each co-round trip will shift the histogram by twice the delay from the PPKTP, as seen in the zoomed view in Fig. 4-8. If the compensating crystals are almost the correct length then these boxes will overlap, as seen in Fig. 4-9. Once overlapping, the amplitudes must be combined before taking the square of the absolute value, which allows for interference effects. Constructive interference of many of these boxes is what gives the significant brightness enhancement at double resonance.

This constructive interference condition can also be seen in the alignment of the signal and idler cavity spectra. The double-resonance conditions for the pump, $2\omega_0$, and cavity round-trip phase, $\mathfrak{L}_0$, is the same as for the equal FSR case and still produces two resonances per FSR. However, with unequal FSR the spectra for signal and idler no longer have to produce degenerate output at either of the two resonances. Instead they will resemble Fig. 4-6, where the cavity resonances for the signal and idler polarizations near degeneracy are no longer at the same frequencies. Nevertheless, when the cavity length is such that the $\omega = 0$ degenerate frequency is midway between signal and idler peaks, as shown by the arrows in the figure, there is a double-resonant enhancement of downconversion. This corresponds to the aforementioned $\exp(i\mathfrak{L}_0\omega_0)$ being ±1, so this also has even and odd conditions. The offset between the signal and idler resonance peaks is controlled by the value of $\mathfrak{d}\sigma\omega_0$. When σ is zero the equal FSR case is recovered. When $\exp(i\mathfrak{d}\sigma\omega_0)$ factor is ±1 the signal and idler resonance spectra are lined up again, almost like the equal FSR case. This occurs when σ is a multiple of 4.5 µm Ṫhe re-aligned spectra have unequal FSR, but the signal and idler FSRs will differ by 4 kHz times $\sigma/(4.5\,\mu\text{m})$ which is extremely small compared to their magnitude of 1.24 GHz.

The opposite case is destructive interference. The worst-case cavity length for the output, as shown in Fig. 4-11, is at or sometimes slightly displaced from being exactly between the constructive peaks. The maximum and minimum downconversion rates versus cavity delay are shown in Fig. 4-12. For delays equivalent to removing one of the two compensating crystals or longer it is a non-resonant flat line that extends out the right side of the plot. The function for the maximum output is piecewise linear with each section representing a different number of overlapping boxes. This description is true insofar as the small co-round-trip birefringent delay does not accumulate to equal the round-trip time. But in our case the amplitude is damped by hundreds of cavity lifetimes long before accumulating enough delay so we can ignore this possibility.

4.2.4 Interference dips and entanglement

The rate of coincidences measured after PBS in a 0° basis of horizontal and vertical polarization is proportional to:

$$\int dt \left| K_{SI}^{(p)}(\delta t) \right|^2 . \tag{4.31}$$

The rate of coincidences measured by a PBS in a ±45 olarization basis is proportional to:

$$\int dt \left| K_{SI}^{(p)}(\delta t) - K_{SI}^{(p)}(-\delta t) \right|^2 /4. \tag{4.32}$$

Thus if the boxes in the $K^{(p)}$ function are even in $\delta t = t_S - t_I$, then the 45° basis will measure zero coincidences. This is the same condition as in the single-pass case, and it indicates polarization entanglement although it does not prove it as the CHSH measurement does.

The $\exp(i(v)\mathfrak{d}\sigma\omega_0)$ factor affects the early and late boxes with opposite phase shifts. This affects the interference dip because that depends on whether v is positive or negative, which can make $K^{(p)}(\delta t)$ no longer an even function.

The center group, where $j_S = j_I$ so $v = 0$, always cancels to zero exactly; however, the other boxes away from the center will not be fully entangled and will not cancel to zero. They will revive, however, when the phase shift $\mathfrak{d}\sigma\omega_0$ is a multiple of π, which can be achieved in this setup if σ is a multiple of 4.50 µm. This condition is when the boxes will come back into phase with their partners with opposite δt and the interference dip will return. The amplitude of the odd differential round-trip peaks may be negative, but this makes no difference to the probability. The revival is not exactly perfect since the co-round trips now shift the boxes slightly, but $\sigma = 4.50$ µm creates a 3.2 fs shift of the co-round-trip boxes which is much less than their 3.5 ps width and thus can be ignored.

The phase shifting by $m\pi$ to $(m+1)\pi$ can be observed in the frequency domain. Consider the cavity transmission of the probe laser at ω_0 in both polarizations (e.g. at +45°). As the length of the cavity is changed by moving the OC on a piezo-electric stack, the transmitted light goes through a free spectral range and a peak is seen. For ideal double-resonance both polarizations have the same free spectral range and their peaks occur at the same position in the sweep of the piezo voltage. As the length error σ in one of the compensating crystals is simulated by altering its temperature, the positions of the signal and idler transmission peaks move dramatically and at different rates due to the birefringence. Initially overlapping peaks will separate and after changing the effective crystal length by ~4.5 µm, one peak will have lapped the other and they will again appear to resonate at the same piezo voltage. This corresponds to squeezing an extra half-wavelength more of one polarization into the cavity. The signal and idler FSRs will have changed by ~30 kHz, and the difference of the two FSRs will be altered by ~4 kHz.

In practice the length of the crystal is not tunable. Instead, the temperature is used to control the birefringence of the compensating crystals. Changing the L-length compensating crystal temperature by ~4.5°C is equivalent to changing σ by 4.5 µm. Thus the temperature must be stabilized to better than (4.5°C/$finesse$) to keep the signal and idler peaks overlapped and maintain polarization entanglement. This provides one practical limit on how large a finesse can be selected.

The width of these dips relative to their revival period is the cavity finesse divided by two. In between the dips the ratio is close to the classical 50% value. All of these measurements are equivalent to measuring the center of a HOM dip, since the relative timing is not being varied. The presence of the dip indicates that the signal and idler are partially or totally indistinguishable, which requires the signal and idler spectrum peaks to be at the same frequencies as discussed in the previous section. Technically only the equal-FSR case has a perfect dip; the recurring dips have slightly offset the co-round-trip boxes so the overhang is not an even function and this prevents perfect cancellation. This misalignment is very small, however, because the shift caused by $\sigma = 4.5$ µm is small relative to the box width; only after ~1100 revivals will the dip have disappeared.

The interference dip does not depend on double resonance. In particular the $\exp(i(2u + |v|)\mathfrak{L}_0\omega_0)$ factor does not break the even symmetry required for $K_{SI}^{(p)}(\delta t)$ to produce entanglement. The constructive or destructive overlap is not related to producing polarization entanglement, but only to the rate at which pairs are produced. This separation of doubly-resonant operation and polarization-entangled operation means that the cavity length does not affect entanglement quality. Conversely, tuning the length (or temperature) of the compensating crystals does not affect the quality of either the even or odd double resonance.

However, the ratio of total coincidence rates is found by integrating over all possible measurement intervals. If a fine-resolution histogram of arrival time differences is measured, then a more complex model is needed. Let v be $j_S - j_I$ to number each round-trip box. Now consider just the boxes at $\pm v$. The 0° and 45° rate contributed by these boxes, ignoring the slight position shift, is proportional to

$$\text{rate}(v,0) = \left|\exp(i(v)\mathfrak{d}\sigma\omega_0)\right|^2 + \left|\exp(i(-v)\mathfrak{d}\sigma\omega_0)\right|^2 \tag{4.33}$$

$$\text{rate}(v,0) = 2 \tag{4.34}$$

$$\begin{aligned}\frac{\text{rate}(v,45)}{\text{rate}(v,0)} &= \left|\exp(i(-v)\mathfrak{d}\sigma\omega_0) - \exp(i(v)\mathfrak{d}\sigma\omega_0)\right|^2/8 \\ &\quad + \left|\exp(i(v)\mathfrak{d}\sigma\omega_0) - \exp(i(-v)\mathfrak{d}\sigma\omega_0)\right|^2/8 \qquad (4.35)\\ &= \sin(v\mathfrak{d}\sigma\omega_0)^2 \qquad (4.36)\end{aligned}$$

The ratio is thus a $\sin^2$ function that is zero at the aforementioned recurrences when $\mathfrak{d}\sigma\omega_0$ is a multiple of π. In particular, the ratio will oscillate $|v|$ times between these uniform revivals. The $v = 0$ box is always 0 as mentioned above. Also note that the $\sin^2$ ratio has a maximum of 1, so there is no dip for such a round-trip box (singlet behavior). This behavior is unique to a type-II system in the cavity, since a type-I pair will always have equal FSR.

The total over all the v-boxes for unequal FSR will average to give the appearance of the classical dip of 50%. This total dip, showing a revival after 4.5°C, is shown in Fig. 4-13.

The $K^{(p)}(\delta t)$ function as a sum of boxes made this straightforward to calculate, but what does the bi-photon state look like? For a given $|v| \neq 0$, label the early

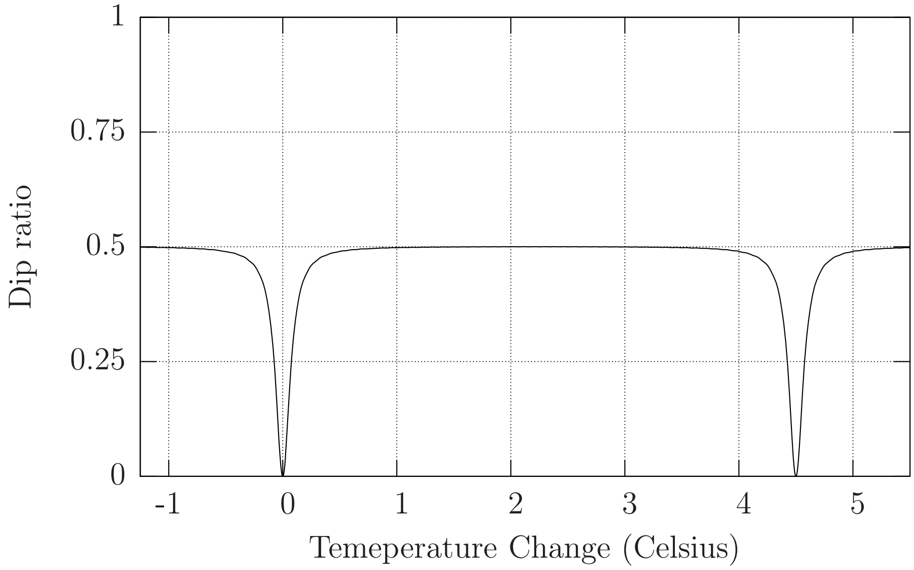

Figure 4-13: This is a plot of the interference dip, the ratio of coincidences measured at 45° to 0°, as the temperature is detuned from equal FSR to the first revival. The cavity mirror's reflection R is set to 90%.

photon as time slot 1 and the late photon as time slot 2. The ±45° polarization states will be labeled F and D, with $|H\rangle = (|F\rangle + |D\rangle)/\sqrt{2}$. Then the un-normalized state for bi-photons with $|j_S - j_I| = |v|$ is:

$$\phi = |v|\mathfrak{d}\sigma\omega_0, \tag{4.37}$$

$$|\Psi\rangle = e^{i\phi}\,|H\rangle_1 \otimes |V\rangle_2 + e^{-i\phi}\,|V\rangle_1 \otimes |H\rangle_2\,, \tag{4.38}$$

$$= (|F\rangle_1 \otimes |F\rangle_2 - |D\rangle_1 \otimes |D\rangle_2)\cos(\phi) - i\,(|F\rangle_1 \otimes |D\rangle_2 - |D\rangle_1 \otimes |F\rangle_2)\sin(\phi). \tag{4.39}$$

The coincidences after the PBS in the 45° basis come from the second term which is proportional to $\sin(v\mathfrak{d}\sigma\omega_0)^2$ as predicted by Eq. (4.35). The $v = 0$ state is always the $|H, V\rangle = |F, F\rangle - |D, D\rangle$ triplet state as in the single-pass model. For the maximal anti-dip when ϕ is $\pi/2$, the state is a singlet in the 0° and 45° bases, and indeed for any polarization basis. (This is ignoring the 1.6 fs shift of the co-round-trip boxes for $\phi = \pi/2$ compared to the 3.5 ps box width). If the $|v| = 1$ boxes are in a singlet state then so are all the odd v boxes, while the even $|v|$ boxes (including the center) are in the triplet state. This whole output state is not in a mixed state since the different $|v|$ states can be measured separately by the start-stop histogram.

4.3 Aside on using a QWP

One trick to reduce the difficulty of tuning the compensating crystals is to create a different cavity arrangement. Consider a quarter-wave plate inserted at 45° next to the high reflector. The photons will swap from signal to idler polarization when they encounter the QWP and HR. So a particular photon reflecting from the OC sees the crystals once as horizontally and once as vertically polarized before returning to the OC. This removes birefringence from additional cavity round trips. The $l/2$-length compensating crystal near the HR can be removed since it does not affect the birefringence. The $l/2$ compensating crystal near the OC does correct the timing as in the single pass case; in some arrangement it can be placed outside the cavity's OC instead of inside. The number of tuning parameters is reduced to two: making the PPKTP temperature match the pump frequency and setting the cavity length with the piezo.

The QWP-cavity has an analytical solution that is much richer than the normal cavity. It has the general form

$$\widehat{a}_S^+(\omega; out) = \alpha \widehat{a}_S^-(\omega; in) + \beta \widehat{a}_I^{-\dagger}(-\omega; in) + \alpha' \widehat{a}_I^-(\omega; in) + \beta' \widehat{a}_S^{-\dagger}(-\omega; in), \tag{4.40}$$

$$\widehat{a}_I^+(-\omega; out) = \tilde{\alpha} \widehat{a}_I^-(-\omega; in) + \tilde{\beta} \widehat{a}_S^{-\dagger}(\omega; in) + \tilde{\alpha}' \widehat{a}_S^-(-\omega; in) + \tilde{\beta}' \widehat{a}_I^{-\dagger}(\omega; in), \tag{4.41}$$

where the output operators are nonlinear mixtures of four instead of two input operators.

If one photon stays an extra odd number of round trips inside the cavity it will exit with the same polarization that its partner did. This will happen close to half the time, creating correlations in the arrival times of identically polarized photons that were not there in the original cavity. Thus several correlation functions that were zero before are now non-zero. This could be alleviated by placing a QWP on each side of the output coupler at ±45°. Then the photon would always leave the cavity+QPWs with its original polarization, and the output operator would be more like the original cavity's mixture of two input operators.

4.4 Laguerre-Gaussian Basis

The previous derivation noted that the nonlinear coefficients μ and ν depend on the spatial mode effects. By computing these effects an optimal arrangement can be found to maximize the downconversion rate. The cavity mode is largely determined by the given mirrors and a desire for a long round-trip time, which both makes the resonant peaks' bandwidth narrower and increases the round-trip delay on a histogram. For collection into a fiber, the desired output mode is a Gaussian, as is the UV pump mode. The remaining question is the waist size that the pump should have given the cavity-determined waist for the output modes. This is very similar to computing the amount the signal-pass output could be coupled through an empty-cavity filter or into a single-mode collection fiber.

Previously, the single-pass pump waist was large enough to ignore the difference between it and a plane wave. For the cavity, the optimal pump Gaussian is focused tighter than the range of validity for this approximation. With the plane-wave pump if an output photon is detected as some plane-wave $f(\boldsymbol{q}, \omega)$, it can be deduced that the partner photon is in the mode $f(-\boldsymbol{q}, -\omega)$. With a realistic Gaussian pump there is a range around $-\boldsymbol{q}$ in which the partner photon momentum can be. This mixing appears in the operator in the general form:

$$\widehat{a}_S^+(\boldsymbol{q}, \omega; out) = \alpha(\omega)\widehat{a}_S^-(\boldsymbol{q}, \omega; in) + \int d^2\boldsymbol{q}'\beta(\boldsymbol{q}', \omega)\widehat{a}_I^-(\boldsymbol{q}' - \boldsymbol{q}, -\omega; in), \tag{4.42}$$

where many idler terms contribute to one signal (and vice versa), with β having the pump beam's width in $\boldsymbol{q}$.

The continuous plane-wave momentum basis is less convenient once the pump is no longer a single plane wave, and the cavity itself creates a natural basis of resonant output modes.

The most useful basis is the discrete Laguerre-Gaussian (L-G) basis (which limits the model to the paraxial approximation). The waist position, direction, and size must be specified. The signal and idler modes are the same and will have the cavity axis and focal parameters. The classical pump has the same parameters except for waist size. The field operators in the Hamiltonian and the progression generator $\widehat{G}$ are expanded in this basis.

Each L-G mode is indexed by a radial parameter p which is a non-negative integer, and an orbital angular-momentum parameter ℓ which can be any integer. Cylindrical coordinates around the longitudinal x-axis are used, with the explicit formula for the normalized L-G modes[27]:

$$k \equiv \frac{\omega}{n(\mathbf{0},\omega)c}, \quad \text{total momentum in material} \tag{4.43}$$

$$x_R \equiv k\frac{w_0^2}{2}, \quad \text{Rayleigh range or (b-parameter/2)} \tag{4.44}$$

$$w(x) \equiv w_0\sqrt{1+\left(\frac{x}{x_R}\right)^2}, \quad \text{waist, } (1/e) \text{ amplitude radius} \tag{4.45}$$

$$r_c(x) \equiv x\left(1+\left(\frac{x_R}{x}\right)^2\right), \quad \text{radius of curvature (expanding if } r_c > 0) \tag{4.46}$$

$$LG_p^\ell(x,r,\theta) \equiv \sqrt{\frac{2(p!)}{\pi w^2(p+|\ell|)!}}\left(\frac{r\sqrt{2}}{w}\right)^{|\ell|}\mathcal{L}_P^{|\ell|}\left(\frac{2r^2}{w^2}\right) \exp\left(i\ell\theta-\frac{r^2}{w^2}+i\frac{kr^2}{2r_c}-i(2p+|\ell|+1)\arctan\left(\frac{x}{x_R}\right)+ikx\right) \tag{4.47}$$

$$LG_0^0(x,r,\theta) = \sqrt{\frac{2}{\pi w^2}}\exp\left(-\frac{r^2}{w^2}+i\frac{kr^2}{2r_c}-i\arctan\left(\frac{x}{x_R}\right)+ikx\right). \tag{4.48}$$

The arctan term provides the Gouy phase factor, which will be important for the non-Gaussian modes in the cavity. For reference:

$$\exp(-ib\arctan(a)) \equiv \left(\frac{1-ia}{\sqrt{1-a^2}}\right)^b \equiv \left(\frac{\sqrt{1-a^2}}{1+ia}\right)^b. \tag{4.49}$$

4.4.1 Perturbative Calculation

Expanding the pump, signal, and idler fields (c.f. Eqs. (A.29),(2.3)), with the foci at $x = 0$ but different waists $w_{P,S,I}$, yields:

$$E_P^+(\boldsymbol{r};t) = i\sqrt{\frac{\hbar\omega_P}{2\epsilon_0 n_P(\mathbf{0},\omega_P)c}} A_P LG_0^0(w_P;\boldsymbol{r})\frac{\exp(-i\omega_P t)}{\sqrt{2\pi}} \tag{4.50}$$

$$\widehat{E}_S^+(\boldsymbol{r};t) = \sum_{p_S=0}^{\infty}\sum_{\ell_S=-\infty}^{\infty}\int d\omega_S\, i\sqrt{\frac{\hbar\omega_S}{2\epsilon_0 n_S(\mathbf{0},\omega_S)c}}\widehat{a}_S^+(w_S;p_S,\ell_S;\omega_S)LG_{p_S}^{\ell_S}(\boldsymbol{r})\frac{\exp(-i\omega_S t)}{\sqrt{2\pi}} \tag{4.51}$$

$$\widehat{E}_I^+(\boldsymbol{r};t) = \sum_{p_I=0}^{\infty}\sum_{\ell_I=-\infty}^{\infty}\int d\omega_I\, i\sqrt{\frac{\hbar\omega_I}{2\epsilon_0 n_I(\mathbf{0},\omega_I)c}}\widehat{a}_I^+(w_I;p_I,\ell_I;\omega_I)LG_{p_I}^{\ell_I}(\boldsymbol{r})\frac{\exp(-i\omega_I t)}{\sqrt{2\pi}} \tag{4.52}$$

Expanding $\widehat{E}$ and d_{24} in H_{int} results in a sum of terms, in which only the quasi-phase matched are kept. The spatial integral of Eq. (2.2) that determines the perturbation calculation of the bi-photon has become a sum of spatially different bi-photon states. The axial indices determine the orbital angular momentum $\exp(i\ell\theta)$ and by conservation the signal and idler must have $\ell_I = -\ell_S$. This reduces the remaining sum to be over p_S, p_I, and ℓ_S, where the sign of ℓ_S does not affect the result and it will thus be abbreviated ℓ. An output signal mode with p_S and ℓ is coupled to idler modes with $\ell_I = -\ell$ and all values of p_I. Hence the output naturally separates into independent ℓ groups within which all the p_S and p_I are coupled. With the Gaussian pump the integral has cylindrical symmetry, such that the θ integral within the crystal is trivially 2π.

The interaction perturbation (c.f. Eq. (2.9)) is now a triple sum:

$$\begin{gathered}|\Psi_{\mathrm{bi}}\rangle = \sum_{p_S}\sum_{p_I}\sum_{\ell}\mathcal{C}\int d\omega\left(\int_{-L/2}^{L/2} dx\int_0^{\infty} dr\, f(\omega_P, p_S, p_I, \ell; x, r, \omega)\right) \\ \widehat{a}_S^{+\dagger}(w_S; p_S, \ell; \omega_P/2+\omega)\widehat{a}_I^{+\dagger}(w_S; p_S, \ell; \omega_P/2-\omega)\,|0\rangle\,,\end{gathered} \tag{4.53}$$

where f is

$$f(p_S, p_I, \ell; x, r, \omega) = (2\pi r)LG_0^0(w_P; x, r)LG_{p_S}^{\ell}{}^*(w_S; x, r)LG_{p_I}^{-\ell*}(w_I; x, r). \tag{4.54}$$

At a given longitudinal position x the radial integral over dr of f can be performed analytically. The remaining integral along x is too complex to be analytic but is fast to perform numerically. Mathematica™was used to compute and store the 125 r-integrals for all combinations of p_S,p_I, and ℓ from 0 to 4. These integrals, denoted $F(p_S, p_I, \ell)$, took a couple of days to evaluate[2], but leveraged the machine's patience. The integral over x and r of $f(...)$ is a function $\mathcal{F}(p_S, p_I, \ell)$ of the waists and ω. The integral over ω of $|\mathcal{F}(p_S, p_I, \ell)|^2$ is the unnormalized rate $\mathcal{R}(p_S, p_I, \ell)$ of downconversion into the (p_S, p_I, ℓ) bi-photon mode.

The effect of the Gouy phase on quasi-phase matching can be understood with an approximation. If the crystal were moved far from the foci of the modes then the arctan functions would be constant phase shifts and could be factored out of the integrals and ignored. If the crystal is at the focus and is small compared to x_R then $\arctan(x/x_R) \approx (x/x_R)$. This creates new contributions to Δk in Eq. (2.58) of the form $\pm(2p_{S,I} + 2|\ell| + 2)/x_R$. For example: if the $p_S = p_I = \ell = 0$ term is phase matched for a cavity with $w_S = w_I = 49.5$ µm then signal's $1/x_R$ is 0.05595 per mm. which causes a df detuning of 26.20 GHz. This causes $\mathcal{F}(1, 0, 0)$ to be peaked near ω of 52.40 GHz instead of at degeneracy. Similarly, the idler's $1/x_R$ is 0.05876 per mm causing a phase shift of 26.47 GHz. These shifts should be compared to the 251 GHz FWHM from table 2.1. Thus the higher order L-G mode bi-photons will be

---

[2] This was partially because Mathematica™would occasionally crash, perhaps from a memory leak. Work was saved at each step so the computation could be resumed where it left off.

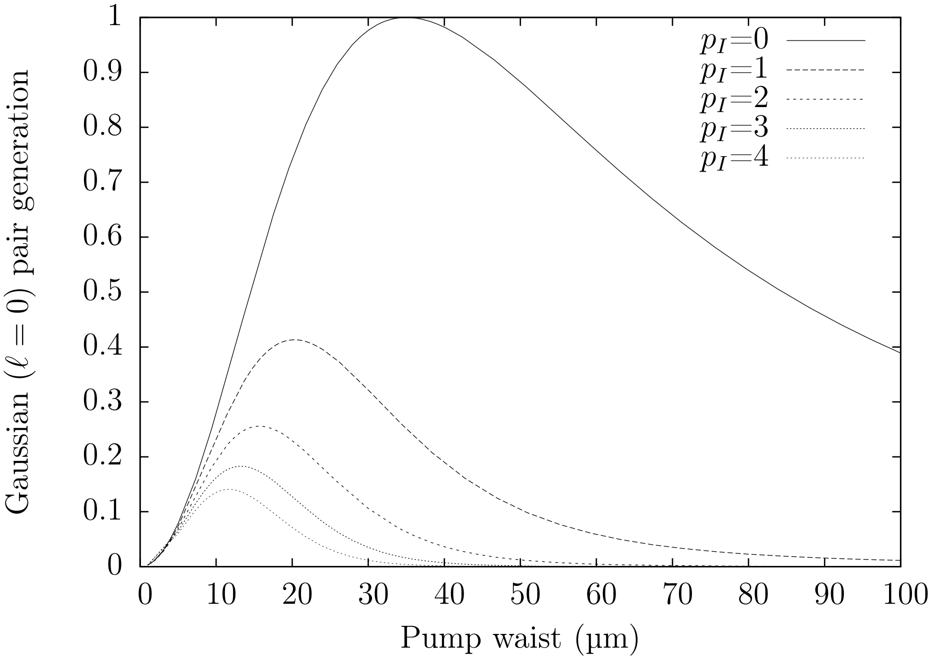

Figure 4-14: Scaled rate of downconversion $\mathcal{R}(0, p_I, 0)$ into the $p_S = \ell = 0$ bi-photons versus pump waist, assuming signal and idler waists of 49.5 µm. Normalized to have maximum 1, which occurs for pump waist of ∼35 µm.

significantly displaced from degeneracy and be much less polarization-entangled.

The preceding L-G mode calculation does not depend on the presence of a cavity, and can be equally well applied to the single-pass case of chapter 2. Therefore the $\mathcal{R}(0, 0, 0)$ can be understood as the collection rate into single mode fibers which collect a certain Gaussian waist in the crystal. However, the Gouy phase interacts with the cavity since it also changes the effective cavity length. For a given pump frequency the mirror location has to be moved some fraction of the FSR to resonate the higher-order L-G mode bi-photons. This spatial-mode selectivity is another feature of cavity-enhanced downconversion that can be advantageous.

The downconversion into Gaussian signal and idler modes with the cavity waist of 49.5 µm is shown in the upper curve of Fig. 4-14. The maximum rate $\mathcal{R}$ is found for a pump waist of approximately 35 µm, which is $49.5/\sqrt{2}$. This optimal pump waist is approximately $49.5\mu\text{m}/\sqrt{2}$, which agrees with the second-harmonic-

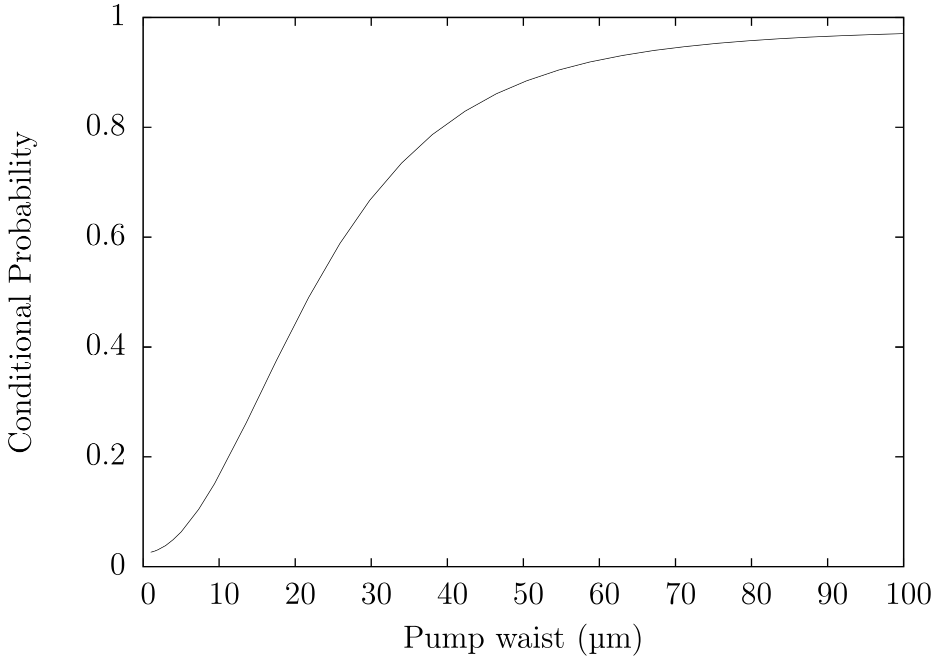

Figure 4-15: Conditional probability of a coincidence for signal and idler collected into lossless single-mode fibers.

generation optimum in Ref. [12]. This maximizes the number of Gaussian pairs collected into fibers, but not the conditional probability. The $\mathcal{R}(0, p_I > 0, 0)$ and $\mathcal{R}(p_S > 0, 0, 0)$ types of pairs will have one photon that can be collected but not both. These rates $\mathcal{R}(0, p_I, 0)$ are also shown in Fig. 4-14; the conditional probability will be worse for pump waists smaller than 35 µm and better for larger waists. Note that $\mathcal{R}$ is nearly symmetric with respect to the p's: $\mathcal{R}(p, q, \ell)$ $\mathcal{R}(q, p, \ell)$ differing by at most 2%, so their plots would appear identical on the scale of Fig. 4-14.

For the optimal pump waist, the phase shift df from forward-degenerate plane waves is 0.0257 THz. This can be compensated for by reducing the PPKTP temperature by .286° C, according to tuning coefficients in Eq. (2.58). The higher order modes will then be detuned from degeneracy by a multiple of ~50 GHz as noted above. This detuning is the location of the peak output frequency of the sinc phase-mathching function. These high order modes will be in resonance at cavity positions shifted by the Gouy phase.

For the optimal pump waist of 35 µm and totaling p_S, p_I from 0 to 4 and ℓ of -4 to 4, the rate $\mathcal{R}(0,0,0)$ is 10% of the output. Considering only the $\ell = 0$ output, the rate $\mathcal{R}(0,0,0)$ is 31% of the output. Considering the $p_S = 0$ and $\ell = 0$ output, the rate $\mathcal{R}(0,0,0)$ is 75% of the output. This last figure of 75% is the conditional probability expected for otherwise lossless collection into single mode fibers from a single-pass downconverter, and can be approximated by $1 - \mathcal{R}(0,1,0)/\mathcal{R}(0,0,0)$ for any pump waist. This has been plotted in Fig. 4-15. But since the rate is also affected by the doubly-resonant cavity this 75% only applies to having no cavity or to an average from sweeping over the cavity FSR. The other contributions are suppressed at a cavity mirror position where $\mathcal{R}(0,0,0)$ is resonant.

4.4.2 Non-Perturbative Calculation

Instead of expanding the Hamiltonian, one can expand the generator of progression $\widehat{G}(x)$. The transverse spatial integral of Eq. (2.37) is the integral over θ and r that can be performed analytically to get $F(...)$. Now $G_{NL}(x)$ is a sum over p_S, p_I, ℓ_S, and ℓ_I and instead of the perturbative numerical integration along x to get $\mathcal{F}(...)$, there are the derivatives

$$\frac{\partial \widehat{a}^{+}_{S,I}(p_{S,I}, \ell_{S,I}, \omega_{S,I}; x)}{\partial x} = \frac{i}{\hbar}\left[\widehat{a}^{+}_{S,I}(p_{S,I}, \ell_{S,I}, \omega_{S,I}; x), \widehat{G}_0(x) + \widehat{G}_{NL}(x)\right], \tag{4.55}$$

which result in infinite sums:

$$\begin{aligned}\frac{\partial \widehat{a}^{+}_{S}(p_S, \ell_S, \omega_S; x)}{\partial x} = {} & ik_S \widehat{a}^{+}_{S}(p_S, \ell_S, \omega_S; x) + \\ & i\mathcal{K}\sum_{p_I=0}^{\infty} \widehat{a}^{+\dagger}_{I}(p_I, -\ell_S, \omega_P - \omega_S; x) F(p_s, p_I, \ell_S, \omega_S - \omega_P/2; x).\end{aligned} \tag{4.56}$$

$$\begin{aligned}\frac{\partial \widehat{a}_I^{+}(p_I,\ell_I,\omega_S;x)}{\partial x} &= ik_I\widehat{a}_I^{+}(p_I,\ell_I,\omega_I;x)+\\ &\quad i\mathcal{K}\sum_{p_S=0}^{\infty}\widehat{a}_S^{+\dagger}(p_S,-\ell_I,\omega_P-\omega_I;x)F(p_s,p_I,-\ell_I,\omega_P/2-\omega_I;x).\end{aligned} \tag{4.57}$$

Altogether, this is an infinite system of first-order linear differential equations for each ℓ value. For reasonable experimental arrangements the system can be truncated and numerically solved. The result will express the field operator $\widehat{a}_S^{+}$ after the crystal as a linear combination of all the $\widehat{a}_I^{+\dagger}$ and all the $\widehat{a}_S^{+}$ before the crystal with comparable ℓ, not just a single a_S^{+} and $a_I^{+\dagger}$. In the low power limit, only the single corresponding a_S^{+} should survive with a unit amplitude coefficient and the $a_I^{+\dagger}$ coefficients should agree with the perturbative calculation of $\mathcal{F}(...)$.

The non-perturbative system of differential equations needs to be solved only when the system is not in the low-power limit, or when the cavity input is not in a vacuum state. For the experimental regime explored here the low-power limit suffices, and the perturbative calculation can be used. Thus in Eq. (4.2) the $\mu(\omega)$ can be replaced by 1 and $\nu(\omega)$ by the $\mathcal{F}(p_S,p_I,\ell,\omega)$ functions.

Chapter 5

Cavity Experiment

> 'Many things I can command the Mirror to reveal,' she answered, 'and to some I can show what they desire to see. But the Mirror will also show things unbidden, and those are often stranger and more profitable than things which we wish to behold. What you will see, if you leave the Mirror free to work, I cannot tell. For it shows things that were, and things that are, and things that yet may be. But which it is that he sees, even the wisest cannot always tell. Do you wish to look?'
>
> **J.R.R. Tolkien**, *The Fellowship of the Ring*

5.1 Early designs

Several attempts were required before the final cavity downconversion experiment was made. The first cavity system that was explored, even before the single-pass PPKTP work, was based on a pre-existing OPO [26]. This was a single-angle phase-matched type-II KTP downconverter in a single-ended cavity. The OPA was used for degenerate conversion of the 532 nm pump to 1064 nm signal and idler. The silicon single-photon detectors had very low (1-2%) quantum efficiency at 1064 nm. The pair detection rate was very poor, about 10 Hz or lower, and heavily masked by unpaired single photon detection events, which were frequent enough to create accidental coincidences within the cavity lifetime. The real coincidence rate could be estimated only by fitting the timestamped events at the two detectors. The pump was cw but the time-stamped acquisition could only run at 10% duty cycle due to hardware bandwidth. Since there was no birefringence compensation, the resonant output was not entangled, though it clearly affected the signal and idler detection rates. It was the non-resonant output which provided an interference signal in the coincidences when the type-II output was measured at 45°.

The next experiments performed were to characterize the PPKTP with a single-pass pump and are described in chapter 3. The first cavity design called for using a PBS inside the cavity to have the signal and idler travel to separate high reflectors [30]. This spatial separation could be used instead of a compensating crystal to adjust the FSR of the two polarizations to be equal. The cavity required a high quality brewster-angle plate PBS with very low ($< 0.2\%$) losses for both polarizations, and the actual optics that were delivered did not meet the stringent specifications. After a second round of optics could not fix the problem the cavity had to be redesigned, leading to the KTP CC + PPKTP + KTP CC layout modeled in the previous chapter.

The existing OPO's monolithic mount was reused to house the PPKTP and two KTP compensating crystals. However, fitting the three temperature-controlled crystals in the cavity and aligning them with the mostly fixed mirrors was too inflexible. The mirrors and crystals were transferred to separate and adjustable mounts. At this time an experiment was performed using a quarter-wave-plate (QWP). The peaks with an odd number of different round trips for signal and idler vanish when analyzed in the 0° basis since the signal and idler have left the cavity with the same polarization. This could not be as useful for teleportation, but was a good test of the cavity resonance and the histogram collection since the detected coincidence peaks had spacings of twice the round-trip time. In the 45° basis the even and odd peaks are equally detectable. The QWP was not anti-reflection coated and the losses resulted in poor cavity finesse and quick fall-off of peak amplitude with each round trip.

The next attempt was to assemble the KTP+PPKTP+KTP cavity. Using a probe beam to simultaneously align the signal and idler polarization modes in this cavity revealed a flaw: the PPKTP crystal's input and output faces were not sufficiently parallel. The probe light at 45° polarization was a single beam entering the output coupler, but after the PPKTP the horizontal and vertical polarizations were traveling along slightly separate paths. This was mainly a vertical (z) deflection of the vertical-polarization with respect to the horizontal. This made aligning the high reflector to reflect both beams at normal incidence at the same time a difficult task. Nevertheless, there was a geometry that could do so and after careful alignment the experiment was run, but the result did not exhibit any noticable polarization entanglement. The worry was that the separated signal and idler paths in the cavity created some residual distinguishability. In addition to the other difficulties, the PPKTP was at least 0.1 mm shorter than the total of the two KTP compensating crystals, thus creating an imbalance in the signal and idler round-trip times.

Rather than continuing to struggle with the defects, the PPKTP was sent to be re-polished so that the input and ouptut faces were parallel, followed by the replacement of the anti-reflection coating. At the same time a new KTP compensating crystal was purchased which was polished and coated alongside the PPKTP so their lengths would be well matched. A tunable Ti:S laser was used to make separate measurement of the birefringence of the PPKTP and KTP crystal over 40 nm of bandwidth. By fitting each data set to the Sellmeier equations, the length of each crystal could be inferred to be 9714±1 µm and 9713±1 µm, respectively. The difference is less than the 4.5 µm distance between successive double-resonant conditions as computed in section 4.2.3. Fine tuning with the temperature is still necessary, but the residual FSR difference will be very slight.

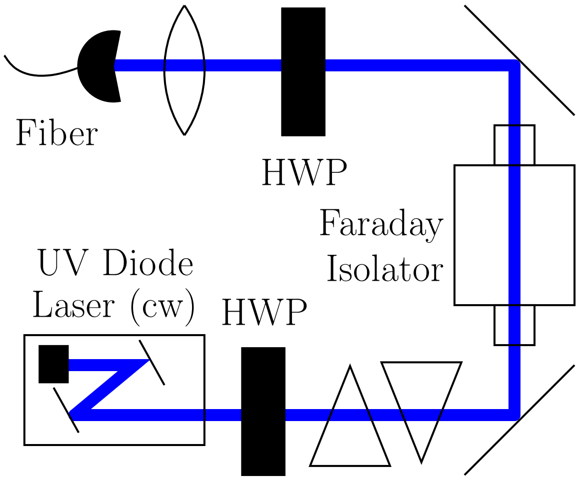

Figure 5-1: Layout for the pump section. The diode is grating-stabilized, reshaped by the anamorphic prism pair, isolated, and coupled into 1 meter of single mode fiber.

5.2 Setup

A schematic of the experimental setup is shown in Fig. 5-2, with the pump section shown in Fig. 5-1. The pump laser itself was the same as in the single-pass experiment (see section 3.1). The UV fiber was single mode and was from Stocker Yale, model NUV-320-K1, and a 20%-25% coupling efficiency was achieved. After the cavity OC there was a lens to collimate the signal and idler output. Three dichrioc mirrors (DM) were used to remove the pump beam. The first of these mirrors diverted the pump to a photodiode so the weak cavity resonance of the pump could be monitored. The other two mirrors were tilted in reverse so the total displacement of the transmitted beam was minimized. There were then two steering mirrors (not shown). Next was a 5 mm long KTP compensating crystal, followed by the aspheric lens that collected the signal and idler into the single-mode fiber. The 2 m long fiber was wound around three polarization control paddles. The fiber output passed through a collimator and then a lens so that the beam focused and expanded before being focused tightly onto a detector. After that lens there was the interference filter, which was tilted to admit the degenerate wavelength. Next, the 50-50 beam splitter separated the photons into two arms. The reflected photons were analyzed with a HWP and PBS and collected

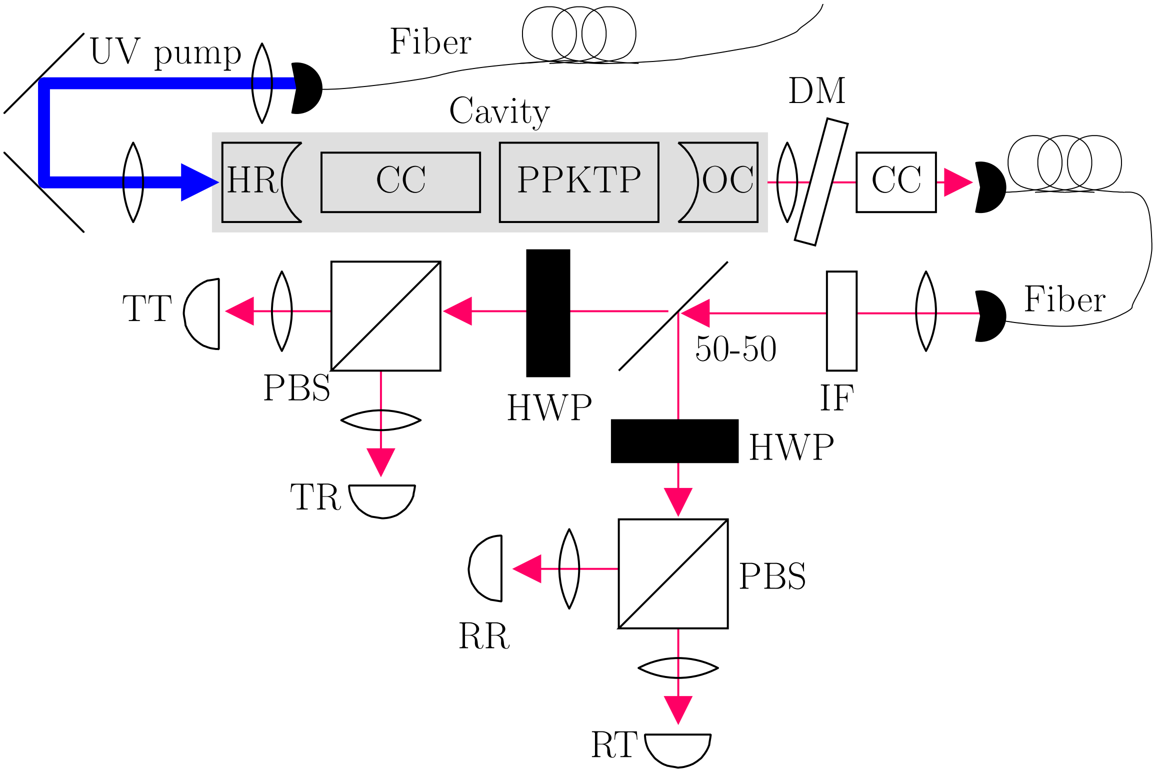

Figure 5-2: Schematic of experimental setup for cavity-enhanced downconversion. The KTP CC inside the cavity is the same length L as the PPKTP crystal. The KTP CC outside the cavity is 5 mm long. The pump is transmitted by the HR and OC, and reflected by the dicroic mirror (DM). The four detectors are labeled TT, TR, RT, and RR.

onto the RT and RR detectors. The transmitted photons were analyzed with their own HWP and PBS and collected onto the TT and TR detectors.

5.3 Cavity Parameters and Tuning

The cavity mirrors had 50 mm radii of curvature, and were located 104.9 mm apart. The crystals were 9.713 mm long and reduced the optical path to an effective separation of 96.1 mm for calculating the cavity focus (w_0) of 49.5 µm. The pump focus (w_P) was close to the optimal value of 35 µm. The crystals expanded the cavity to an effective phase separation of 120.3 mm of free space, which produced a FSR of 1.246 GHz and a round trip time of 802 ns. The largest stable separation of the mirrors corresponded to a 1.207 GHz FSR and a 829 ns delay, so the system is close to the maximum time separation and minimum bandwidth. The cavity finesse was measured to be ∼55, which implied an 11% cavity loss per round trip, consistent with the 92% reflection of output coupler and ∼0.3% loss per surface (including reflections) per round trip.

The PPKTP crystal temperature was adjusted for frequency-degenerate operation and for efficient collection of the frequency-degenerate signal and idler outputs. This was much like the single-pass case, but the collection was into the cavity Gaussian modes instead of free space through a fixed iris. The KTP compensating crystal (CC) in the cavity was temperature tuned so that probe light at nearly twice the pump wavelength had simultaneous transmission peaks for the two polarizations. The residual round-trip birefringence in the cavity was then an integer number of wavelengths. Each extra wavelength shifted the FSR difference by an otherwise immeasurable 4.1 kHz, but had a cummulative effect on the obtainable double resonance and polarization entanglement. The crystal length implied a single-pass correlation time between signal and idler of $L\Delta k'/c = 3.43$ ps, and each extra wavelength of birefringence shifted the timing by 2.65 fs per round trip, which was a fractional shift of about 1/1294. The crystal lengths and temperature were well matched and were likely to have no more than a 4-wavelength birefringent shift. The simultaneous double-resonance from tuning the CC temperature was observed to recur every ~4.5° C as the birefringent shift gained or lost a wavelength.

The UV pump was operated at 397.343 nm (vacuum) with ~1 mW of power delivered to the cavity. The collection fiber was aligned to the cavity, and the internal KTP compensating crystal was temperature tuned, by bringing IR laser light backwards as a probe and examining the light transmitted through the cavity onto a photo-diode. Aligning the forward UV-pump light was accomplished by overlapping it with the backward IR probe laser, assisted by auxillary irises in and out of the cavity, and by maximizing the pump laser's cavity resonance amplitude. The IR probe was also used to measure the cavity finesse of ~55 and calibrate the mirror's piezo-voltage for an FSR sweep.

5.4 Interference Dip

The interference dip experiment was performed, similiar to the single-pass version in section 3.3, to detect the polarization-entanglement of the output pairs. The coincidence rate between the RT and RR detectors was measured in the 0° basis. Simultaneously, the coincidence rate between the TT and TR detectors was measured in the 45° basis (or the 0° basis for calibration). When recording data, the cavity piezo voltage was driven by a triangular voltage waveform. This swept the cavity mirror by a FSR for the degenerate 795 nm output (i.e. the mirror translation distance was 397.5nm). The sweep period was 40 seconds.

Some of the resulting data is shown in Fig. 5-3 where a 3 nm IF was used, and in Fig. 5-4 where a 1 nm IF was used. There are several features of note in the data. The RR singles rate was anomalously high, due to a light-leak in the shielding of the detectors, and can be ignored. The output double resonance occured every FSR/2,

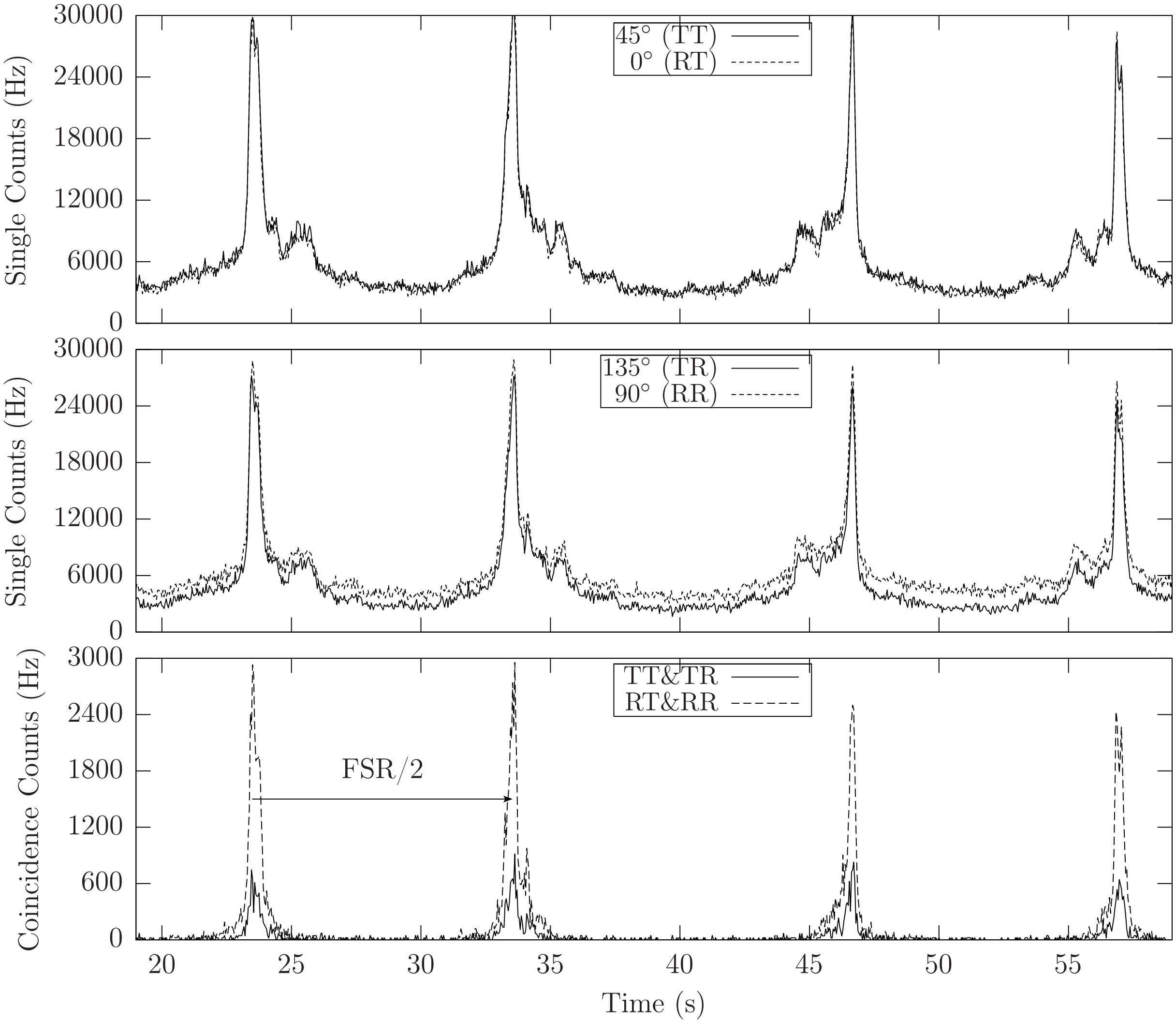

Figure 5-3: Plot of singles and coincidence rates during a cavity sweep, using a 3 nm IF. The cavity length sweeps across a FSR and back over 40 s, with a 24 Hz count rate. There is a resonance peak every FSR/2. The 45° basis coincidence rate is less than half the 0° basis rate, showing the interference dip.

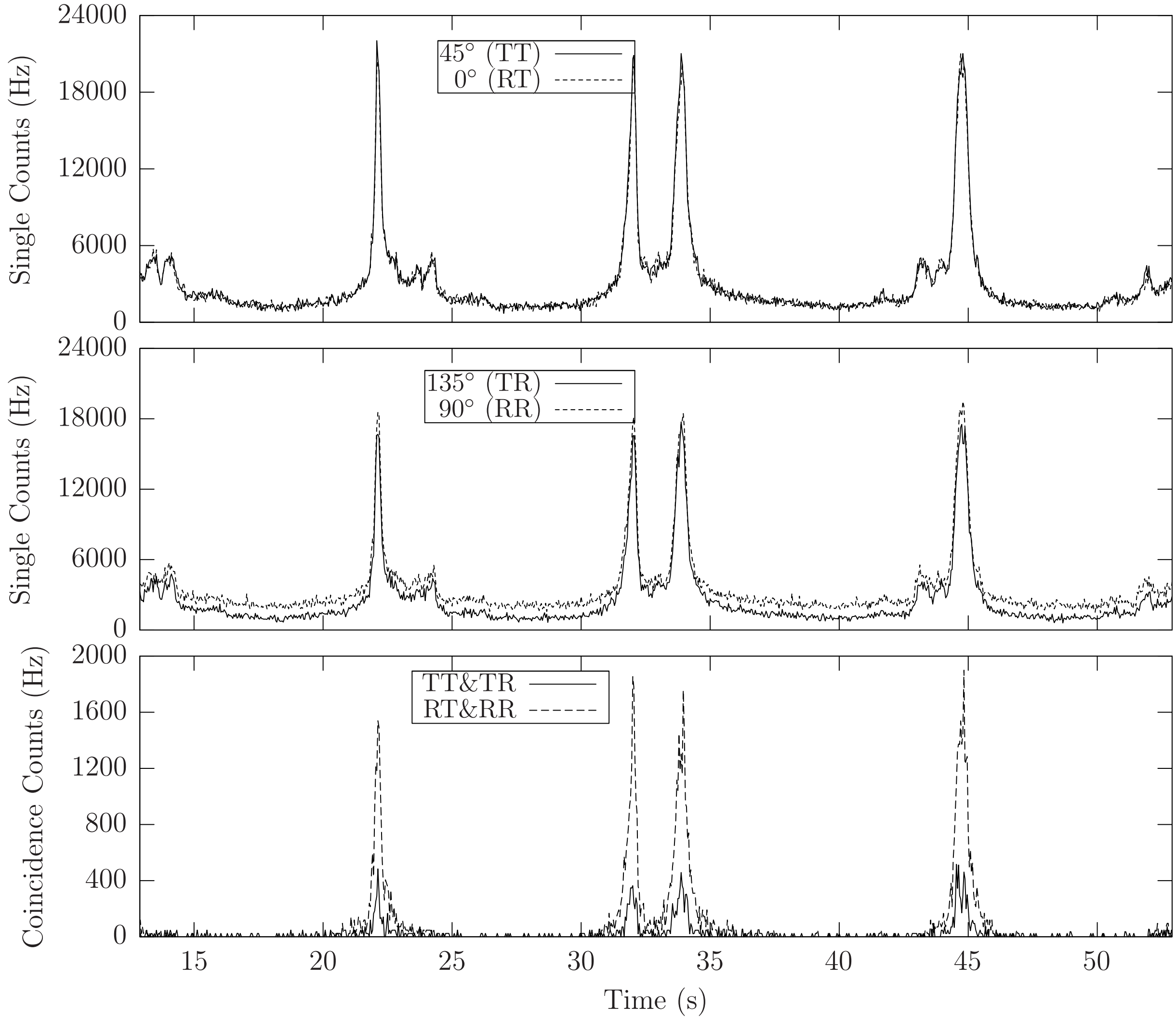

Figure 5-4: Plot of singles and coincidence rates, similar to Fig. 5-3, but using a 1 nm IF.

twice in each half of the sweep. This agrees with the resonance periodicity in Eqs. (4.9) and (4.14). One of these peaks is the "even" degenerate peak and the other is the "odd" peak with no output at degeneracy, but which is which cannot be discerned from the data. In addition to the double-resonance peaks, there were nearby side peaks in the single rates. These side peaks did not correspond to any features in the coincidence rate, and were due to resonant production of pairs with Gaussian signal and non-Gaussian idler photons, and vice versa. Only the Gaussian half of these pairs was detected, since both members of these pairs could not propagate in the single-mode fiber. Their resonant position in the cavity sweep was displaced from the primary peak due to the Gouy phase shift. The most important feature in the figures is that the reduction in the amplitude of the coincidence peaks in the 45° basis compared to the 0° basis was more than 50%. This reduction was consistent as the cavity length was swept through resonance, which emphasizes that the production of polarization-entangled output is distinct from the production of doubly-resonant output. The conditional probability of coincidences in the 0° basis was ∼8%, which compares favorably to the rate seen in single-pass free-space collection of ∼24% (which did not have the 50% reduction from the beamsplitter) . The background rate of single-count events is likely due to fluorescence driven by the pump, with some off-resonant pair production in addition. Summing the coincidence rates across several sweeps of the cavity, the maximum visibility achieved was 73%.

The interference dip weakened and disappeared when the internal KTP compensating crystal temperature was varied by a few times the ∼0.1° C resolution of the stabilized temperature stage. To improve the visibility the PPKTP crystal may need to be temperature tuned, with an accompanying change in the CC temperature.

The output from the TT and RT detectors was also used to collect a start-stop arrival time histogram with the Picoquant Timeharp 200. Histograms for the 0° and 45° bases using a 1 nm IF, each collected over 16 minutes while the cavity was being swept, are shown in Fig. 5-5. The resolution of the discrete peaks was limited by the

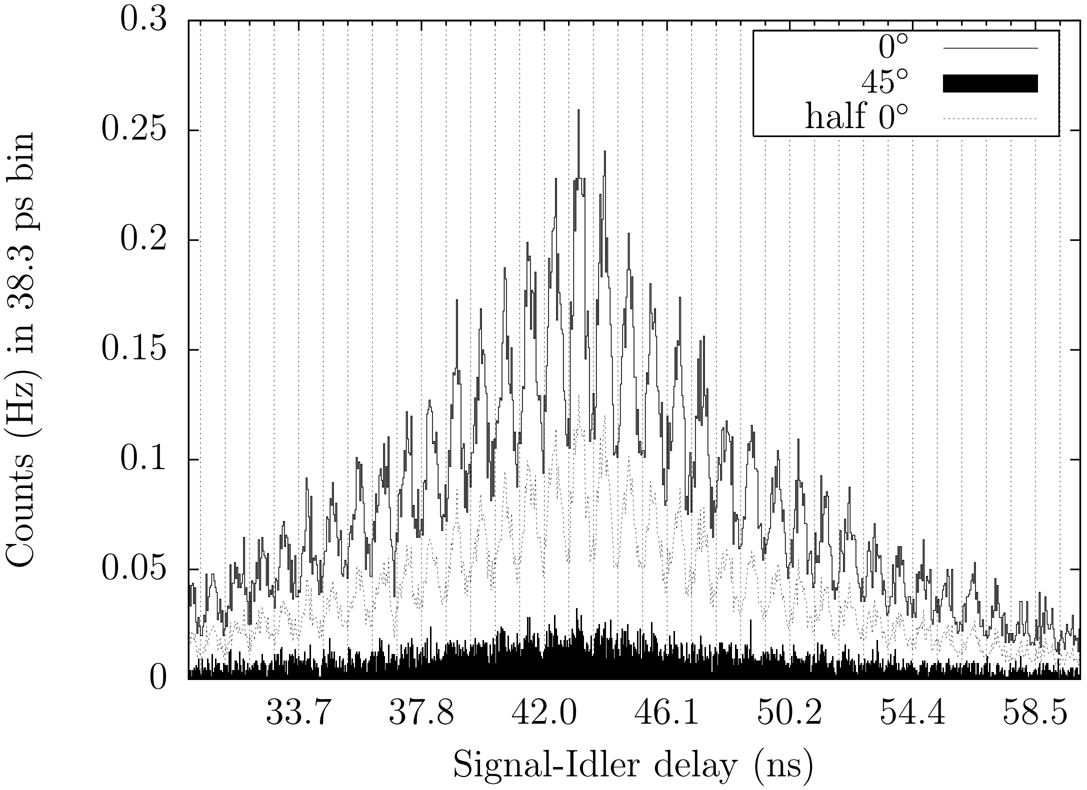

Figure 5-5: Histogram averaged over 16 minutes and collected through a 1 nm IF. The polarization-entanglement reduces the 45° basis coincidence interference dip below half of the 0° basis' rate. The separate peaks are from the signal and idler leaving the cavity after a different number of round trips. The peak spacing is 826 ps. The cavity length was continuously swept during acquisition through one FSR with a 40 s period triangular voltage waveform.

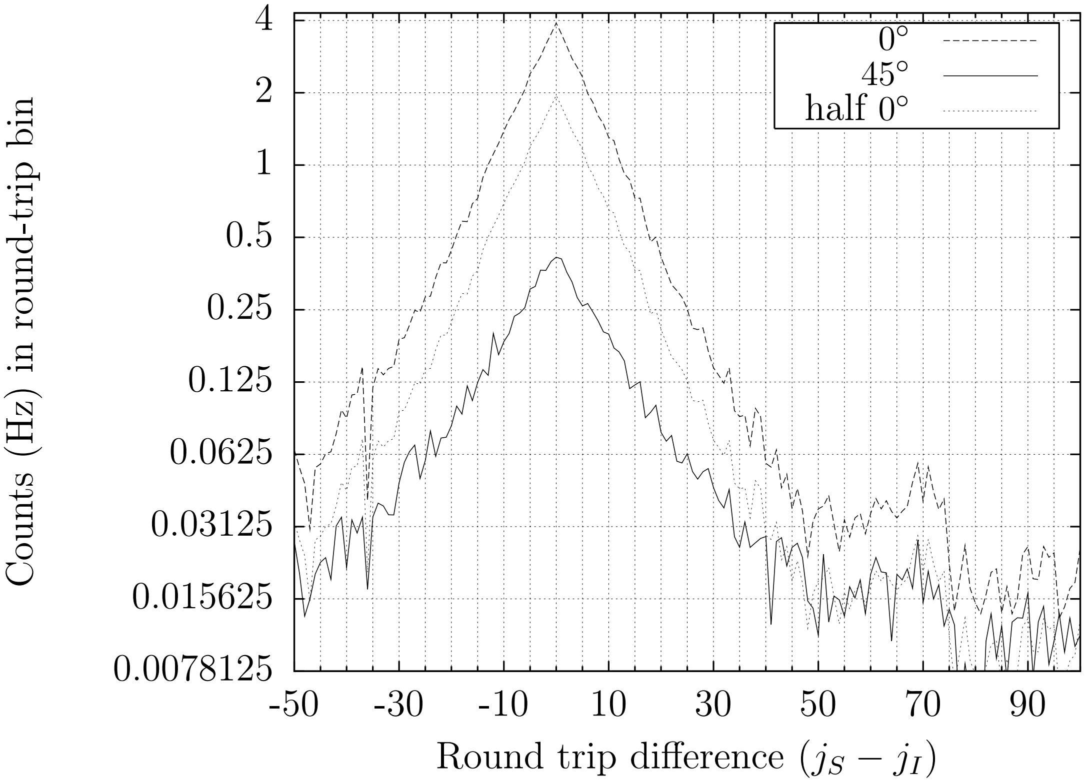

Figure 5-6: Log-scale (in base 2) histogram showing the interference dip. Same data as in Fig. 5-5 where the data for each peak has been totalled. The vertical grid has a line for every 5 round-trip peaks.

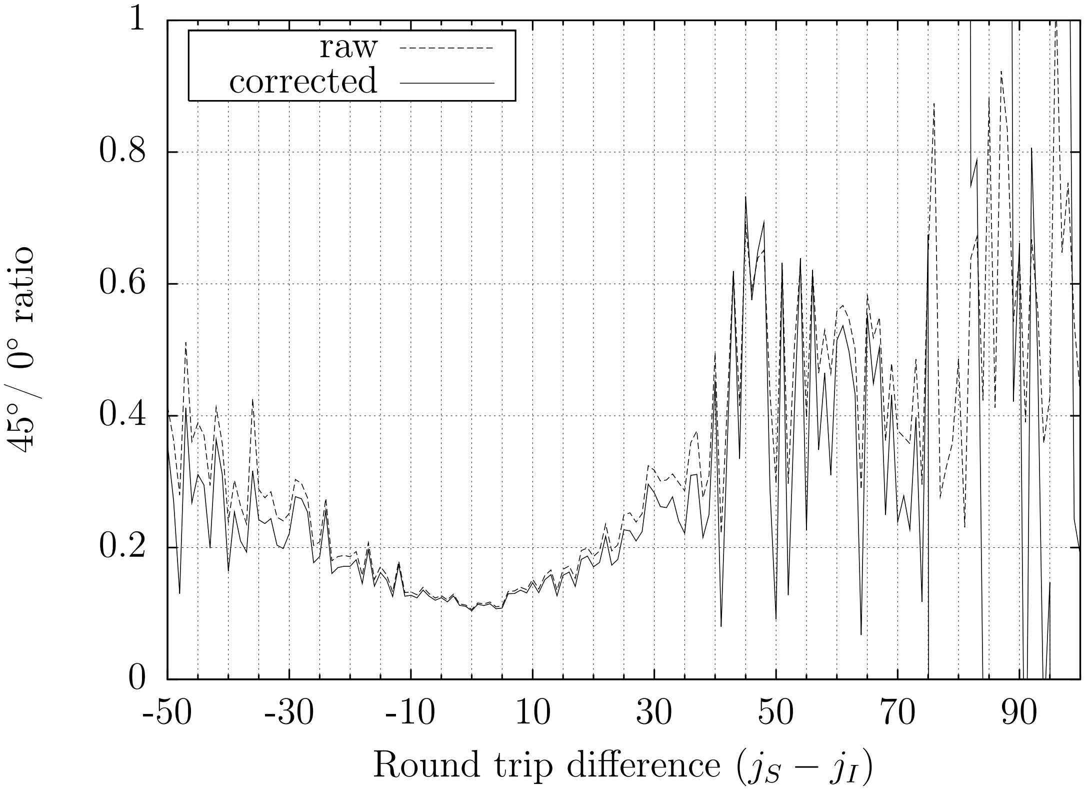

Figure 5-7: Same data as in Fig. 5-6 where the data for each peak has been totalled. The "corrected" line has had the average background accidental coincidence rates subtracted before taking the ratio. The vertical grid has a line for every 5 round-trip peaks.

timing jitter of the detector pulses, which was about 350 ps. The peak separation interval was extracted from a fit to the peaks and found to be 826 ps; the vertical lines show the separation of the data into different round-trip intervals. The histogram resolution of 38.3 ps allowed for 21.57 bins per round-trip interval. The data within each interval was binned and the result is shown in Fig. 5-6 on a log scale (in base 2). There is a vertical grid line every 5 round trips.

The counts in each peak should decline from the center with the ratio of the output coupler (OC) reflectivity R reduced by intra-cavity loss. This exponential decline is evident from the linear decline on the log-scale plot, and fitting this results in an R of 89%. This is consistent with the nominal 92% value for the OC and 0.3% loss per surface during a cavity round trip, and is also identical to the effective R deduced from the measured finesse. The 45° histogram was well below the classical prediction of half the 0° rate (shown on the figure to allow comparison).

The ratio of the 45° to the 0° data for each round trip is shown in Fig. 5-7. The dip was clearly better in the center of the histogram, with a slow increase as the number of extra round trips increases to either side. This is to be expected if the birefringence is not perfectly corrected. However, the central region of ±20 round trips accounts for 90% of the pairs. The average 45° to 0° ratio in this central region was 0.131, or a visibility of 76.8%. The central peak's ratio was 0.106, or a visibility of 80.8%. The variation of the interference dip can be attributed to a slight average temperature offset of 0.004°C from the equal FSR operating point.

5.5 Brightness

The brightness of the output was measured using the coincidence peaks in data like that shown in Fig. 5-4. The doubly-resonant peaks had a detected coincidence rate of 2000 pairs/s per mW of pump, after the single-mode fiber, 1 nm IF, and 50-50 beam splitter. However, that measurement was between the TT and TR detectors, which see only one quarter of the pairs after the beam splitter. Between the T and R sides of the beam splitter there were twice that many pairs, so a rate of 4000 pairs/s per mW of pump was inferred. This can be compared to several different free-space collection results that are also based on ∼1 cm of PPKTP generating ∼795 nm degenerate output. The cavity result is much higher than the 300 pairs/s per mW from the single pass source [31], which used an iris, 1 nm IF, and beam splitter. It is also higher than the 820 pairs/s per mW from the overlapping cone source [23] which used two irises, a 1 nm IF, and did not have a beam splitter. The very broadband double-pumped source [32] produced 12,000 pairs/s per mW with a very large iris and a wider 3 nm IF, and did not have a beam splitter.

It should be emphasized that the cavity output was measured after having been collected into one single-mode fiber. The coupling efficiency into the single-mode fiber could be partly inferred from the conditional coincidence rate of ∼8%. Comparing this to the single-pass rates without a cavity indicates that the fiber coupling was pessimistically 33% and likely near 50%. The inferred production rate from the conditional probability is 6.25×10^5 pairs/s/mW, which is comparable to estimates from our other PPKTP sources.

With the FSR of 1.23 GHz, finesse of 50, and phase-matching FWHM of 251 GHz, the central degenerate output peak should be 25 MHz FWHM and account for $1/225^{\text{th}}$ of the total output. This gives a spectral brightness of $2000 * 2/225/25 \approx 0.7$ pairs/s per mW of pump per MHz of bandwidth at degeneracy. The single-pass and overlapping-cone sources had a similar phase-matching FWHM but no cavity, so their brightness were, respectively, 0.001 and 0.003 pairs/s/mW/MHz. The double pump source was very broadband, but using a generous 3:1 ratio estimated from the 3 nm IF, the brightness was 0.014 pairs/s/mW/MHz. The cavity experiment reported in [11] used KbNO_3 crystals and type-I SPDC instead of type-II PPKTP, and its cavity-enhanced brightness (at the degenerate frequency) was 0.12 pairs/s/mW/MHz (this generously uses their calibrated rate which was higher

Set	CC (V)	T_{CC} (°C)	$\lvert 22.361°C - T_{CC} \rvert$	δT_{fit} (°C)	period v_0
a	1.3349	22.3514	0.0096	0.0203	216.3
b	1.3375	22.2577	0.1033	0.1040	42.37
c	1.3394	22.1891	0.1719	0.1694	25.97
d	1.3413	22.1206	0.2404	0.2509	17.54
e	1.3434	22.0449	0.3161	0.3192	13.78
f	1.3451	21.9836	0.3774	0.3793	11.60
g	1.3470	21.9152	0.4458	0.4544	9.68
h	1.3494	21.8287	0.5323	0.4942	8.90
i	1.3975	20.0984	2.2626	2.1773	2.021
j	1.2750	24.5210	2.1600	2.1666	2.031

Table 5.1: For the 10 data sets 'a' through 'j', the data for the measured KTP CC temperature and the temperature inferred from the fit of the interference dip are shown. The KTP CC thermistor voltage is translated to a temperature, and this is subtracted from 22.361. The last column is the v_0 fit of $\sin(\pi v/v_0)^2$ to the interference dip, the next to the last column is 4.4°C/v_0 which is the inferred temperature from the fit. The 22.361°C is the estimated ideal FSR temperature.

than their actual detected rate). This shows that the current cavity source is 50 to 700 times as bright as non-cavity sources, and at least 5 times brighter than the other reported polarization-entangled cavity source. From the 0.08 conditional probability and 0.7 pairs/s/mW/MHz, the inferred production rate from the cavity in the degenerate output peak in the Gaussian spatial mode was 110 pairs/s/mW/MHz.

From the mode-matching calculations, the fraction of the spontaneous output coupled into the Gaussian signal and idler spatial modes is 10% (section 4.4.1). Another way of looking at this is to consider that 90% of the potential output will be suppressed by the cavity, while the remaining 10% will experience the double-resonant enhancement. A system redesigned from scratch could improve this coupling and increase the brightness of the system, essentially by harnessing a greater fraction of the pump light.

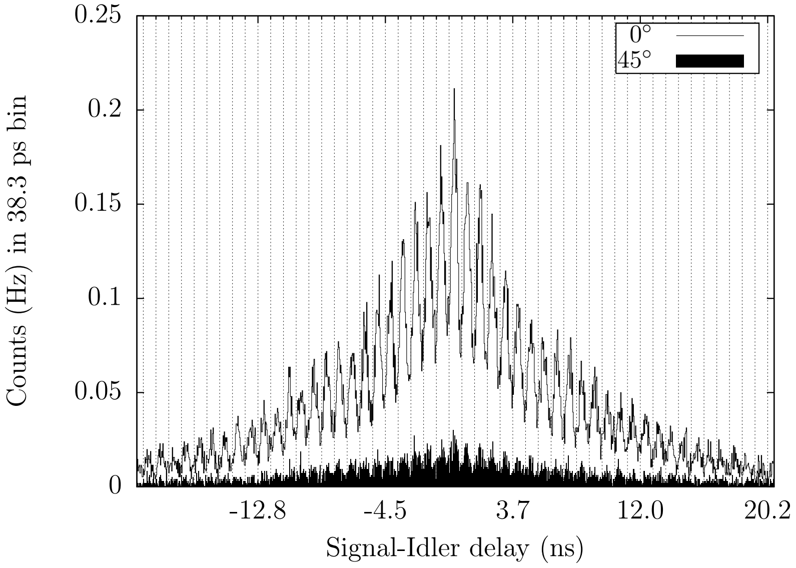

Figure 5-8: Raw histograms for set 'a'

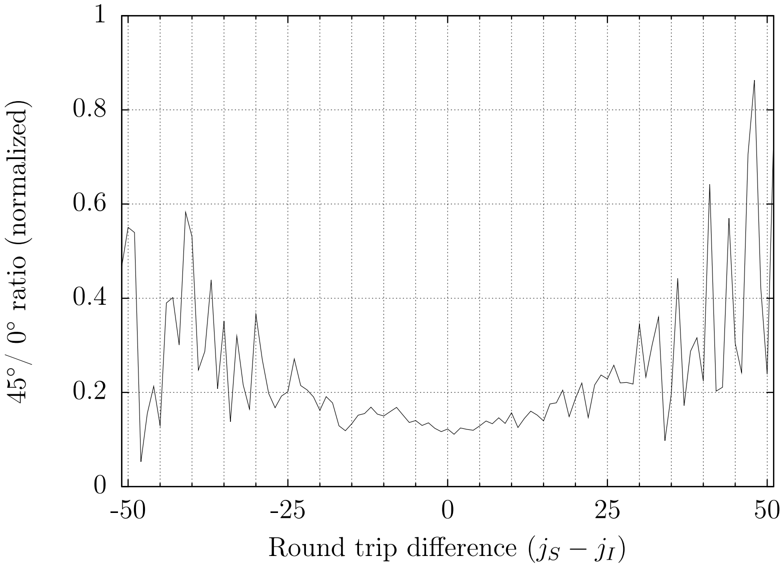

Figure 5-9: Normalized ratio for set 'a'

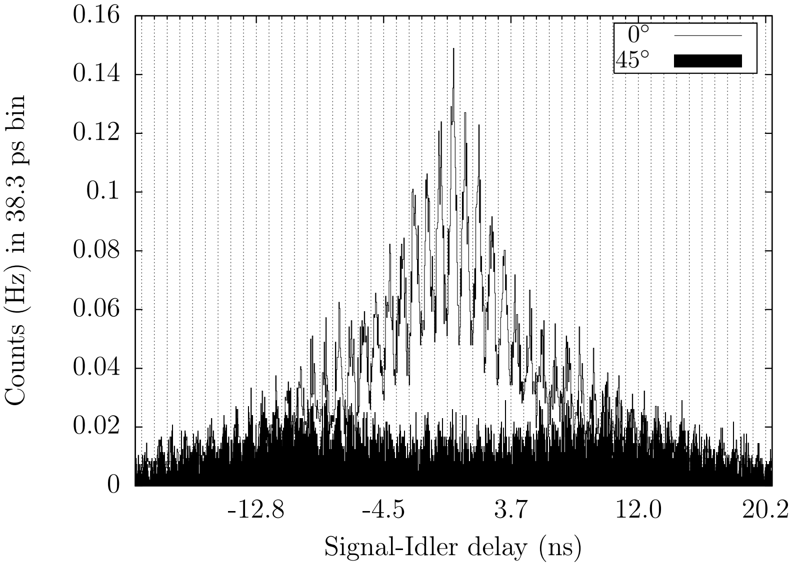

Figure 5-10: Raw histograms for set 'b'

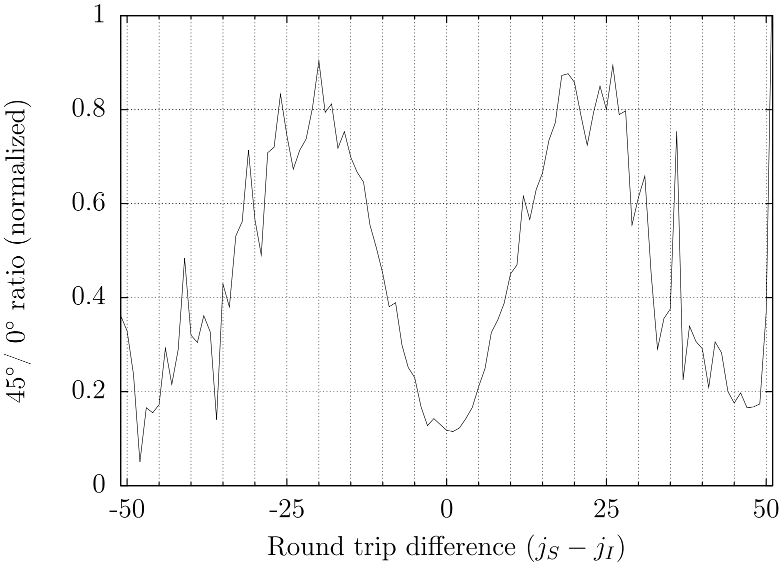

Figure 5-11: Normalized ratio for set 'b'

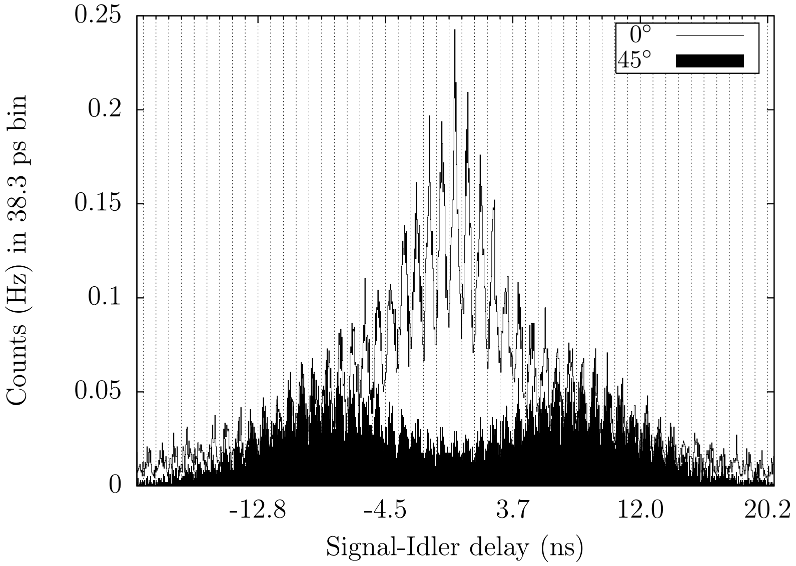

Figure 5-12: Raw histograms for set 'c'

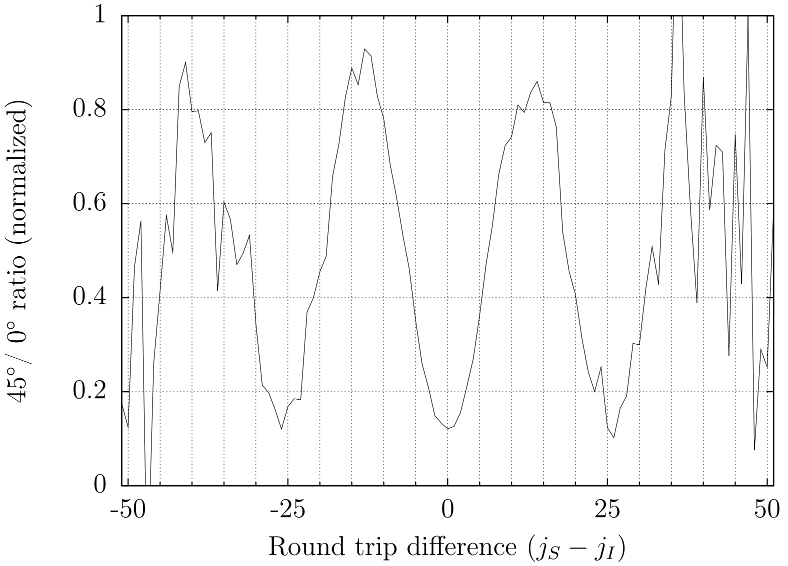

Figure 5-13: Normalized ratio for set 'c'

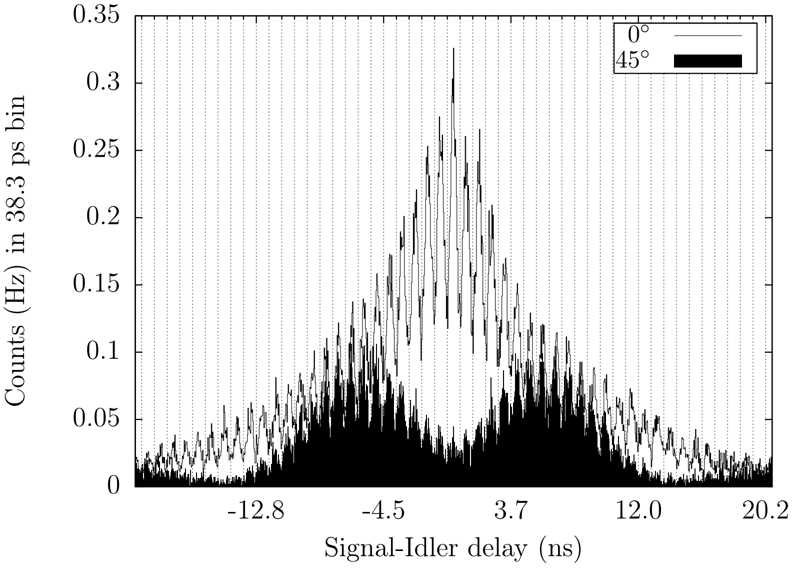

Figure 5-14: Raw histograms for set 'd'

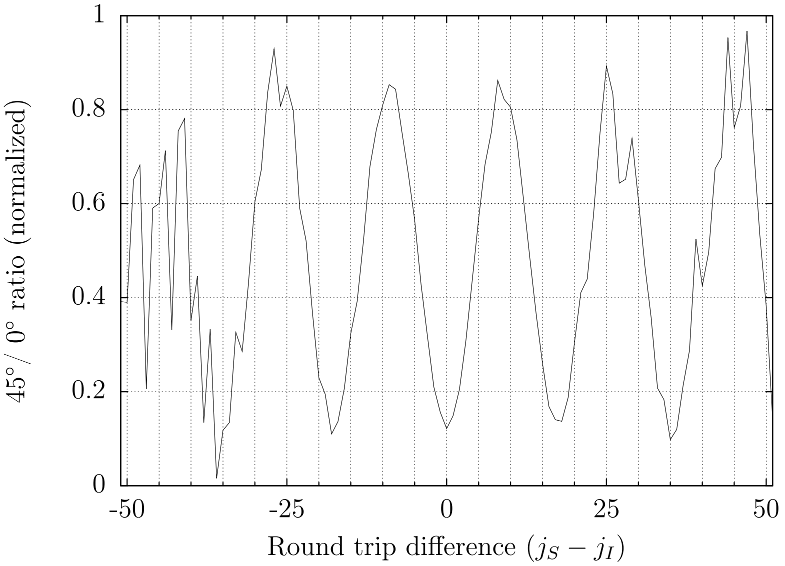

Figure 5-15: Normalized ratio for set 'd'

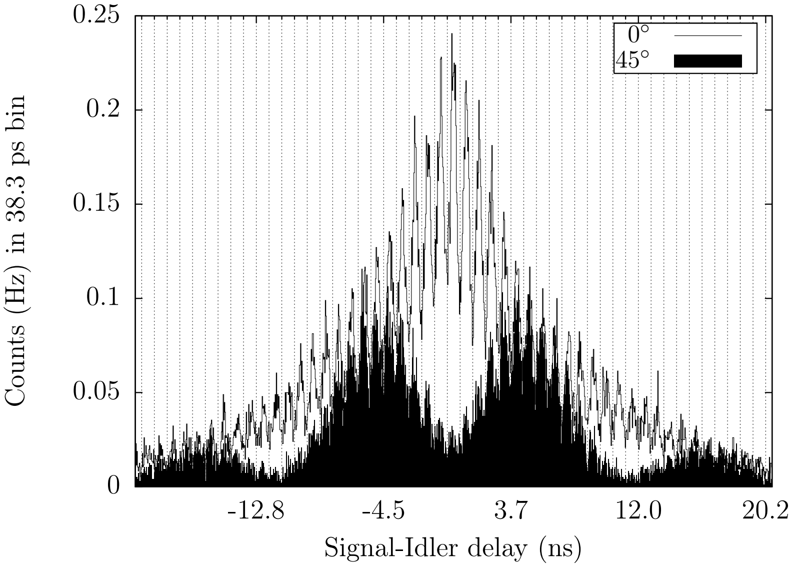

Figure 5-16: Raw histograms for set 'e'

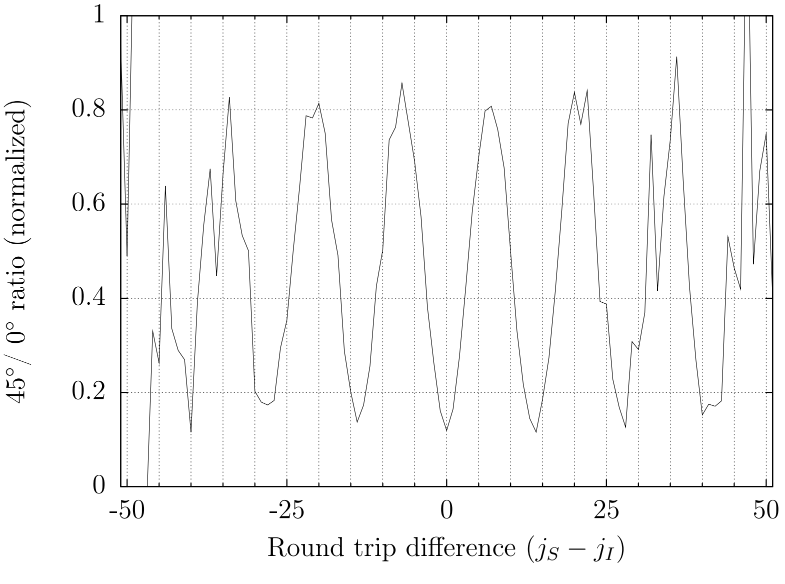

Figure 5-17: Normalized ratio for set 'e'

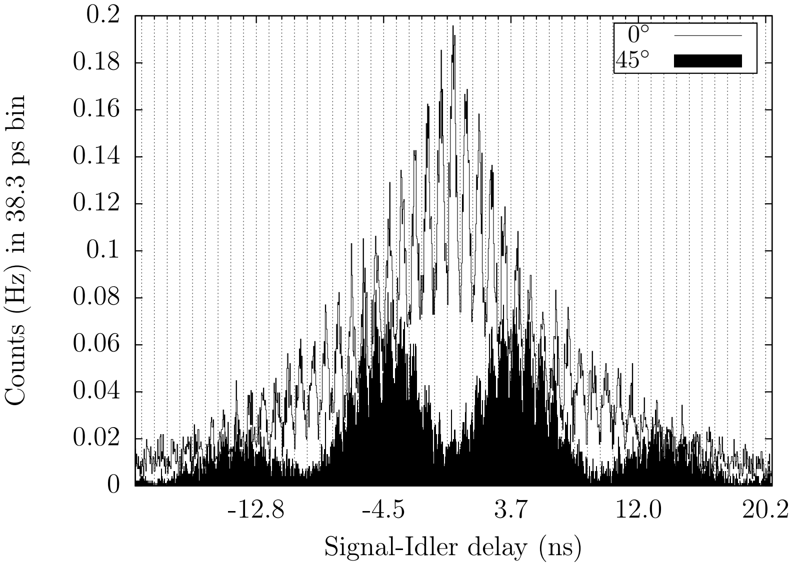

Figure 5-18: Raw histograms for set ’f’

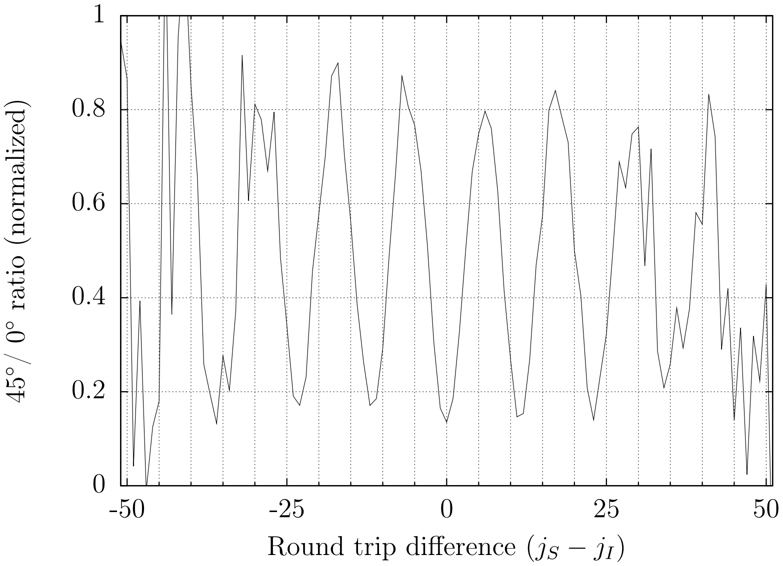

Figure 5-19: Normalized ratio for set ’f’

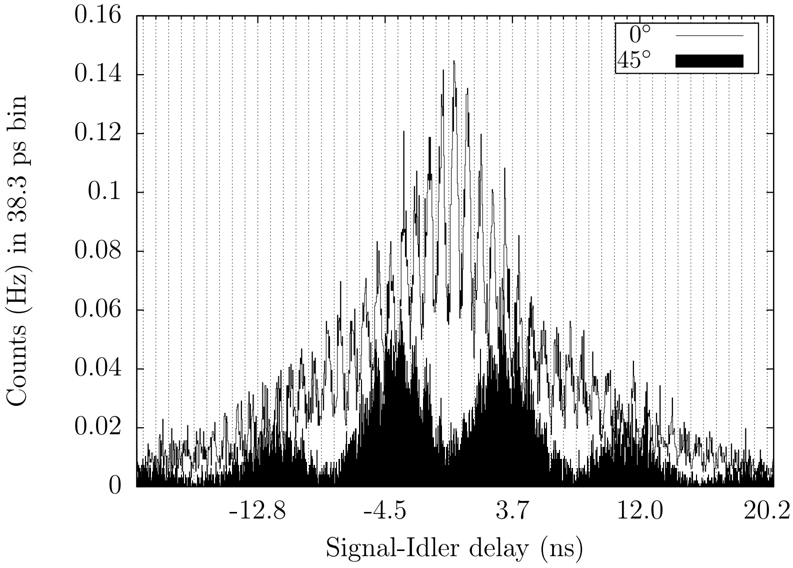

Figure 5-20: Raw histograms for set 'g'

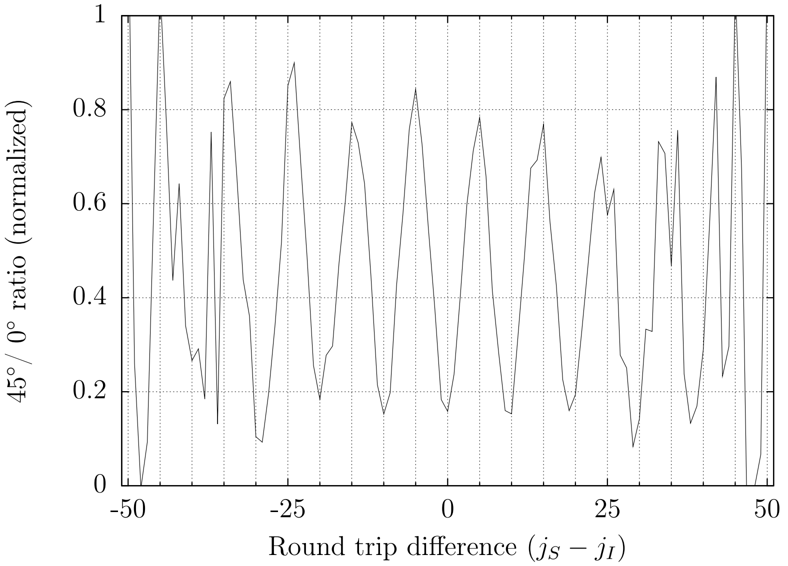

Figure 5-21: Normalized ratio for set 'g'

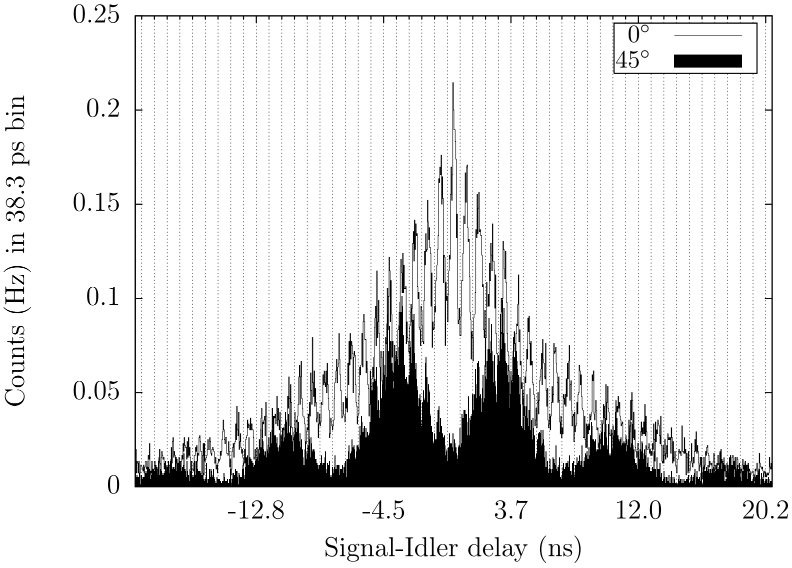

Figure 5-22: Raw histograms for set 'h'

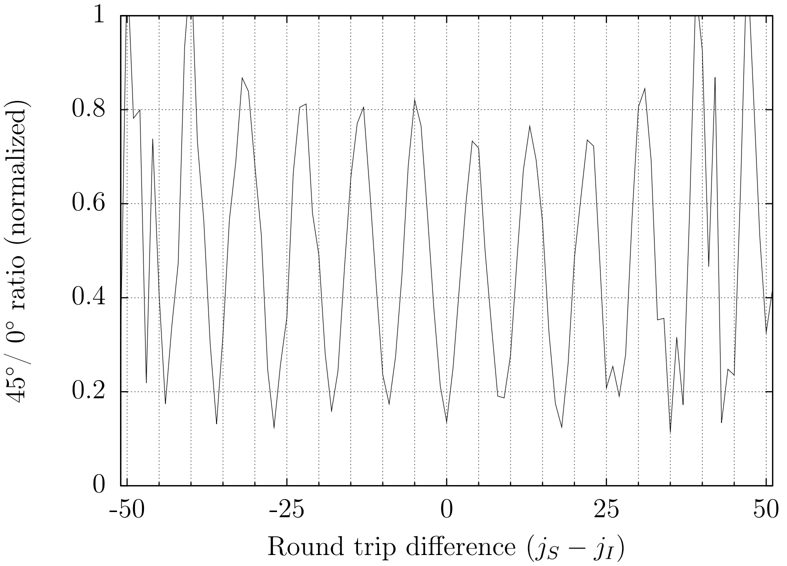

Figure 5-23: Normalized ratio for set 'h'

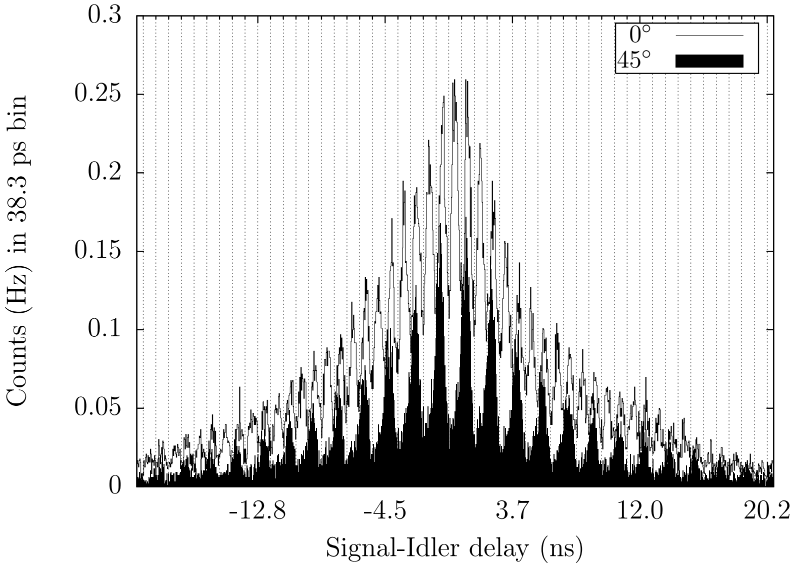

Figure 5-24: Raw histograms for set 'i'

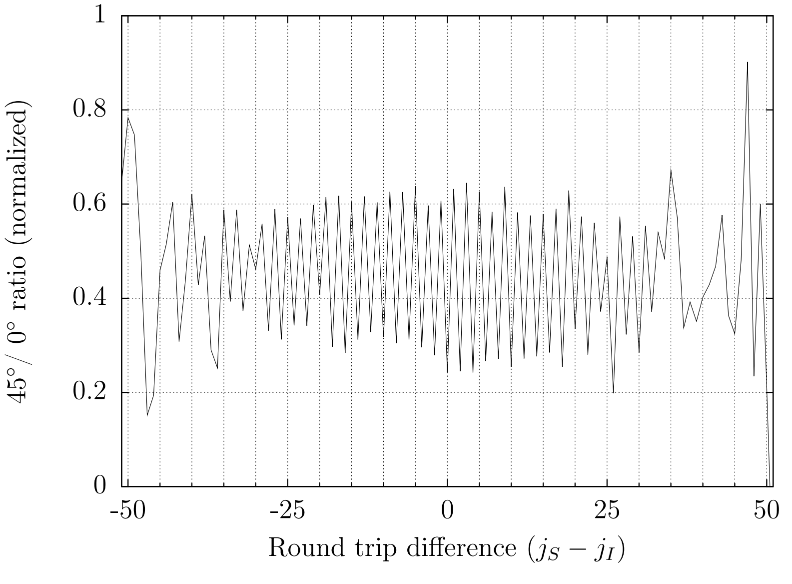

Figure 5-25: Normalized ratio for set 'i'

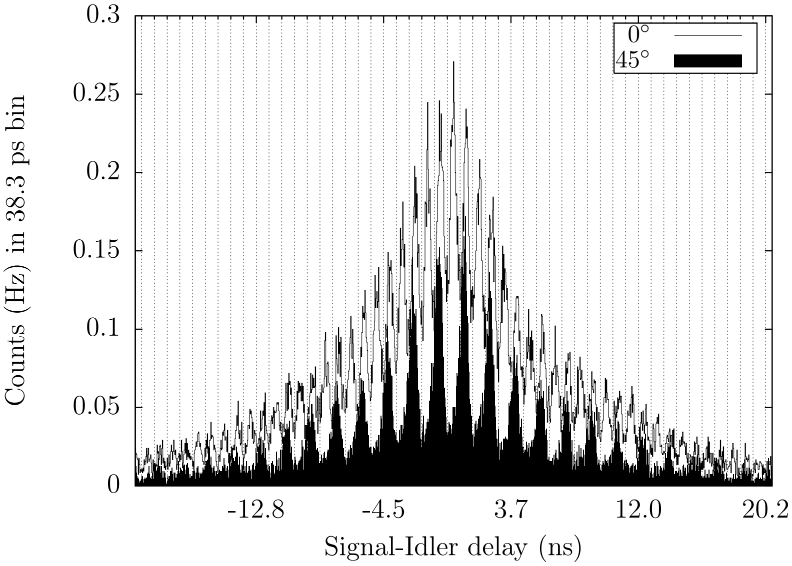

Figure 5-26: Raw histograms for set 'j'

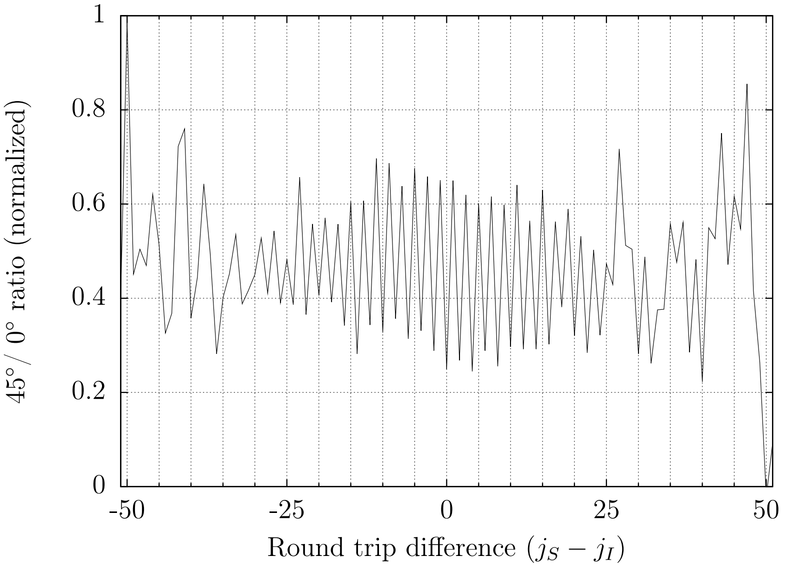

Figure 5-27: Normalized ratio for set 'j'

5.6 Unequal FSR

In order to observe the predicted $\sin^2(n\mathfrak{d}\sigma\omega_0)$ behavior of the interference dip a series of 45° and 0° histograms were taken at various temperatures. These ten sets of data (names ’a’ through ’j’) are summarized in Table 5.1 and their histograms and interference dips are shown in Figs. 5-8 to 5-27. The interference dip versus round-trip index v varied with a period v_0 which was obtained by fitting $A+B\sin^2(\pi v/v_0)$ to the data. The temperature for recurrence of the full dip was found to be ∼4.4°C from previous data. Thus, the change in the KTP CC temperature can be inferred from the v_0 fit as $dT_{fit} = 4.4°C/v_0$. The actual temperature of the KTP CC was controlled, and the measured thermistor voltage can be translated into a temperature T_{CC}. Thus the relative temperature between data sets was both directly measured and also inferred from the interference dip shape. These two measures of dT in columns 4 and 5 of Table 5.1 agree remarkably well.

The first data set, ’a’, was very near the equal FSR condition for a full dip. The next seven sets, ’b’ through ’h’, were taken with a small increment of ∼2 mV of thermistor voltage to lower the temperature. The change from the nearly flat, equal FSR, case to the $\sin^2$ behavior is clear, with set ’h’ having 10 full periods of the oscillation across the histogram. The last two sets were attempts to move to half the change from the equal FSR temperature of ’a’ to the next lower and higher equal FSR temperatures. Thus the last two sets should have triplet even-v states with a deep dip and singlet odd-v states with only a slight dip, so the 45° histogram should have alternating high and low peaks. This can be clearly seen, but the detector jitter causes the round-trip peak width to be not quite separable on the histogram. This made the tall odd v peaks bleed into the bins for the adjacent low peaks, raising the even v low peaks. The central peak had a dip ratio of 0.13 to 0.16 for ’a’ through ’h’, confirming that the central box always cancels regardless of whether the FSR is equal or unequal. The largest amplitude $A + B$ from the $A + B\sin^2(\pi v/v_0)$ fits was $A + B = 0.12 + 0.75 = 0.87$ for data set ’c’. This 0.87 is much higher than the 0.5

classical prediction.

All the 'a' through 'j' 45° and 0° histograms (between the TT and TR detectors) were acquired sequentially, each taking 16 minutes. The pump power from the fiber was mostly stable (to a few percent), but on occasion drifted by as much as 20% between some of the acquisitions, changing the level of the raw histograms. During each histogram acquisition time the rate of coincidences in a 0° basis was also being measured between the RT and RR detectors. This simultaneous reference measurement made it possible to normalize the ratio of 45° to 0° histograms, and it is the normalized ratios that are shown in the figures and used for fitting (note that the $\sin^2$ period v_0 is independent of the correction).

5.7 Imperfect Visibility

The interference ratio, $\sin(\pi v(T/4.5°\text{C}))^2$, should vary between zero and one for a polarization-entangled state. The observed variation is roughly from 0.15 to 0.85, with some data having a dip down to .106 (as seen above in Sec. 5.4). This can be explained if there was a mixture of polarization-entangled and unentangled output. The unentangled part would dip to 50%, preventing the total rate from going to zero or remaining at one. Some unentangled pairs can be generated when there is pump light traveling backwards through the crystal. Since the CC in the cavity is not in two symmetric pieces of half the PPKTP length, any pairs generated going backwards are timing shifted in the wrong direction by the external KTP CC and remain timing-distinguishable. Their contribution can be measured by inserting a HWP to swap signal and idler polarization after the cavity and before the external KTP CC. Then the backwards-generated pairs should be polarization-entangled and not the usual forward-generated pairs. This measurement was performed, and produced a dip of 0.429, which indicates that at least 14.2% of the output was generated going backwards. This is consistent with the observed variation of the pump light transmitted through the cavity, and the reflectivity of the output coupler at the pump wavelength. In total this accounts for 78.8% of the outputs that are forward-generated and entangled, and 14.2% of the outputs that are backwards-generated and entangled, which total 93.0%. Taking into account the 3% error in the length of the external KTP CC indicates that 95.8% of the output is forward or backward generated and entangled, but that only one or the other can be timing-corrected and thus polarization-entangled. The sources of the remaining imperfection are unknown.

Chapter 6

Conclusion

> "Using today's technology," Avi shot back, "that is true. But what about quantum computers? And what if new mathematical techniques are developed that can simplify the factoring of large prime numbers?"
>
> "How long do you want these messages to remain secret?" Randy asked, in his last message before leaving San Francisco. "Five years? Ten years? Twenty-five years?"
>
> After he got to the hotel this afternoon, Randy decrypted and read Avi's answer. It is still hanging in front of his eyes, like the afterimage of a strobe:
>
> `I want them to remain secret for as long as men are capable of evil.`
>
> **Neal Stephenson**, *Cryptonomicon*

6.1 Novel Source

To enable future experiments, new sources of entanglement are needed. One of the best sources of entangled qubits is photon pair production via SPDC, but non-photon entanglement is required for the joint Bell-state measurements needed to do quantum teleportation. Thus the quantum correlation must be transferred to other systems such as the proposed atomic quantum memories[33]. The 10^4 bandwidth mismatch between SPDC and the proposed Rubidium atom memory required a novel source that could be much brighter within a narrow bandwidth. To this end a more complete theory of low-power downconversion in a cavity was derived. The dependence on spatial mode matching, frequency degeneracy, and birefringence mismatch were all included in the new derivation. Experiments were then successfully performed and compared to the predictions of the model.

Initially, single-pass downconversion experiments were performed. These measurements verified the operating conditions for which polarization-entangled pairs could be produced from the PPKTP. The apparatus produced 300 pairs per second per mW of pump with high visibility.

The use of PPKTP allowed for collinear pump, signal, and idler both inside and outside the crystal. This enabled the use of a doubly-resonant linear cavity for the signal and idler. The effect of circulating the pair inside the cavity was to constructively enhance the downconversion rate at a comb of resonant frequencies. This resulted in a higher rate of downconversion than from a single-pass SPDC source. Tuning the temperature of the KTP CC inside the cavity allowed for degenerate operation with equal FSR and resulted in polarization-entangled output. Measurement of the coincidence rate indicated that the source had a measured spectral brightness of 0.7 polarization-entangled pairs per second per mW of pump per MHz of output bandwidth at degeneracy (in a single spatial mode), with 110 pairs/s/mW/MHz inferred generation rate from the 8% conditional probability. This spectral brightness easily exceeds the other reported source of narrowband polarization-entangled pairs [11], and has the highest spectral brightness of any source of polarization-entangled photons on earth. The earlier experiments by Ou and Lu in Refs. [8, 9, 10] used only a single type-I process and did not produce polarization-entanglement.

In addition to creating the doubly-resonant source that can be operated at equal

FSR to produce degenerate pairs, the unequal-FSR case was also investigated. The coincidence rate ratio of $\sin^2(\pi v(T/4.5°\mathrm{C}))$ was derived for photons in the pair having a different number of cavity round trips. This allowed a state which ranged from triplet to singlet behavior, with alternating behavior being the extreme case. The other cavity-enhanced polarization-entangled experiment in Ref. [11] used two type-I processes and needed to have the signal and idler cavity spectra aligned (the equal FSR condition) to produce both $|HH\rangle$ and $|VV\rangle$. Therefore, that experiment cannot resonantly create the unequal-FSR states with $\sin^2(\pi v(T/4.5°\mathrm{C})$ behavior. These new states are only produced using a type-II process and a cavity.

6.2 Future Work

The current cavity could be used to further verify that the output is polarization-entangled by performing a CHSH inequality measurement. In particular, the unequal-FSR output states could be further studied. All of these measurements would benefit from a slightly improved cavity. The current cavity was built using flexible mounts, using a total of eleven adjustable optic positioning knobs. Now that a working crystal and cavity configuration has been demonstrated, it can be rebuilt with more stable mounts to allow for easier locking at the output resonances. This would allow for much greater data collection rates. Exploring the output state using the histogram would be best done with a slightly longer cavity which will allow clean separation of the different round-trip peaks.

More radically new and improved cavity designs might be explored. Building off the bi-directional pump, single-pass experiments by Marco Fiorentino, [32], a bi-directionally pumped ring cavity with a single type-I downconverter might be a more robust source of degenerate narrowband polarization entanglement. This would have the advantage that the cavity birefringence is no longer a problem, since the forward and backward pairs share the same polarization, but also would lose the ability to create the unequal-FSR states. A ring cavity using a type-II process to produce polarization-entangled should be possible to build, with or without bi-directional pumping. An advantage to a bi-directionally pumped type-II process is that the signal and idler pairs need not have degenerate frequencies.

While not emphasized in this work, the cavity can be used to resonantly produce pairs in other combinations of spatial modes. By using a pump with a different focal size, the coupling into higher order Laguerre-Gaussian modes could be increased. Then by adjusting the cavity length these modes could be produced, including states with non-zero orbital angular momentum. This selective production of higher-order modes might find its own uses in the future.

Part of the original quantum-teleportation proposal was a scheme to create the pairs of polarization-entangled photons at ∼1.5 µm and transmit them down single-mode fibers. These would then be combined with active polarization correction and an upconversion apparatus to translate them to 795 nm before being used to couple into the atomic memory. Marius Albota is currently finishing such an upconversion apparatus and there is the strong possibility that a future cavity, operating at 1.5 µm instead of 795 nm, could be combined with it.

Eventually, a cavity source could be built as part of an experiment involving atomic systems. By locking the pump lasers and tuning the cavity, the polarization-entangled pair could be absorbed. The atomic systems, which may be single atoms or ensembles, would then be entangled and allow for further measurements and manipulations, especially the possibility of quantum teleportation.

Appendix A

Field Operators

> Never let the future disturb you. You will meet it, if you have to, with the same weapons of reason which today arm you against the present.
>
> **Marcus Aurelius**

There are several related variations of electromagnetic field operators $\widehat{a}$ used in this work. This appendix defines the notation and interpretation of them. The fields are in the $MKSA$ system of units, in which the classical Maxwell's equations are

$$\begin{aligned}
\epsilon_0 \nabla \cdot \boldsymbol{E} &= \rho & \boldsymbol{D} &\equiv \epsilon_0 \boldsymbol{E} + \boldsymbol{P} \\
\nabla \cdot \boldsymbol{B} &= 0 & \boldsymbol{H} &\equiv \frac{\boldsymbol{B}}{\mu_0} - \boldsymbol{M} \\
\nabla \times \boldsymbol{E} &= -\frac{\partial \boldsymbol{B}}{\partial t} & \nabla \cdot \boldsymbol{D} &= \rho_{\text{free}} \\
\nabla \times \boldsymbol{B} &= \mu_0 \boldsymbol{J} + \mu_0 \epsilon_0 \frac{\partial \boldsymbol{E}}{\partial t} & \nabla \times \boldsymbol{H} &= \boldsymbol{J}_{\text{free}} + \frac{\partial \boldsymbol{D}}{\partial t} \\
\boldsymbol{E} &= -\frac{\partial \boldsymbol{A}}{\partial t} - \nabla V & \boldsymbol{B} &= \nabla \times \boldsymbol{A} \\
P_i &= \chi^{(1)}_{ij} E_j + \chi^{(2)}_{ijk} E_j E_k + ... & c &= \frac{1}{\sqrt{\mu_0 \epsilon_0}}.
\end{aligned}$$

Instead of using a finite quantization volume V and discrete sums, this work takes the limit of infinite volume and uses continuous integrals. The discrete and continuum vacuum plane-wave operators, where i and j are the polarization indices, obey the commutation relations

$$\left[\widehat{a}_{i,\boldsymbol{k}}, \widehat{a}^{\dagger}_{j,\boldsymbol{k}'}\right] = \delta_{ij}\delta^{3}_{\boldsymbol{k},\boldsymbol{k}'}, \tag{A.1}$$

$$\left[\widehat{a}_{i}\left(\boldsymbol{k}\right), \widehat{a}^{\dagger}_{j}\left(\boldsymbol{k}'\right)\right] = \delta_{ij}\delta^{3}\left(\boldsymbol{k}-\boldsymbol{k}'\right), \tag{A.2}$$

where the $\widehat{a}$ are in units of length to the (3/2) power. Discrete operators $\widehat{a}_{\boldsymbol{k}}$ and sums are converted as follows:

$$\sqrt{\frac{V}{(2\pi)^3}}\widehat{a}_{j,\boldsymbol{k}} \rightarrow \widehat{a}_{j}\left(\boldsymbol{k}\right), \tag{A.3}$$

$$\sum_{\boldsymbol{k}} \frac{(2\pi)^3}{V} \rightarrow \int d^3\boldsymbol{k}. \tag{A.4}$$

The discrete vector potential is replaced by a continuous one [34]:

$$\widehat{\boldsymbol{A}}(\boldsymbol{r},t) = \sum_{j,\boldsymbol{k}} \boldsymbol{\varepsilon}_{j,\boldsymbol{k}}\sqrt{\frac{\hbar}{2\epsilon_0 V\omega_{j,\boldsymbol{k}}}}\left(\widehat{a}_{j,\boldsymbol{k}}\exp\left(i\boldsymbol{k}\cdot\boldsymbol{r}-i\omega_{j,\boldsymbol{k}}t\right)+H.c.\right) \tag{A.5}$$

$$\widehat{\boldsymbol{A}}(\boldsymbol{r},t) = \sum_{j}\iiint d^3\boldsymbol{k}\,\boldsymbol{\varepsilon}_{\boldsymbol{j}}(\boldsymbol{k})\sqrt{\frac{\hbar}{2\epsilon_0\omega_j(\boldsymbol{k})}}\left(\widehat{a}_j(\boldsymbol{k})\frac{\exp\left(i\boldsymbol{k}\cdot\boldsymbol{r}-i\omega_j(\boldsymbol{k})t\right)}{(2\pi)^{3/2}}+H.c.\right) \tag{A.6}$$

In the above definitions $\boldsymbol{\varepsilon}_{j,\boldsymbol{k}}$ is the polarization unit vector and $H.c.$ stands for the Hermitian conjugate of the preceding terms. The electric field $\widehat{\boldsymbol{E}}(\boldsymbol{r},t)$ is equal to $-\partial\widehat{\boldsymbol{A}}/\partial t$ in all cases.

Since several fields will be present, attention must be paid to the phases in (A.6). By construction of $\widehat{\boldsymbol{A}}$, the $\widehat{a}_j(\boldsymbol{k})$ terms create plane-wave fields that all have the same zero phase at the $(\boldsymbol{r},t) = (\boldsymbol{0},0)$.

A canonical quantum description of macroscopic electromagnetism in non-uniform dispersive anisotropic nonlinear materials is more complex [35] than needed for a model of downconversion in the experimental regime. Only the vacuum operators and simplified material operators will be required.

Reformulating the evolving fields at a certain time as propagating fields at a certain position x as done in Refs. [36, 22] allows for a more natural treatment of quantum optics and derivation of downconversion. This is accompanied by a change of variables from k_x to ω. The choice of x, instead of the more common z, agrees with the experiment's propagation along the x-axis of the nonlinear material. This replacement of the longitudinal k_x with ω has serendipitous consequences: the refraction of the $\boldsymbol{k}$ vectors on entering and leaving the material is polarization dependent and needlessly add to the complexity, but with material interfaces normal to x all three parameters ω, k_y, and k_z are unchanged. The (y, z) part of $\boldsymbol{r}$ will be denoted as $\boldsymbol{s}$ and the (k_y, k_z) part of $\boldsymbol{k}$ will be denoted $\boldsymbol{q}$.

The change of variables affects the integral and commutator:

$$k_{x,j}(\boldsymbol{q},\omega) = \pm\sqrt{\left(\frac{\omega}{c}\right)^2 - |\boldsymbol{q}|^2} = \pm\left(\frac{\omega}{c^2}\right) g(\boldsymbol{q},\omega), \text{ where} \tag{A.7}$$

$$g(\boldsymbol{q},\omega) \equiv c\sqrt{1 - \left(\frac{|\boldsymbol{q}|c}{\omega}\right)^2}, \tag{A.8}$$

$$dk_{x,j} \to \frac{dk_{x,j}(\boldsymbol{q},\omega)}{d\omega} d\omega = \pm\frac{d\omega}{g(\boldsymbol{q},\omega)}, \tag{A.9}$$

$$\iiint_{k_x>0} d^3\boldsymbol{k} \to \iint d^2\boldsymbol{q} \int_{c|\boldsymbol{q}|}^{\infty} d\omega \frac{1}{g(\boldsymbol{q},\omega)}, \tag{A.10}$$

$$\iiint_{k_x<0} d^3\boldsymbol{k} \to \iint d^2\boldsymbol{q} \int_{c|\boldsymbol{q}|}^{\infty} d\omega \frac{1}{g(\boldsymbol{q},\omega)}, \tag{A.11}$$

$$\left[\widehat{a}_i^{+}\left(k_{x,i}(\boldsymbol{q},\omega),\boldsymbol{q}\right), \widehat{a}_j^{+\dagger}\left(k_{x,j}(\boldsymbol{q}',\omega),\boldsymbol{q}'\right)\right] = \delta^2\left(\boldsymbol{q}-\boldsymbol{q}'\right)\delta(k_{x,i}(\boldsymbol{q},\omega) - k_{x,j}(\boldsymbol{q}',\omega'))\delta_{ij} \tag{A.12}$$

$$= g(\boldsymbol{q},\omega)\delta^2\left(\boldsymbol{q}-\boldsymbol{q}'\right)\delta(\omega-\omega')\delta_{ij}. \tag{A.13}$$

The separation of $k_x > 0$ and $k_x < 0$ will be useful, in particular with propagation inside a cavity. The g_j function in the commutator is bothersome but will now be absorbed by the reformulated photon-flux operators $\widehat{a}_j^{\pm}(\boldsymbol{q},\omega)$ via

$$\widehat{a}_j\left(k_{x,j}(\boldsymbol{q},\omega),\boldsymbol{q}\right) \rightarrow \widehat{a}_j^{\pm}(\boldsymbol{q},\omega)\sqrt{g(\boldsymbol{q},\omega)}, \tag{A.14}$$

where the + superscripts denotes $k_x > 0$ and the − denotes $k_x < 0$. The commutation relations are

$$\left[\widehat{a}_i^{\pm}(\boldsymbol{q},\omega),\widehat{a}_j^{\pm\dagger}(\boldsymbol{q}',\omega')\right] = \delta(\boldsymbol{q}-\boldsymbol{q}')\delta(\omega-\omega')\delta_{ij} \tag{A.15a}$$

$$\left[\widehat{a}_i^{\pm}(\boldsymbol{q},\omega),\widehat{a}_j^{\mp\dagger}(\boldsymbol{q}',\omega')\right] = 0 \tag{A.15b}$$

$$\left[\widehat{a}_i^{\pm}(\boldsymbol{q},\omega),\widehat{a}_j^{\pm}(\boldsymbol{q}',\omega')\right] = \left[\widehat{a}_i^{\pm}(\boldsymbol{q},\omega),\widehat{a}_j^{\mp}(\boldsymbol{q}',\omega')\right] = 0. \tag{A.15c}$$

The vector potential splits into forward and backward propagating pieces

$$\widehat{\boldsymbol{A}}(\boldsymbol{r},t) = \widehat{\boldsymbol{A}}^{+}(\boldsymbol{r},t) + \widehat{\boldsymbol{A}}^{-}(\boldsymbol{r},t) + H.c., \tag{A.16}$$

$$\begin{aligned}\widehat{\boldsymbol{A}}^{+}(\boldsymbol{r},t) = \widehat{\boldsymbol{A}}^{+}(x,\boldsymbol{s},t) = \sum_j \iiint \frac{d^2\boldsymbol{q}\,d\omega}{\sqrt{g(\boldsymbol{q},\omega)}}\boldsymbol{\varepsilon_j}(\boldsymbol{q},\omega)\sqrt{\frac{\hbar}{2\epsilon_0\omega}} \\ \widehat{a}_j^{+}(\boldsymbol{q},\omega)\frac{\exp\left(ik_{x,j}(\boldsymbol{q},\omega)x + i\boldsymbol{q}\cdot\boldsymbol{s} - i\omega t\right)}{(2\pi)^{3/2}},\end{aligned} \tag{A.17}$$

where the explicit limits on $d\omega$ are dropped for simplicity. The energy in the system, dropping the infinite component, is as expected

$$\widehat{H} = \iiint d^2\boldsymbol{q}\,d\omega\,\hbar\omega\left(\widehat{a}^{+\dagger}(\boldsymbol{q},\omega)a^{+}(\boldsymbol{q},\omega) + a^{-\dagger}(\boldsymbol{q},\omega)a^{-}(\boldsymbol{q},\omega)\right). \tag{A.18}$$

An expression for $\widehat{\boldsymbol{E}}$ in a material will be needed, but only in the paraxial and quasi-monochromatic limit. The variable transformation from k_x to ω in the material will use the $\kappa_m(\boldsymbol{q},\omega)$ functions

$$\kappa_{S,I,P}(\boldsymbol{q},\omega)=\sqrt{\left(\frac{n_{S,I,P}(\boldsymbol{q},\omega)\omega}{c}\right)^2-|\boldsymbol{q}|^2}, \tag{A.19}$$

where the subscript $m = S, I, P$ indicates both polarization and central frequency for signal, idler, or pump beams. The κ are analytical, if a bit messy, with this parameterization. In the paraxial limit the group velocity is approximately

$$v_G(m,\boldsymbol{q},\omega)\approx\left(\frac{\partial\kappa_m(\boldsymbol{q},\omega)}{\partial\omega}\right)^{-1}, \tag{A.20}$$

and the integration transforms as

$$\iiint_{k_x>0} d^3\boldsymbol{k}\rightarrow\iint d^2\boldsymbol{q}\int_{|\boldsymbol{q}|c/n*}^{\infty} d\omega\,\frac{1}{v_G(m,\boldsymbol{q},\omega)}, \tag{A.21}$$

where $n*$ depends on $\boldsymbol{q}$ and m, and is the value of $n_m(\boldsymbol{q},\omega)$ when $\kappa_m(\boldsymbol{q},\omega)$ is equal to zero for small ω. This integral has a lower limit than the one in free space with the "extra" modes being those past the critical angle and only exist inside the material. The explicit limits will be dropped for simplicity.

Inside a dispersive material, the index of refraction cannot be everywhere real as a consequence of causality. However, here the fields are confined to several quasi-monochromatic frequencies where the index is approximately real and the imaginary component, and thus absorption, will be neglected.

From [34] the equivalent of (A.6) inside a material is:

$$\widehat{\boldsymbol{A}}(\boldsymbol{r},t)=\sum_m\iiint d^3\boldsymbol{k}\,\boldsymbol{\varepsilon}_m\sqrt{\frac{\hbar v_G(m,\boldsymbol{k})}{2\epsilon_0\omega_m(\boldsymbol{k})n_m c}}\left(\widehat{a}_m(\boldsymbol{k})\frac{\exp\left(i\boldsymbol{k}\cdot\boldsymbol{r}-i\omega_m(\boldsymbol{k})t\right)}{(2\pi)^{3/2}}+H.c.\right). \tag{A.22}$$

Using $\widehat{a}_m(\boldsymbol{k}) \rightarrow \sqrt{v_G(m, \boldsymbol{q}, \omega)}\widehat{a}_m(\boldsymbol{q}, \omega)$ produces $\widehat{\boldsymbol{A}}^{\pm}$ in the material:

$$\widehat{\boldsymbol{A}}^{\pm}(\boldsymbol{r}, t) = \sum_m \iiint d^2\boldsymbol{q} d\omega \, \boldsymbol{\varepsilon}_m \sqrt{\frac{\hbar}{2\epsilon_0 \omega n_m c}} \widehat{a}^{\pm}_m(\boldsymbol{q}, \omega) \frac{\exp\left(\pm i\kappa_m(\boldsymbol{q}, \omega)x + i\boldsymbol{q} \cdot \boldsymbol{s} - i\omega t\right)}{(2\pi)^{3/2}}. \tag{A.23}$$

Taking the negative time derivative of $\widehat{\boldsymbol{A}}$ produces $\widehat{\boldsymbol{E}}$:

$$\widehat{\boldsymbol{E}}(\boldsymbol{r}, t) = \widehat{\boldsymbol{E}}^{+}(\boldsymbol{r}, t) + \widehat{\boldsymbol{E}}^{-}(\boldsymbol{r}, t) + H.c., \tag{A.24}$$

$$\widehat{\boldsymbol{E}}^{\pm}(\boldsymbol{r}, t) = \widehat{E}^{\pm}_S(\boldsymbol{r})\boldsymbol{\varepsilon}_S + \widehat{E}^{\pm}_I(\boldsymbol{r})\boldsymbol{\varepsilon}_I + \widehat{E}^{\pm}_P(\boldsymbol{r})\boldsymbol{\varepsilon}_P, \tag{A.25}$$

$$\widehat{E}^{\pm}_m(\boldsymbol{r}, t) = \iiint d^2\boldsymbol{q} d\omega \, i \sqrt{\frac{\hbar\omega}{2\epsilon_0 n_m(\boldsymbol{q}, \omega) c}} \widehat{a}^{\pm}_m(\boldsymbol{q}, \omega) \frac{\exp\left(\pm i\kappa_m(\boldsymbol{q}, \omega)x + i\boldsymbol{q} \cdot \boldsymbol{s} - i\omega t\right)}{(2\pi)^{3/2}}. \tag{A.26}$$

The vacuum equations and material equations both assume the world is homogeneous: that there is only one kind of uniform medium. This is fixed by the exp() functions which only refer to a single uniform dispersion relation.

Quantum optics treating multiple materials needs a slightly more complicated formulation. If the material boundaries are all perpendicular to the paraxial axis (x) then it is straightforward to move the complexity of the space into the operators. The field operators can be transformed into a form that obeys the equal-space commutation relation

$$\left[\widehat{a}^{\pm}_i(\boldsymbol{q}, \omega; x), \widehat{a}^{\pm\dagger}_j(\boldsymbol{q}', \omega'; x)\right] = \delta(\boldsymbol{q} - \boldsymbol{q}')\delta(\omega - \omega')\delta_{ij}, \tag{A.27}$$

where the x coordinate dependence has been added to the notation. This x dependence subsumes that of operators built from it, so that

$$\widehat{A}_m^{\pm}(\boldsymbol{s},t;x) = \iiint d^2\boldsymbol{q}d\omega \sqrt{\frac{\hbar}{2\epsilon_0\omega n_m(\boldsymbol{q},\omega;x)c}}\frac{\exp(i(\boldsymbol{q}\cdot\boldsymbol{s}-\omega t))}{(2\pi)^{3/2}}\widehat{a}_m^{\pm}(\boldsymbol{q},\omega;x) \tag{A.28}$$

$$\widehat{E}_m^{\pm}(\boldsymbol{s},t;x) = \iiint d^2\boldsymbol{q}d\omega\, i\sqrt{\frac{\hbar\omega}{2\epsilon_0 n_m(\boldsymbol{q},\omega;x)c}}\frac{\exp(i(\boldsymbol{q}\cdot\boldsymbol{s}-\omega t))}{(2\pi)^{3/2}}\widehat{a}_m^{\pm}(\boldsymbol{q},\omega;x). \tag{A.29}$$

The phase of the new $\widehat{a}(;x)$ operators acts to record the progression of the plane wave from the origin, where x is zero, through the different materials to the specified x plane. Thus the $\widehat{\boldsymbol{E}}$ field operator "knows" the structure of the space, including knowing the nonlinear interactions.

There is an analogous version $\widehat{a}(\boldsymbol{k};t)$ that obeys an equal-time commutation relation and subsumes the $\exp(-i\omega t)$ dependence of $\widehat{\boldsymbol{A}}(\boldsymbol{r};t)$, but it will not be needed. Other continuum formulations use variations on these $\widehat{a}$ that differ by factors of 2π, the system of units for the fields, or the definition of the fields as $\mathrm{Re}(A...)$ instead of $A + H.c.$, which can also introduce factors of 2.

Bibliography

[1] C. K. Hong, Z. Y. Ou, and L. Mandel. Measurement of subpicosecond time intervals between two photons by interference. *Phys. Rev. Lett.*, 59(18):2044–2046, November 1987.

[2] Alain Aspect, Philippe Grangier, and Gérard Roger. Experimental tests of realistic local theories via Bell's theorem. *Phys. Rev. Lett.*, 47(7):460–463, August 1981.

[3] E. Knill, R. Laflamme, and G. J. Milburn. A scheme for efficient quantum computation with linear optics. *Nature*, 409(6816):46–52, January 2001.

[4] C. H. Bennett and G. Brassard. Quantum cryptography: Quantum key distribution and coin tossing. In *Proceedings of IEEE International Conference on Computers, Systems and Signal Processing*, pages 175–179, Bangalore, India, December 1984.

[5] Charles H. Bennett, Gilles Brassard, Claude Crépeau, Richard Jozsa, Asher Peres, and William K. Wootters. Teleporting an unknown quantum state via dual classical and Einstein-Podolsky-Rosen channels. *Phys. Rev. Lett.*, 70(13):1895–1899, March 1993.

[6] Jeffrey H Shapiro. Architectures for long-distance quantum teleportation. *New Journal of Physics*, 4:47, 2002.

[7] Jeffrey H Shapiro and N C Wong. An ultrabright narrowband source of polarization-entangled photon pairs. *J. Opt B*, 2(1):L1–L4, February 2000.

[8] Z. Y. Ou and Y. J. Lu. Cavity enhanced spontaneous parametric down-conversion for the prolongation of correlation time between conjugate photons. *Phys. Rev. Lett.*, 83(13):2556–2559, September 1999.

[9] Y. J. Lu and Z. Y. Ou. Optical parametric oscillator far below threshold: Experiment versus theory. *Phys. Rev. A*, 62:033804, August 2000.

[10] Y. J. Lu, R. L. Campbell, and Z. Y. Ou. Mode-locked two-photon states. *Phys. Rev. Lett.*, 91(16):163602, 2003.

[11] Haibo Wang, Tomoyuki Horikiri, and Takayoshi Kobayashi. Polarization-entangled mode-locked photons from cavity-enhanced spontaneous parametric down-conversion. *Phys. Rev. A*, 70:043840, October 2004.

[12] G. D. Boyd and D. A. Kleinman. Parametric interaction of focused gaussian beams. *Journal of Applied Physics*, 39(6):3597–3639, July 1968.

[13] J. Q. Yao and Theodore S. Fahlen. Calculations of optimum phase match parameters for the biaxial crystal $KTiPO_4$. *Journal of Applied Physics*, 55(1):65–68, January 1984.

[14] W. Wiechmann, S. Kubota, T. Fukui, and H. Masuda. Refractive-index temperature derivatives of potassium titanyl phosphate. *Optics Letters*, 18(15):1208–1210, August 1993.

[15] Martin M. Fejer, G. A. Magel, H. Jundt, and Robert L. Byer. Quasi-phase-matched second harmonic generation: Tuning and tolerances. 28(11):2631–2654, November 1992.

[16] Mark Hillery and Leonard D. Mlodinow. Quantization of eletrodynamics in nonlinear dielectric media. *Phys. Rev. A*, 30(4):1860–1865, October 1984.

[17] I. Abram and E. Cohen. Quantum theory for light propagation in a nonlinear effective medium. *Phys. Rev. A*, 44(1):500–517, July 1991.

[18] Morton H. Rubin, David N. Klyshko, Y. H. Shih, and A. V. Sergienko. Theory of two-photon entanglement in type-II optical parametric down-conversion. *Phys. Rev. A*, 50(6):5122–5133, December 1994.

[19] Lu-Ming Duan and Guang-Can Guo. Alternative approach to electromagnetic field quantization in nonlinear and inhomogeneous media. *Phys. Rev. A*, 56(1):925–930, July 1997.

[20] Meta Atatüre, Goivanni Di Giuseppe, Matthew D Shaw, Alexander V. Sergienko, Bahaa E. A. Saleh, and Malvin C. Teich. Multiparameter entanglement in quantum interferometry. *Phys. Rev. A*, 66:023822, 2002.

[21] Jeffrey H. Shapiro. High-efficiency upconversion for photon counting and quantum-state frequency conversion. Technical report, MIT Lincoln Laboratory Group 67, July 2004.

[22] B. Huttner, S. Serulnik, and Y. Ben-Aryeh. Quantum analysis of light propagation in a parametric amplifier. *Phys. Rev. A*, 42(9):5594–5600, November 1990.

[23] Marco Fiorentino, Christopher E. Kuklewicz, and Franco N. C. Wong. Source of polarization entanglement in a single periodically poled $\mathrm{KTiOPO_4}$ crystal with overlapping emission cones. *Optics Express*, 13(1):127–135, January 2005.

[24] John F. Clauser, Michael A. Horne, Abner Shimony, and Richard A. Holt. Proposed experiment to test local hidden-variable theories. *Phys. Rev. Lett.*, 23(15):880, October 1969.

[25] Paul G. Kwiat, Klaus Mattle, Harald Weinfurter, Anton Zeilinger, Alexander V. Sergienko, and Yanhua Shih. New high-intensity source of polarization-entangled photon pairs. *Phys. Rev. A*, 75(24):4337–4342, dec 1995.

[26] Christopher E. Kuklewicz, Eser Keskiner, Franco N. C. Wong, and Jefferery H. Shapiro. A high-flux entanglement source based on a doubly resonant optical parametric amplifier. *J. Opt B*, 4:S162–S168, 2002.

[27] H. Kogelnik and T. Li. Laser beams and resonators. *Appl. Opt.*, 5(10):1550–1567, 1966.

[28] M. J. Collett and C. W. Gardiner. Squeezing of intracavity and traveling-wave light fields produced in a parametric amplification. *Phys. Rev. A*, 30(3):1386–1391, September 1984.

[29] Jeffrey H. Shapiro, Christopher E. Kuklewicz, and Franco N.C. Wong. Quantum signatures from singly-resonant and doubly-resonant parametric amplifiers. pages 1–3. OSA NLO, OSA, 2004.

[30] D. Lee and N.C. Wong. Tuning characteristics of a cw dual-cavity ktp optical parametric oscillator. *Applied Physics B*, 66(2):133–143, February 1998.

[31] Christopher E. Kuklewicz, Marco Fiorentino, Gaëtan Messin, Franco N. C. Wong, and Jeffrey H. Shapiro. High-flux source of polarization-entangled photons from a periodically poled $KTiOPO_4$ parametric down-converter. *Phys. Rev. A*, 69(1):013807, January 2004.

[32] Marco Fiorentino, Gaétan Messin, Christopher E. Kuklewicz, Franco N. C. Wong, and Jeffrey H. Shapiro. Generation of ultrabright tunable polarization entanglement without spatial, spectral, or temporal constraints. *Phys. Rev. A*, 69(4):041801(R), April 2004.

[33] S. Lloyd, M. S. Shahriar, J. H. Shapiro, and P. R. Hemmer. Long distance, unconditional teleportation of atomic states via complete bell state measurements. *Phys. Rev. Lett.*, 87(16):167903, October 2001.

[34] K. J. Blow, Rodney Loudon, Simon J. D. Phoenix, and T. J. Shepherd. Continuum fields in quantum optics. *Phys. Rev. A*, 42(7):4102–4114, October 1990.

[35] A. Lukš and V. Peřinová. Canonical quantum description of light propagation in dieletric media. *Progress in Optics*, 43:295–431, 2002.

[36] Horace P. Yuen and Jeffrey H. Shapiro. Optical communication with two-photon coherent states–part i: Quantum-state propagation and quantum-noise reduction. *IEEE Transactions on Information Theory*, IT-24(6):657–668, November 1978.